Design of a Robust Priming Controller for SMA Actuators

by

Zihao Hunter Song

A thesis
presented to the University of Waterloo
in fulfillment of the
thesis requirement for the degree of
Master of Applied Science
in
Electrical and Computer Engineering

Waterloo, Ontario, Canada, 2012

Author's Declaration

I hereby declare that I am the sole author of this thesis. This is a true copy of the thesis, including any required final revisions, as accepted by my examiners.

I understand that my thesis may be made electronically available to the public.

Abstract

Shape Memory Alloys (SMAs) have been demonstrated to be effective actuator elements in a wide range of applications, such as robotics, medicine, aerospace and automotive. Enabled by the unique thermo-mechanical properties of SMAs, these actuators offer the advantages of light weight, high power-to-weight ratio and a simple actuation mechanism compared to traditional actuator types. At the same time, the widespread adoption of the SMA actuator remains elusive as its low power efficiency and complex hysteretic behaviour often render it an impractical means of actuation. These actuators also exhibit a slow response speed and their response is highly sensitive to changes in the external environment, namely ambient temperature and mechanical stress, thus complicating their control. Position, force or temperature sensors may be used to facilitate feedback control, but at the cost of increasing the overall size and complexity of the system.

The difficulties caused by the hysteretic behaviour can be largely avoided when SMA wires are used as on-off actuators, making SMAs well suited for such applications. However, they may still be subject to a wide range of dynamic operating conditions that would impact their actuation time, and achieving a consistent actuation time is often highly desirable.

This thesis presents the synthesis of a nitinol SMA actuator control system which uses electrical resistance feedback to enable a fast response speed and robustness to disturbances in the external environment. A study of the resistance behaviour of SMAs is discussed first. The design of an adaptive controller and the experimental evaluation of its performance are described in detail next. The objective of the SMA actuator control system is to achieve a consistent and fast actuation time throughout the range of operating ambient temperature and stress. The control system is implemented experimentally and shown to be quite successful.

Acknowledgements

I would like to thank many people who have helped and guided me through my academic endeavour, for without them it would not be possible for me to craft this thesis and complete my research project.

I would like to first thank my supervisor Robert B. Gorbet for giving me the opportunity to work on this project, for providing speedy and valuable advice every step of the way, and for editing my thesis. I would like to thank Dr. Eric Kubica for his valuable advice on hardware implementation as well as being the best company in the lab. Also, I'd like to thank Mr. Kevin Krauel for his help on the design of the electrical system of my project. I would also like to offer thanks to Dr. David Wang and Dr. Shreyas Sundaram for reviewing my thesis.

I would also like to give thanks to my friends and colleagues at UW for keeping the stress in graduate school under control: Chuan Yu, Mike Takeda, Darrell Gaudette, Shailaja Sajja, and many others. You had offered meaningful conversations about research as well as life in general that helped me become a better person and made my Master's a wonderful experience.

I would also like to thank the Engineering Student Machine Shop, Jorge Cruz and Mike Luckenhaus for helping me machine components for my project.

Finally, and most importantly, I would like to thank my mum and dad for their patience and unwavering support throughout the past seven years while I was at UW. Last but not least, thank you to Jenny, my sweetheart, for believing in me during the hard times.

Dedication

I dedicate this thesis to my mum and dad, for their unwavering support and faith in me.

Table of Contents

List of Figures

List of Tables

Chapter 1

Introduction

Shape memory alloys (SMAs) are “smart materials” that possess unique geometry change properties which could be exploited for engineering applications. Their name comes from the fact that these materials can be deformed, but will return to their original shape when they are heated, as if they “remember” their original shape. Actuators made from SMAs have the advantages of a simple actuation mechanism, low weight, and a high power-to-weight ratio [1] as compared to conventional actuator systems, such as motors, hydraulics or solenoids. For these reasons, SMAs been applied in the past as actuators for fuel injector valves [2], active endoscopes [3], and miniature robotic “muscles” and “morphing structures” on aeroplanes [4].

There are many different kinds of shape memory alloys, such as Cu-Zn-Al, Cu-Al-Ni, or Ni-Ti to name a few. Of all the different kinds of SMAs, the Ni-Ti alloy, or nitinol, has been the most studied and commercially viable SMA material for actuator applications. In SMA actuators, actuation is achieved usually by passing an electrical current through a nitinol wire, causing it to increase in temperature and undergo the geometry change.

1.1 Motivation

In addition to the above mentioned advantages of SMA actuators, they also have a self-sensing capability which, in some applications, allows sufficient control to be established without needing sensors that add to the total cost and size of the actuator system. This can be done using their electrical resistance behaviour. At the same time, one drawback of using

SMA actuators is that, using the traditional actuation method of passing a constant current through the SMA wire, the response time is often variable as a result of different operating conditions.

This research, at its core, seeks to apply the self-sensing capability of SMA actuators to both reduce their response time as well as the associated variability. Specifically, in [5], Featherstone *et al* designed a heating method that allows a larger current than the "safe current" to be applied safely to the SMA actuator using resistance feedback. In [6] a controller using resistance feedback was designed to pre-emptively "prime" the SMA actuator to the cusp of actuation, thereby reducing the response time for the subsequent actuation. The motivation for this research is to enhance the design of such "priming controllers" to both minimize the response time as well as make it more consistent in a diverse range of dynamic operating conditions.

1.2 Goals

There are three goals for this research:

- Develop a model that adequately describes the electrical resistance behaviour of the SMA actuator during its operation;
- Design a priming controller that uses the knowledge embedded within the SMA resistance model to allow the SMA actuator to be pre-emptively brought to, then maintained at the cusp of actuation prior to the actuation command; and
- Evaluate the performance of the priming controller in diverse conditions, where the ambient temperature and stress on the SMA wire may change arbitrarily during the operation of the SMA actuator.

1.3 Outline

The rest of this thesis is organized as follows.

- In Chapter 2, the background information on SMAs as well as a review of SMA actuator designs and control techniques are presented. The motivation for this research is also elaborated in much more technical detail.
- In Chapter 3, the objective, requirements and criteria of the priming controller design that is the crux of this research are defined.
- In Chapter 4, the mechanical and electrical designs of the experimental testing platform as well as the software environment are described.
- In Chapter 5, the development and experimental identification of the SMA resistance model is discussed.
- In Chapter 6, the design of the priming controller is presented. The controller incorporates an inverse model based on the SMA resistance model developed in Chapter 5 to allow the SMA wire to be maintained at a temperature that is very close to the temperature where the actuation starts.
- Chapter 7 presents the results of the experimental evaluation of the priming controller design, based on the criteria outlined in Chapter 3.
- Finally, the conclusion for this research and recommendations for future work are presented in Chapter 8.

Chapter 2

Background, literature Review and motivation

In this chapter, the background on shape memory alloys is presented first, including the physics behind their unique properties, and their advantages and limitations. The second section presents a review of feedback control methods for SMA actuators, with a particular focus on using electrical resistance as feedback. Lastly, an in-depth technical explanation of the motivation for this research project is presented.

2.1 Shape memory alloy background

Shape memory alloys (SMAs) exhibit special mechanical properties when the material temperature is changed. These properties are a result of unique microscopic changes in the alloy's crystalline structure that are temperature and stress dependent. At a high temperature, the SMA material crystalline structure is in a body-centered cubic (BCC) geometry (B2 phase [7]) that is structurally similar to the austenite allotrope of iron, and hence this SMA phase is called the austenite phase, or "A-phase". Once the temperature has dropped low enough, the SMA undergoes a phase transformation into the B-19' monoclinic martensite phase [7], or "M-phase". If the temperature is increased again, the SMA once more transforms back into A-phase. In many SMAs there is also a third phase that may show up during the austenite to martensite phase transformation, called the rhombohedral phase or R-phase. The R-phase is essentially a distortion of the A-phase [7], and during cooling the R-phase may compete with M-phase in transforming from the A-phase. However, R-phase is

usually negligible in SMAs that exhibit the strongest shape memory effect [8] and in addition the research presented in this thesis focuses on the martensite to austenite phase transformation, or "M→A transformation", so it can be safety ignored here.

In this research, a widely available SMA material called Flexinol manufactured by Dynalloy Inc. is used experimentally. Flexinol is a nickel-titanium shape memory alloy, or "nitinol", which is a kind of SMA that is widely used for actuator applications. The repeatable M→A transformation behaviour of Nitinol has been investigated in great detail. Perhaps the most attention has been given to the hysteresis in the temperature-dependent phase transformation behaviour. As shown in Figure 2.1, the nitinol martensite phase fraction (traditionally denoted as ξ_M) can be viewed as a function of the temperature. During heating, the SMA material gradually transitions from being approximately completely in M-phase to being completely in A-Phase (or 0% M-phase) between the *austenite start* and *austenite finish* temperatures (A_s and A_f respectively), and during cooling the reverse transition takes place between the *martensite start* and *martensite finish* temperatures, or M_s and M_f respectively. The heating and cooling phase transition curves joined together form the *major hysteresis loop*. Experimentally, the transformation temperatures A_s, A_f, M_s, and M_f are difficult to measure precisely, and in literature their exact numerical definitions differ depending on the purpose of study. As shown in Figure 2.1, for engineering applications it is common to define these transformation temperatures as the "corner" temperatures of the quadrilateral fitted to the hysteresis loop [9]. If nitinol were to undergo partial transformation cycles, caused by temperature reversals in the ranges of (A_s, A_f) or (M_s, M_f), then *minor hysteresis loops* would be formed inside the major loop. Commercially available nitinol SMA materials that are suitable for engineering applications are manufactured such that the four transformation temperatures can be controlled by varying the elemental compositions of the alloy.

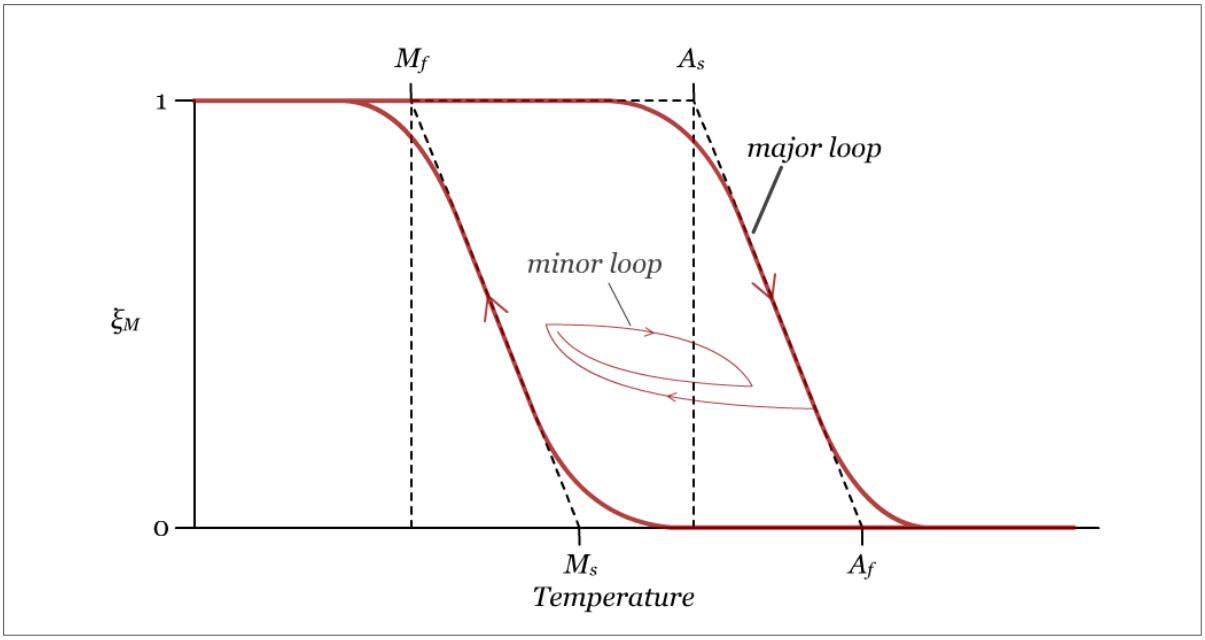

Figure 2.1: Martensite phase fraction vs. temperature. The major hysteresis loop, a minor loop, and the transformation temperatures are illustrated.

The martensite and austenite microstructural phases differ vastly in their mechanical properties. Notably, the Young's modulus varies sufficiently to make nitinol in wire form suitable as means of actuation. As shown in Figure 2.2, the high temperature A-phase structure is microscopically more compact and has a higher elastic modulus than the low temperature M-phase structure, which causes the nitinol wire to contract when heated above A_s. When the wire is cooled, the austenite transforms to the twinned martensite form which then is stretched to the detwinned martensite form under mechanical loading, resulting in an extension of the wire. When the wire is heated again, it transformed back to A-phase and the original A-phase strain is recovered. This unique shape change behaviour is called the Shape Memory Effect (SME), and is the mechanism which allows nitinol wires to be made into "SMA actuators".

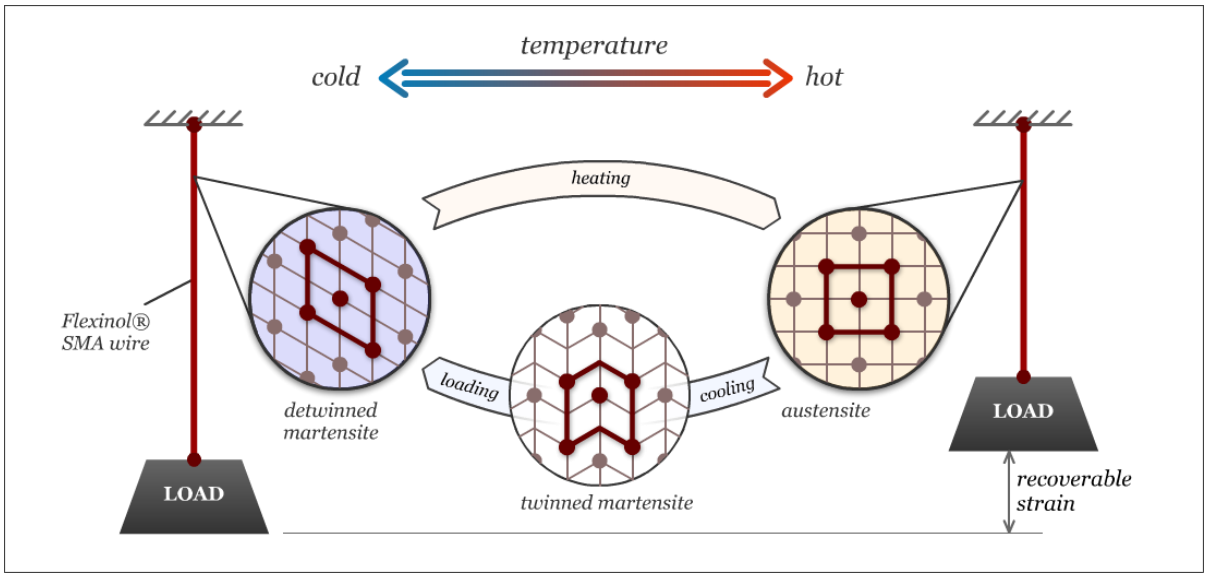

Figure 2.2: The physical mechanism of the Shape Memory Effect.

Nitinol also exhibits another distinctive behaviour called the Pseudo-Elastic Effect. The cause of this effect is the stress-dependent nature of the four transformation temperatures. Figure 2.3 shows that increasing the stress on nitinol causes the transformation temperatures to shift upwards. This means that the application of additional stress to a nitinol material in austenitic state causes it to transform partially or fully into the more elastic and deformable martensite if M_s shifts above the temperature of the material (though not shown in Figure 2.3, removing the additional stress at this point allows the nitinol material to revert back to austenite). With proper design and manufacturing of nitinol materials, the pseudo-elastic effect has allowed nitinol be used in place of traditional metal alloy or plastic materials where the ability to deform elastically under high load is required, such as in dental braces or shock-resistant eyeglass frames [10]. For actuator applications, the Pseudo-Elastic Effect is not used, but the stress-dependent nature of the transformation temperatures is still a factor in the performance of SMA actuators.

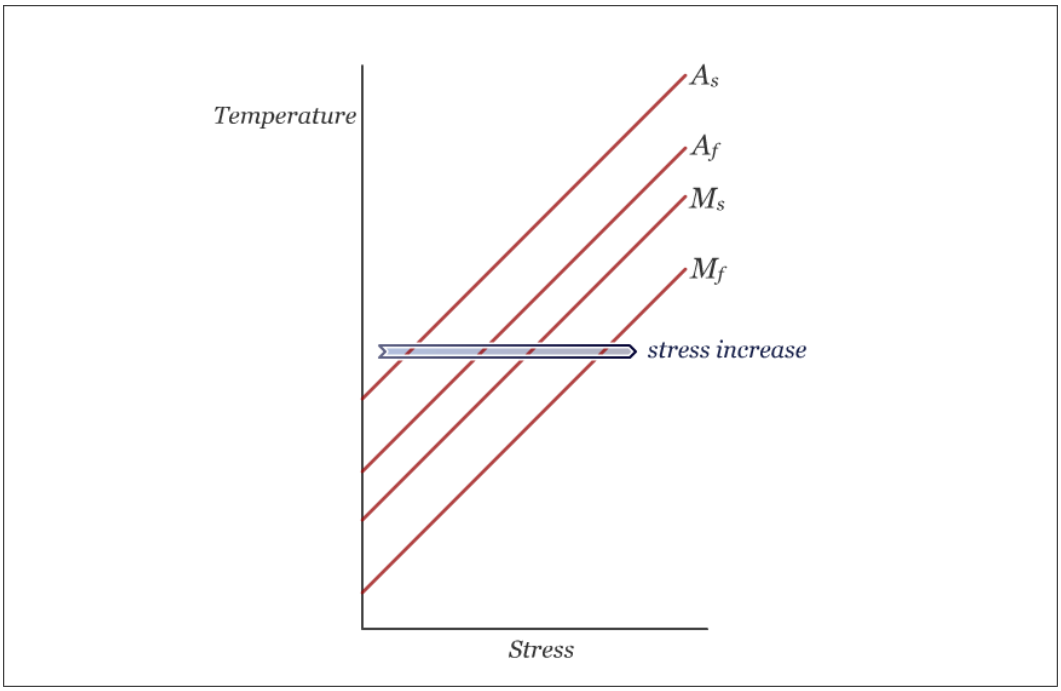

Figure 2.3: Stress-dependence of the transformation temperatures of nitinol.

The Shape Memory Effect is more commonly exploited in the design of nitinol SMA actuators. Nitinol is manufactured into a wire so that the M→A and A→M phase transformations render wire contraction and expansion respectively, given that there is load on the wire (without load the wire would not be able to expand upon A→M transformation). The Flexinol® wire used in the experiments in this research may achieve a stable recoverable strain of 3% to 4% for tens of thousands of actuation cycles [11]. Larger strains may be achieved by increasing the load of the Flexinol® wire; however doing so will increase the transformation temperatures as well as the likelihood of microscopic plastic deformations in the wire, both of which are detrimental to the life and cycling repeatability of the SMA actuator. Manufacturer's data for Flexinol® [11] shows that even at a relatively low stress of 103MPa (less than a third of the 350MPa fatigue stress of nitinol [12]), the wire may experience up to 0.5% permanent strain change after tens of thousands of actuation cycles [11].

Nitinol wires that are suitable for use as actuators are usually manufactured to have transformation temperatures between 60°C to 110°C. The M→A "forward" phase transformation is most commonly achieved using Joule Heating - the process where the wire is heated by passing an electrical current through it, resulting in a wire length contraction; while the A→M "reverse" transformation is achieved by cutting off the electrical current and allowing the nitinol wire to cool via convection to the surrounding medium. While only contraction can be actively performed using a single SMA wire, there are multiple ways for an SMA actuator to achieve two-way motion. As shown in Figure 2.4, a spring or a dead weight may be used to provide a bias force for the nitinol wire that allows the wire to be extended during cooling [11]. Another popular method is to connect two nitinol wires in an antagonistic arrangement for active two-way motion control [3] [13]. In this research, a dead weight is used with one nitinol wire for two-way motion, so this configuration will be referred to as the *SMA actuator* in the rest of this thesis.

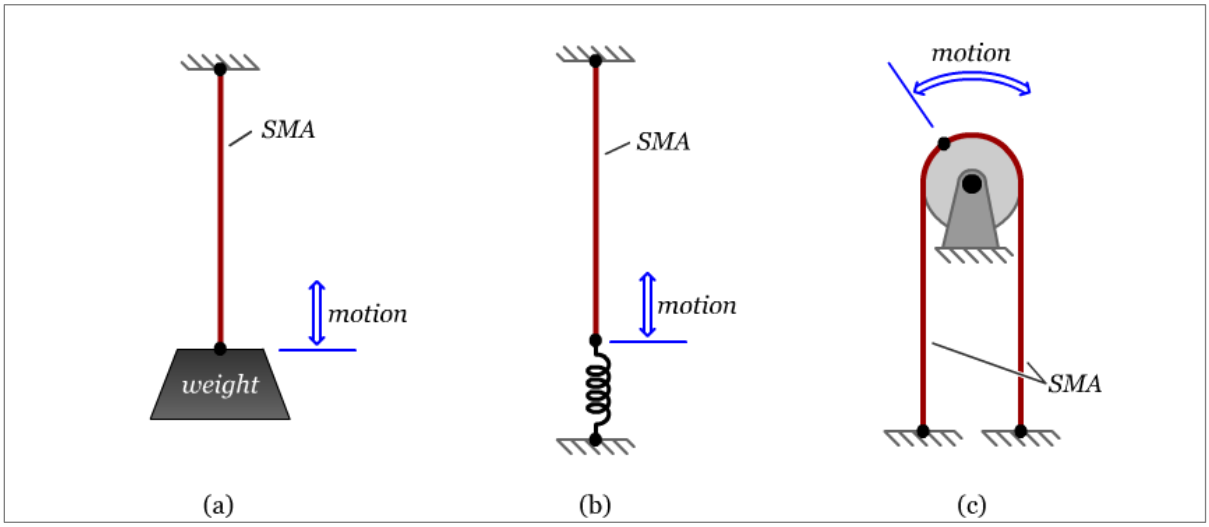

Figure 2.4: SMA actuator configurations. (a) The return force is provided by a dead weight. (b) The return force is provided by a spring. (c) Two SMA wires are connected antagonistically for active two-way motion.

The SMA actuator may be used for either “analog” or “digital” actuation. In analog actuation, the position change of the actuator load is coupled to the length change of the nitinol wire. The wire length can be controlled in an open-loop manner or it can be measured (usually directly with a linear encoder or using a pulley/rotary encoder combination) for feedback control. It is common in position control applications for the target actuator strain to be somewhere within the overall range of motion. In such cases, the nitinol wire will undergo partial transformation cycles and the minor loop behaviour of the phase transformation hysteresis has an important effect on the dynamic behaviour of the actuator system. In addition to analog position actuation, SMA actuators can also be used in a similar fashion to solenoid valve actuators for “digital actuation”, where only full phase transformation cycles are performed. Here, the nitinol wire is actuated to either its M-phase strain or A-phase strain, and the transition between these two strain values is converted to a toggle action. Unlike analog position control, partial cycling is avoided and minor loops don’t occur, resulting in a simpler controls system design. In automotive and aerospace applications, these “SMA toggle actuators” are suitable for toggling door locks, actuating latching mechanisms, or opening and closing valves. In [14] Selden *et al* also attempted to combine the flexibility of analog position control and the simplicity of binary actuation. Selden *et al* combined multiple short binary SMA actuators in a serial configuration to form a longer overall actuator so that the overall “wire strain” can be changed to one of several “digital” levels.

2.1.1 Advantages

There are a number of advantages of using wire-type SMA actuators:

Lightweight and compact: SMA actuators have a very high power-to-weight ratio (upwards of 100W/g [1]), and the SMA wire occupies very little space, making them very feasible in applications with a severe space limitation;

Simple actuation mechanism: the actuation action relies solely on the solid-state phase transformation mechanism of the SMA material which can be manufactured to be repeatable to tens of thousands of cycles, thus making SMA actuators highly reliable;

Self-sensing: the resistivity properties of the two SMA phases are different and can be measured easily to provide limited feedback of the SMA wire's phase change, without needing additional sensor hardware [3].

Some additional advantages of SMA actuators are: lower noise [1], cleanliness, high recovery stress (500MPa to 900MPa [12]), high recoverable strain [11] and low cost [11]. These make SMA actuators especially attractive in micro-robotic applications.

2.1.2 Limitations

At the same time there are practical limitations that prevent the widespread adoption of SMA actuators. First of all the hysteresis in the phase transformation behaviour means it is difficult to control the actuator position (i.e. strain of the wire) accurately without position sensors. Much of this difficulty is a result of minor loop behaviour which is dependent on the history of partial transformation cycles. Even with sensors, the consistency of the dynamic performance cannot be guaranteed. Often a hysteresis model is used for feed-forward control. However, it is difficult to find an accurate hysteresis model, and the control system is highly nonlinear and complex.

Another limitation is the low energy efficiency of SMA actuators. A typical SMA actuator can be viewed as a Carnot cycle heat engine working in a low temperature, so the upper bound on its Carnot efficiency is around 13% [15]. In reality, due to energy loss during phase transformation, the maximum power efficiency of nitinol is 3% to 4% [16]. In comparison, the efficiency of electric motors is approximately 80% [17].

A third limitation is that the SMA actuator has a low bandwidth compared to other types of actuators. The actuation speed is dependent on the rate of temperature change which is

usually limited by implementation constraints. The SMA manufacturer's datasheet would usually specify a maximum current that could be safely applied without overheating the wire and since the SMA wire is heated electrically, the heating rate would in fact be limited by the safety current. On the other hand, cooling of the SMA wire would also take place at a restricted rate since the SMA would cool only as quickly as convection would allow. Forced convection may be used to accelerate cooling. Unfortunately this cannot be done without negatively affect the heating rate in most implementations.

Finally, SMA actuators may have a short fatigue life that negatively impacts the actuators' performance as the number of cycles increase. The fatiguing of the SMA actuator is highly dependent on the stress induced by the load. Huang *et al* [12] showed that, although recovery stresses in excess of 500MPa can be achieved by nitinol, the fatigue stress is 350MPa. For repeatable performance to be achieved for a large number of cycles, the SMA actuator should be designed to operate at much lower stresses [11].

Nonetheless, these limitations are often far outweighed by the benefits of SMA actuators in specification application scenarios, such as in micro-robotics, biomedical, automotive and aerospace fields.

2.2 Feedback control of SMA actuators

For accurate position control of the SMA actuator, closed-loop feedback is used. There are many SMA quantities that could be measured for feedback in a control system, divided into two classes [1]: external variables – e.g. *displacement* and *generated force* – that are effects caused by the SMA actuator on the external environment, and internal variables – e.g. *temperature* and *electrical resistance* – that are intrinsic changes of the SMA wire.

2.2.1 External variable feedback

The most straightforward feedback would be the position (or displacement) of the load attached to the SMA actuator, since in most applications the nitinol wire changes length in order to effect positional displacement. In [8], Madill *et al* optically tracked an LED attached to the end of a nitinol wire to measure the length change, and in [18], Song *et al* embedded SMA actuators in a flexible composite beam to change the position of the tip of the beam, and used an infrared laser sensor to measure the tip position for feedback. In other experimental setups, displacement sensors such as encoders, LVDTs [1] or even simple potentiometers were used for position feedback. Combined with linear PID control laws, closed-loop position control systems are straightforward to implement and good position tracking performance can achieved for slowly time-varying reference signals.

The force generated by the nitinol wire may also be measured for feedback control, and is particularly suitable for applications where the end goal of the SMA actuator is to produce a force on a load. An example application is a robotic gripper design by Choi *et al* which uses strain gauges to measure the force produced by SMA actuators [19].

While both position and force feedback allow the quantity directly controlled to be measured, the dynamic performance of these systems may be inadequate since the nonlinear hysteresis is not always accounted for (for example in [8] hysteretic oscillatory behaviour was observed in position tracking), In addition, both the strain of the nitinol wire or the generated force change very little once the wire temperature is past A_f, so relying on position or force feedback could likely cause overheating of the wire which could not be detected

[1] A Linear Variable Differential Transformer (or LVDT), is essentially a miniature transformer with a variable core. An alternating current is driven through the primary coil, which induces a voltage in the secondary coils. The ferromagnetic core is coupled to the object whose position is to be measured, and a displacement of the object would cause the induced voltage in the secondary coils to change, thus allowing the displacement to be measured.

through feedback [1]. Finally, position and force feedback requires sensors which increase the size, or cost of the actuator system, negating the numerous benefits of SMA actuators.

2.2.2 Internal variable feedback

2.2.2.1 Temperature feedback

Having feedback of the temperature of the nitinol wire allows the temperature to be directly controlled. In [13], Russell *et al* argued that availability of the nitinol wire temperature feedback simultaneously allowed the possibility to rapidly heat the nitinol wire without overheating as well as prevent excessive heating that causes prolonged cooling time. Wire temperature may be measured using thermocouples attached to the nitinol wire; however, the small diameter of the wire and the ever-present geometry change during actuator operation make attaching a thermocouple to the wire challenging. An additional challenge is electrically isolating the thermocouple from the nitinol wire [13]. Non-contact sensing techniques such as infrared sensing may also be employed; however, these must be calibrated (often with considerable effort) to deduce the nitinol wire's absolute temperature from its infrared radiation. Another limitation of temperature feedback is the fact that due to minor hysteresis loops and the stress-dependency of transformation temperatures, the nitinol wire temperature could not be used to reliably determine its phase composition. The challenging task of obtaining an accurate measurement of the temperature of SMA wires often leads to the overall actuator system having a large size, high cost and high power consumption.

2.2.2.2 Resistance feedback

The SMA wire's electrical resistivity was reported to be one of 23 intrinsic property changes caused by the Shape Memory Effect [20]. In comparison to position, force and temperature feedback, resistance feedback has the advantages of lower system size, cost, and power consumption. Firstly, measuring the resistance of a nitinol wire does not require bulky sensor hardware as the other feedback mechanisms do, and can be easily implemented using

resistors and amplifiers in the driver circuitry that powers the SMA actuator. Secondly, the circuit design for measuring resistance is very inexpensive relative to the sensors needed for measuring position, force or temperature. Finally, resistance sensing requires only very little external power for powering voltage amplifiers. These amplifiers can be designed to have very high output impedance meaning that compared to sensor mechanisms for position, force and temperature feedback, resistance feedback draws very little external power.

At the same time, one limitation of resistance feedback is that there is a small degree of resistance-strain hysteresis [21] which would prohibit the usage of a direct resistance-to-strain mapping for position control purposes. However, as will be described in the following paragraphs, previous work focusing on the resistance behaviour of SMAs had allowed resistance feedback to be used intelligently, making SMAs an increasingly feasible actuator choice.

There has been a lot of research on using electrical resistance as feedback in a control system. In [3], Ikuta noted that the changes in the electrical resistance and the strain of a nitinol wire are approximately linear as phase transformation takes place. Ikuta then used a normalized resistance fraction value as an indirect measurement of the wire strain for controlling the SMA actuator system for an active endoscope. Because the focus in [3] was to use resistance to provide feedback during transformation, the resistance behaviour in only the transformation temperature range (i.e. $M_f < T < A_f$) was investigated and the authors did not look at the resistance change of the nitinol wire outside of that range.

In [21], the resistance-strain relationship was studied in more detail and the authors concluded that the strain-resistance relationship exhibits significantly less hysteresis than the temperature-strain relationship. A neural network to infer the SMA wire strain from the resistance feedback was combined with a PID controller for analog position control, and shown to be a feasible alternative to position feedback in some applications. Here, too, resistance was used as an indirect measurement of the wire strain.

Figure 2.5 shows the resistance-strain relationship of a Flexinol® wire that was used in this research as it is heated and then cooled. It can be seen in the 1mm to 12mm strain range (i.e. during phase transformation), the resistance-strain relationship is indeed almost linear and exhibits very little hysteresis which is in agreement with both [3] and [21].

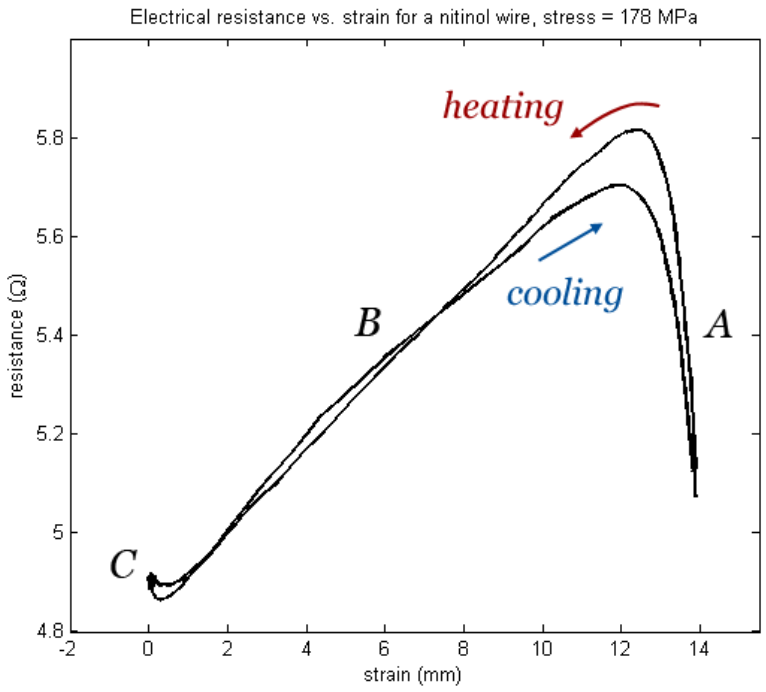

Figure 2.5: Resistance vs. strain plot for a complete heating and cooling cycle. Region "A": the nitinol wire in M-phase; region "B": during M↔A transformation; region "C": A-phase.

Another research focus for SMA actuators is reducing the response speed in toggle actuation applications. Here, precise position-tracking is not required, as only full M↔A transformation cycles are performed. Featherstone *et al* studied SMA resistance behaviour in [5] to design an intelligent heating method that allows the SMA wire to be heated faster, reducing the response time. Featherstone *et al* argued that since the wire's resistance goes from a high value to a low value during the M→A phase transformation, a threshold value resistance value can be set to signal the completion of the transformation when the

measurement resistance is below this value. This allows the wire to be heated safely using a higher current than the "maximum safe current" until this threshold resistance is reached, at which point the controller switches to a lower current to prevent over-heating. Here, the resistance measurement is once again used to infer information about the state of phase transformation.

In [2], Alliston *et al* applied a similar idea in the design of an SMA fuel injector valve actuator controller, where a resistance threshold was used to detect the completion of the M→A transformation. A large current is passed through the nitinol wire before the transformation is complete to vastly improve the actuator response time. Alliston *et al* also noted that since the resistance of the nitinol wire increases dramatically during the reverse A→M transformation, the start of the reverse transformation can be detected when the wire resistance increases past a threshold value that signals the onset of the transformation [2]. Using this knowledge, Alliston *et al* designed a method to decrease the A→M transformation time, by pre-cooling the A-phase wire so that its resistance is at this threshold value.

The work in [5] and [2] showed that using resistance feedback is a promising approach to improve the response time of SMA actuators. Furthermore, in [2], the concept of using "priming" to improve response time is introduced, i.e. bringing the SMA actuator close to the onset of phase transformation in preparation of actuation. A drawback of the controller designs of both [5] and [2] is that these designs may not work under a condition of varying ambient temperatures. The ambient temperature was assumed to be invariant during the life of the actuator, which permitted the choices of heating powers that were "large enough" to cause rapid M→A transformation. While this assumption is reasonable for the specific SMA actuator applications in [5] and [2], in general a range of dynamic ambient temperatures may be encountered for the SMA actuator. Under different ambient temperatures, a "large enough" power may over-heat the nitinol wire or not cause any transformation at all.

In [6], El Dib *et al* expanded upon the "priming concept" to make a resistance feedback based control system more robust to different ambient temperatures. Unlike [2], where

priming is used to speed up the cooling time for the A→M transformation, the control designs in [6] are designed to reduce the heating time for M→A forward transformation. Investigations conducted in [6] reveal that there exists a local maximum, or "cusp", in the resistance-temperature relationship of the nitinol wire at the onset of M→A actuation, and preheating the wire so that its resistance is close to the cusp will allow the wire to be primed for actuation. To determine the power level required to reach this resistance cusp in uncertain ambient temperature and stress conditions, an initial probing phase was implemented where the electrical power for heating the nitinol wire is increased gradually until the resistance cusp is detected. Several heuristic open- and closed-loop priming strategies are designed to keep the wire close to the resistance cusp, using the knowledge obtained during probing. All of the priming controller designs in [6] show considerable response time improvements compared to actuation without priming, thus validating the idea of priming.

Since the probing phase in [6] was designed to compensate for the uncertainty in ambient temperature and stress, the controller designs in [6] are capable of improving the actuation response time in a range of operating conditions. However, there are drawbacks yet to the controller designs in [6]. The probing phase may not be feasible for implementation for two reasons. First, the probing phase may take a long time to complete since the heating power is increased slowly during probing. It was shown in [6] that probing may last over ten seconds. Since the time of arrival of an eventual actuation signal cannot be predicted, a short probing time is desired. Secondly, it was shown in [6] that the SMA actuator had undergone partial actuation during probing. In many applications, partial actuations should be avoided prior to giving the command to actuate.

Another drawback is the fact that in [6], the priming controllers rely on knowledge obtained during probing, so the priming controllers' performance is only guaranteed under the assumption that the ambient temperature and load of the nitinol wire remain invariant between the probing and priming phases. In many applications, it is expected that in some operation scenarios, the ambient temperature or load may be time varying, so the assumption

of invariant ambient temperature and stress would be inadequate, or worse even, contradictory. For example, in an SMA-actuated door lock application scenario on a modern automobile, the ambient temperature inside the door frame would be expected to change over time as the automobile is warmed up after the initial ignition. In these scenarios, the priming control systems of [6] would need to perhaps periodically re-probe the SMA actuator, which would reduce the amount of time that the SMA actuator is available for actuation.

Nonetheless, the body of ideas presented in [6] provides an excellent basis for further research in using resistance feedback for priming SMA actuators. The research presented in this thesis seeks to improve the design of such priming controllers by developing a detailed model of the resistance behaviour of nitinol wires and applying the resistance model to design a more robust control system than the control system in [6].

2.3 Motivation for this research project

As previously mentioned, one drawback of using SMA actuators is their relatively slow response speed compared to other more widespread kinds of actuators, since the rate of strain change of an SMA wire is limited by the rate of the wire temperature change. In the past, one approach used to increase the response speed is to physically speed up the rate of temperature change. In [13], Russell and Gorbet incorporated a mobile heat sink (in the form of a metallic bar with holes drilled in it) in the design of an SMA actuator, such that the heat sink comes into contact with a nitinol wire when it is being cooled to accelerate the conductive and convective rate.

In applications where the SMA actuator is used as a toggle actuator, the response speed is also limited by the time it takes for the nitinol wire to change from its initial temperature to its transformation start temperature. In other words, if it is required for the nitinol wire to undergo a M→A transformation and the wire is initially at the same temperature as its surrounding environment, then it must take some time for the wire to be heated from the

initial temperature to its A_s temperature before the transformation starts, and that may take many seconds or even longer depending on the heating current and dimensions of the SMA wire. Furthermore, the amount of time to heat the wire to its A_s temperature depends on ambient temperature. In addition, the stress on the wire also changes the transformation start and finish temperatures so the time it takes to heat the wire prior to transformation would also depend on the wire stress.

In many application areas, such as the automotive industry, this inexact "pre-transformation heating" time is undesirable, as it may cause delay and a large degree of uncertainty in the performance of the system in which SMA actuators are used. [2] and [6] developed the concept of "priming" to deal with this problem specifically. In the control systems of both [2] and [6], the ambient temperature and stress of the wire were assumed to remain constant during operation – an assumption that is not always appropriate for SMA actuator applications in general.

If the actuator system could be designed such that the actuation time can be made consistently small independent of stress and ambient temperature variations, then an SMA actuator – given its benefits – would become a much more attractive design choice than other actuator types. Therefore, the focus of this research is to design a control system whose aim is to minimize the pre-actuation heating time and achieve consistent actuation times across a range of ambient temperature and stress conditions.

Chapter 3

Design objective, requirements and criteria

The goal of this research is to synthesize a design for an SMA actuator control system. In this chapter, the objective of the priming controller design is defined first in Section 3.1. Then, the requirements and the criteria for the controller are presented in Sections 3.2 and 3.3 respectively.

3.1 Objective

As noted in Chapter 2, the response time of toggle-type SMA actuators can be improved dramatically with the concept of "priming", i.e. a control system that pre-emptively brings the SMA actuator close to the onset of actuation, prior to receiving the actuation command. In [2], priming has been applied to a high degree of success, however with the assumption that the ambient temperature and stress conditions remain constant throughout the life of the SMA actuator. In [6], the possibility of different (but constant) ambient temperatures is accounted for and compensated by incorporating a probing phase that intelligently determines a input power which allows the SMA actuator to be maintained in a "primed state". The objective of this research, as an extension to [6], is to design a priming controller with the ability to compensate for, or adapt to, an operating condition where both the ambient temperature and the stress of the nitinol wire change over time. The goal of the priming controller is to reduce both the duration as well as the variability of the actuation time across the range of ambient temperature and stress conditions, without using a probing phase.

The SMA actuator for which the priming controller is designed is of the dead-weight bias force type, where the weight of the load provides the return force necessary for wire extension during the A→M transformation. In addition, active actuation of the nitinol wire is achieved with the M→A phase transformation caused by heating the wire, so the priming controller is designed for the M→A transformation.

3.2 Design requirement

The research presented here is geared toward developing a readily implementable controller algorithm for toggle-type nitinol wire SMA actuators in real-world applications. As such, several requirements can be formulated that will make the controller design feasible for implementation.

Requirement #1: the controller design should not require costly or cumbersome sensor hardware.

Because one of the main advantages of SMA actuators compared to other kinds of actuators is its compact form factor, incorporating (relatively) bulky and costly sensors for feedback control would negate this advantage and make SMA actuators a less desirable design choice.

Requirement #2: the controller design should avoid causing unintended actuations.

The primed actuator would, by its very nature, be on the verge of undergoing transformation, so it is very important that the control system does not cause the phase transformation to occur prematurely. Unintentional actuations should be avoided not only in unchanging environmental conditions, but also in situations where the ambient temperature and stress are time-varying.

Requirement #3: the control system should avoid undergoing a lengthy probing phase for determining priming controller parameters.

The probing phase of the control system of [6] negatively impacts the feasibility of the SMA actuator design, since it is time and energy consuming, causes premature actuation, and cannot accommodate for disturbances in the ambient temperature and stress during operation. If disturbances in these quantities are expected, then re-probing would be required. The frequency of re-probing is positively correlated with the speed and frequency of changes in the ambient temperature and stress, so the amount of time that the SMA actuator is available for actuation (i.e. when it is not probing) can be severely limited.

3.2.1 Satisfying the design requirements

To satisfy requirement #1, the SMA actuator implementation used in this research uses resistance feedback for the control system since it was shown that resistance feedback has the least size, cost and power consumption compared to position, stress or temperature feedback. Additionally, the ambient temperature is also measured for feedback in the priming controller. The inclusion of ambient temperature feedback is justified for two reasons: a) the ambient air temperature can be measured easily and does not suffer from the same measurement difficulties as the temperature of a nitinol wire; and b) in many applications (for example in automotive applications), a measurement of the ambient temperature is already available, so including ambient temperature feedback for the SMA actuator control system does not incur additional size, cost or power consumption penalties. In systems where there isn't a pre-existing ambient temperature measurement mechanism, a thermocouple can be used to provide a fast and accurate measurement of the ambient temperature.

The priming controller design in this research relies prominently on feedback of the resistance of the nitinol wire, so noise in the resistance feedback signal may negatively affect the quality of priming. To satisfy requirement #2, a noise filtering algorithm to generate a clean resistance feedback was used in [6]. Here, the electrical system of the overall SMA actuator system is designed with the specific goal of providing voltage signals that allow the effects of noise to be rejected in the calculation of the nitinol wire's resistance.

Finally, to satisfy requirement #3, the controller design determines the required power for priming the SMA wire in real-time, without an initial probing stage. To do this, a model is developed to describe the resistance behaviour of SMA wires, and an inverse model based on that is implemented as part of the controller to use the real-time resistance feedback to determine the required wire temperature.

3.3 Performance criteria

In addition to the requirements outlined in Section 3.2, there are a few criteria based on which the priming performance of the controller design can be evaluated.

Criterion #1: Quality of priming

The controller design can be evaluated on how well the SMA wire is primed, i.e. the quality of priming. Because the objective of the priming concept is to minimize the amount of heating required to bring the SMA wire to the onset of actuation, a good metric is the time it takes for a wire in the primed state to begin the phase transformation once the actuation command is given. In [6], this time duration is called “Time-To-Cusp”, and here a similar metric will be used to judge the quality of priming.

Because the priming controller here will have the additional task of dealing with varying ambient temperature and stress conditions during priming, another useful metric for judging the quality of priming is the variation in strain during priming. A good priming controller design will compensate for the condition of varying ambient temperatures or stresses effectively and keep the nitinol wire at an approximately constant strain (i.e. the strain at the cusp of actuation) prior to actuation, which would result in a low variation in strain while the primed state is maintained. Note that this metric is applicable only in operational regimes where the stress is relatively constant, since a changing stress will naturally cause the wire strain to change as well due to the finite elastic modulus of nitinol.

The length change of the wire is measured experimentally using a rotary encoder. The length change is measured only for the purpose of evaluating the performance of the priming controller, not for feedback for the priming controller to work, in accordance with *Requirement #1* in Section 3.2.

Criterion #2: Repeatability of priming

The controller can be also evaluated on how repeatable the priming performance is under the same ambient temperature and stress conditions. This can be accomplished by performing experimental trials multiple times under the same ambient temperature and stress conditions and analyzing the statistical variations of the quality of priming metrics.

Criterion #3: Consistency of priming

A main goal that the controller design pursued in this research is that performance should be robust to unpredictable changes in the external environment of the actuator. The robustness of the control system design can be evaluated by comparing the consistency of the quality of priming metrics under both different but invariant ambient temperature and stress conditions as well as time-varying conditions. Here, "different/invariant conditions" means each experimental trial may have different ambient temperature and stress values but they remain constant over the course of each trial; while "time-varying conditions" means that all trials may have different ambient temperature and load values from each other and the conditions may also change during the course of each trial.

Chapter 4

Experimental design

The work presented in this research is geared heavily toward physical applications; therefore much of the research is experiment-based. Much of the research extend upon the concept of priming as presented by El Dib *et al* in [22], so the same mechanical set up as [22] is used as the experimental testing platform, though with minor modifications. The mechanical platform is specifically designed to simulate the range of operating conditions in physical applications, and the electrical platform is optimized for implementing the software control system. At the same time, the focus is on developing a high-level controller algorithm that is implementable on an electronic system instead of optimizing the efficiency of the electronic system itself. Unlike [22], where an industrial-grade microcontroller was used for the control system, the design, and implementation priming controller in this research is done through the MATLAB/Simulink environment instead of an industrial-grade microprocessor.

This chapter serves as a high-level summary of the mechanical, electrical and software platforms on which experimental work were conducted, and is organized as follows: The mechanical set up of the experimental test-bed is presented, followed by a description of the electrical system design. Lastly, the design of the software environment in which the priming controller will operate is summarized. Figure 4.1 is a diagram of the overall SMA actuator experimental platform used in this research. Details on the design and implementation of the electrical and software component are presented in Appendix A.

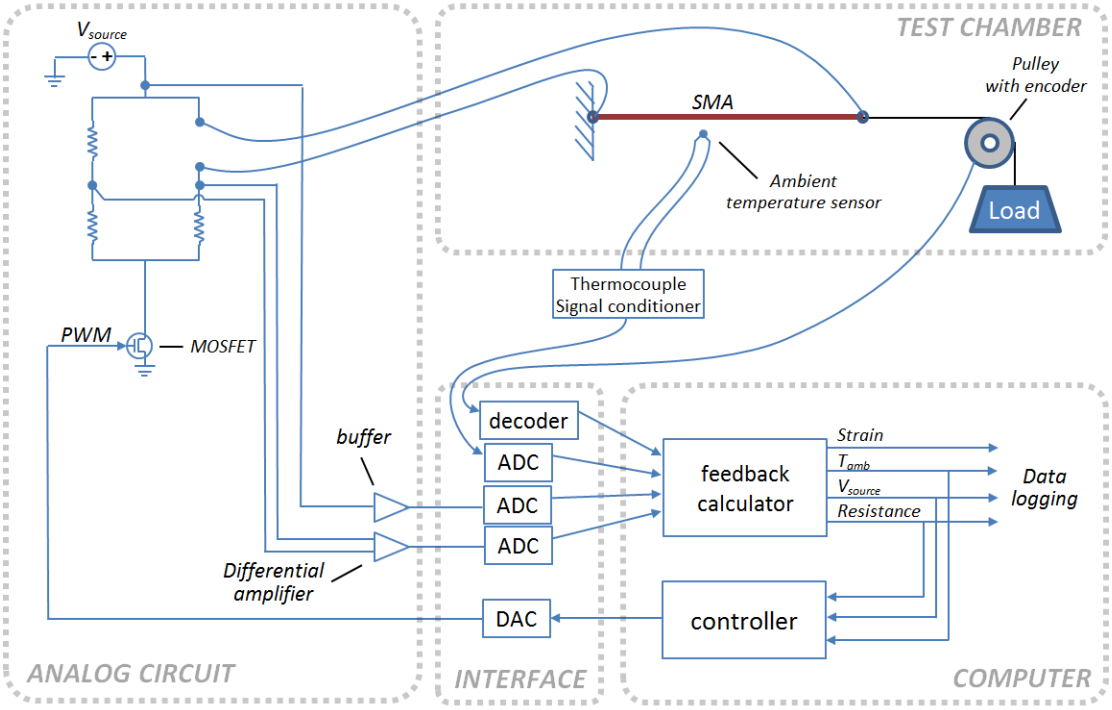

Figure 4.1: Overall block diagram of the SMA actuator system.

4.1 Mechanical platform

As shown in Figure 4.2, the freezer compartment of a refrigerator is used as a controlled environmental chamber to house the SMA actuator mechanism. The actuator mechanism consists of a 28.3cm Flexinol® SMA wire (length measured under 178MPa load) manufactured by Dynalloy Inc., mounted horizontally to a fixed aluminum frame at one end and a high-strength wire at the other end. The high-strength wire is attached to a load cage around a pulley. The stress on the SMA wire can be adjusted by placing various amounts of weight in the cage. While position feedback is not a part of the design of the control system developed in this research, a US Digital H5S-1024 rotary shaft encoder is used to provide experimental measurement of length change of the SMA wire. The two ends of the SMA wire are electrically connected to the SMA driver circuit for Joule heating.

The temperature of the chamber can be controlled between -30°C to 40°C (with 0.1°C resolution) using an OMEGA CN7800 temperature controller. The temperature controller uses a thermocouple placed 2cm away from the SMA wire to measure the ambient temperature of the air surrounding the SMA. The OMEGA CN7800 uses bang-bang controller to maintain the air temperature within a ±2.5°C hysteresis band around the temperature setpoint, by either turning on an incandescent light bulb or activating the refrigeration system. The compressor fan (part of the refrigeration system) is kept turned on at all times regardless of whether or not the refrigeration is active, in order to maintain a constant convection rate throughout the experiments. Finally, a separate thermocouple is also placed 2cm away from the SMA wire and provides the ambient air temperature feedback to the computer.

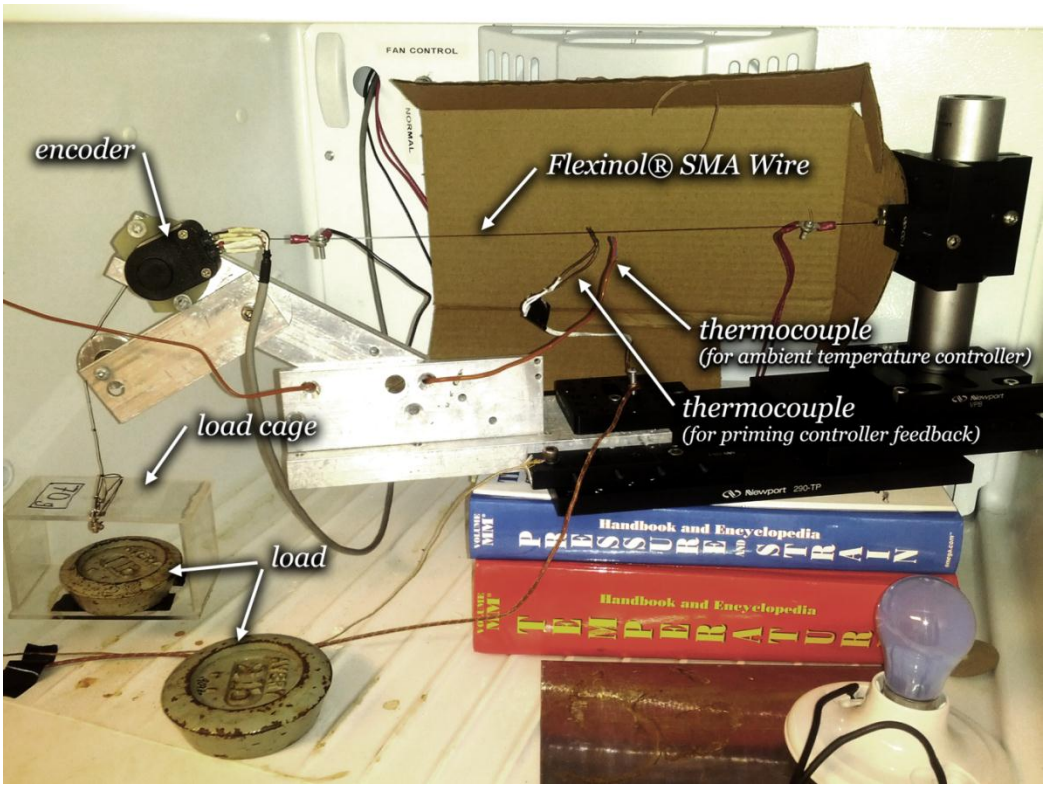

Figure 4.2: Annotated photograph of the experimental setup inside the freezer compartment of a refrigerator.

4.2 Electrical system

An electrical system was designed for providing the power to drive the SMA actuator as well as allowing various physical quantities in the SMA actuator to be accurately measured. Specifically, the electrical system can be divided into four sections:

- *SMA driver circuit*: this circuit is used for simultaneously heating the SMA wire using a DC source, and for measuring the SMA wire resistance via a Wheatstone bridge circuit. Two voltage measurements are taken from the SMA driver circuit to allow the SMA resistance (R_{sma}) to be computed: the source voltage V_s and the Wheatstone bridge differential voltage V_d. Pulse width modulation (PWM) is used to adjust the power delivered to the SMA wire for heating.

- *Signal amplification circuit*: this circuit is used to amplify the V_s and V_d voltage measurements from the SMA driver circuit before they are sent to the data acquisition board.

- *Other feedback signals*: as noted in Section 4.1, an encoder is used for measuring the SMA wire length change and a thermocouple is used for measuring the ambient air temperature inside the test chamber. Output signals from these sensors are collected by the computer via the data acquisition board.

- *Data Acquisition*: a Quanser MultiQ-PCI data acquisition board is used for interfacing the electrical system with the computer.

The technical details of the design and implementation of the electrical system can be found in Appendix A.

4.3 Software system

The software for controlling, driving, collecting data from the experiment and processing that data is designed to be self-contained in the MATLAB/Simulink environment. As shown in Figure 4.3, the software system can be divided into 3 subsystems, the *PWM driver*, *Data processor*, and *controller*. The PWM driver subsystem is responsible for adjusting the heating power for the SMA wire based on the control signal generated by the controller; the data processor is responsible for calculating the resistance of the SMA wire, R_{sma}, and relaying feedback signals V_s, R_{sma} and T_{amb} to the controller; the controller is responsible for generating the control signal for "priming" and actuating the SMA wire. The implementation of the PWM driver and data processor subsystems are presented in Appendix A; while the design of the controller subsystem are explained in detail in Chapter 6.

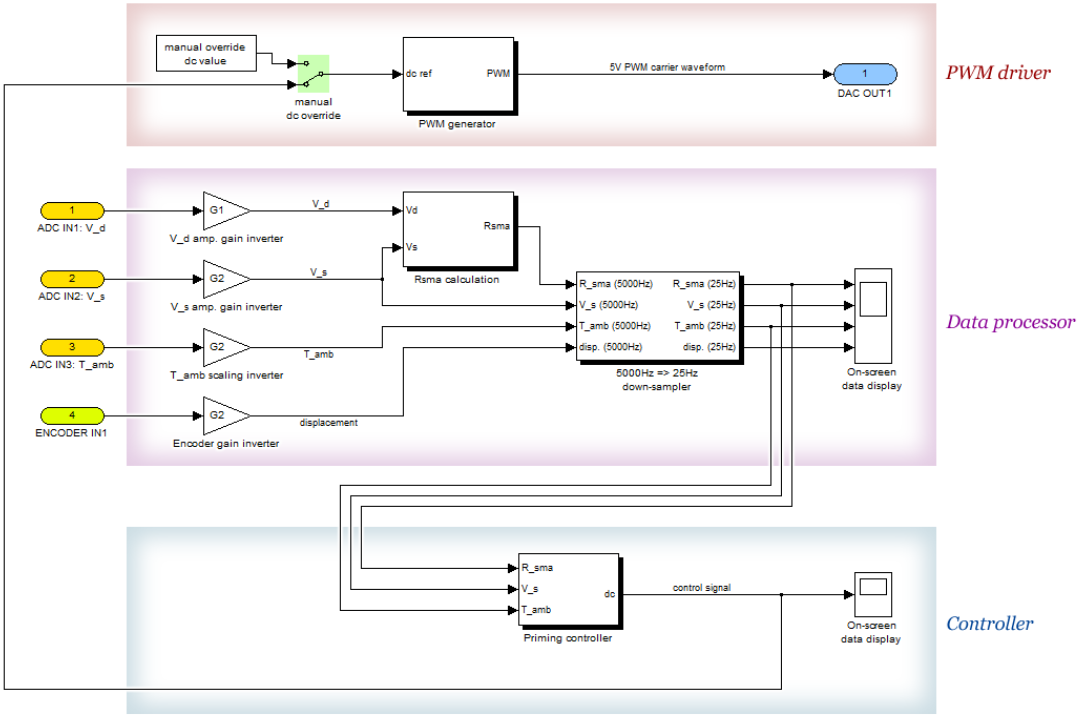

Figure 4.3: Software system block diagram.

Chapter 5

Resistance modelling of the SMA actuator

In this research project, the overall goal is to design an SMA priming controller that uses resistance feedback. A plant model of the SMA actuator system is desired for three reasons:

1. By developing a model which accurately describes the resistance behaviour of the SMA actuator, a deeper understanding of the SMA's behaviour can be obtained. Using this knowledge, the priming controller can be better designed.

2. Having a model will allow a simulation of the SMA actuator system to be created. Using the simulated system, feedback control algorithms can be safely tested before they are implemented on the physical system. It will also allow the dynamics of the closed loop system to be studied, and designs iterated much more rapidly than via only experimental testing.

3. An inverse model can be devised from the forward model and integrated into the priming controller design. Since the feedback signal is the SMA resistance, the controller algorithm may use the resistance feedback and the inverse model to calculate unknown or uncertain variables in the system.

This chapter is organized as follows: a literature review of some of the existing approaches to resistance modelling feedback is presented in Section 5.1; the design of the SMA resistance model equations is explained in Section 5.2; Section 5.3 describes in detail the

experimental procedures for identifying model parameters and finally Section 5.4 presents the experimental results as well as the numerical values of the model parameters.

5.1 SMA resistance modelling literature review

Since the late 1980's, there has been a continued interest in using the electrical resistance (ER) of an SMA actuator as feedback for controlling the strain of the actuator. In [3] Ikuta *et al* investigated the changes in ER of a nitinol wire as the wire underwent phase transformation, and although no analytical model was formulated to predict the ER behaviour given inputs, they did provide a method for interpreting the data: as the nitinol wire undergoes the M→A phase transformation, the ER transitions smoothly from a maximum resistance value to a minimum value. This range of resistance variation is then normalized to a value between 0 to 1 and used as an indirect indicator of ξ_M, the Martensite phase fraction, i.e.:

$$\xi_M = R_{normalized} \tag{5.1}$$

where $R_{normalized}$ represents the normalized SMA resistance.

Using the above relationship Ikuta *et al* designed a position controller using resistance feedback only for an antagonistic type SMA actuator consisting of two nitinol wires. [3] showed that the control system was very successful in tracking a square position reference signal, although the response speed was limited. Unfortunately, the behaviour of commercial SMA wires nowadays appears to differ vastly from [3], to such an extent that the relationship of (5.10) developed in [3] would not be readily applicable. In particular, it was stated in [3] that there is very little hysteresis in the resistance-temperature curve of nitinol wires, while more recent publications [23, 24] show that the hysteresis width is comparable to that found in the strain-temperature function. It is also shown in [23, 24] that with currently commercially available nitinol wires, the resistance first increases prior to the onset of M→A phase transformation, which is contradictory to the data shown in [3] where the pre-

transformation resistance increased was not observed. Nevertheless, an important contribution of [3] is establishing the concept that the ER of an SMA wire actuator transitions from some kind of a maximum to a minimum when the SMA itself undergoes the complete M→A phase transformation.

In [21], Ma *et al* expanded upon the idea of using resistance feedback for position control. Instead of simply using a linear mapping to compute the nitinol wire strain from the wire resistance as was done in [3], Ma *et al* used experimental resistance and strain data, as shown in Figure 5.1, to construct mappings between resistance and strain which, compared to [3] take additional account of stress and partial transformation loops. Based on the collected data, Ma *et al* trained a neural network to predict the strain of the wire and incorporated the neural network in a position controller. Using only resistance as feedback, the controller design in [21] showed an average steady state error of 7% for a stepped position reference signal.

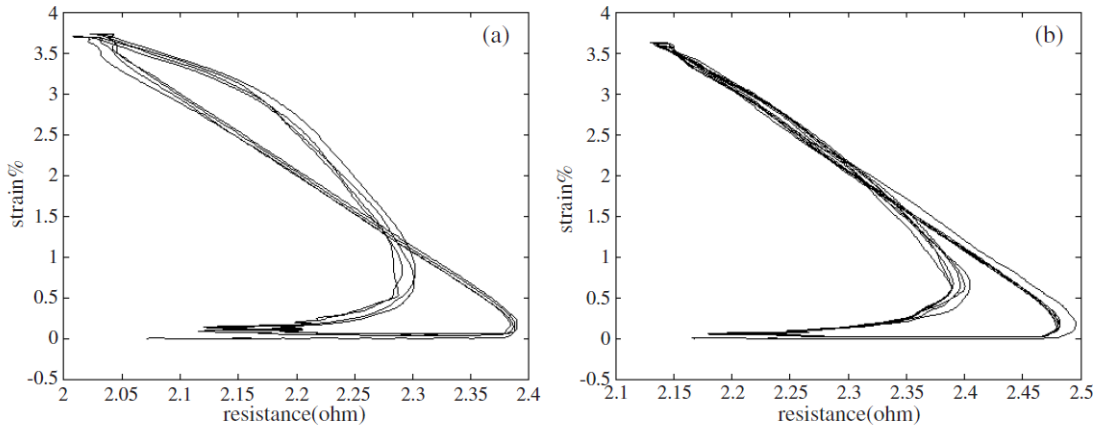

Figure 5.1: Strain vs. ER (a) under small pre-tension and (b) under large pre-tension. Multiple complete transformation cycles shown. Figure reproduced with permission from the copyright holders of [21].

Both [3] and [21] show that resistance feedback can be used legitimately to infer the nitinol wire strain. Furthermore, both also show that the relationship is mostly linear during heating,

and the strain-resistance hysteresis is much smaller than the strain-temperature hysteresis. Figure 5.2 shows the resistance-strain relationship for the Flexinol® wire used in this research. It is very similar to the resistance-strain relationship shown in [21].

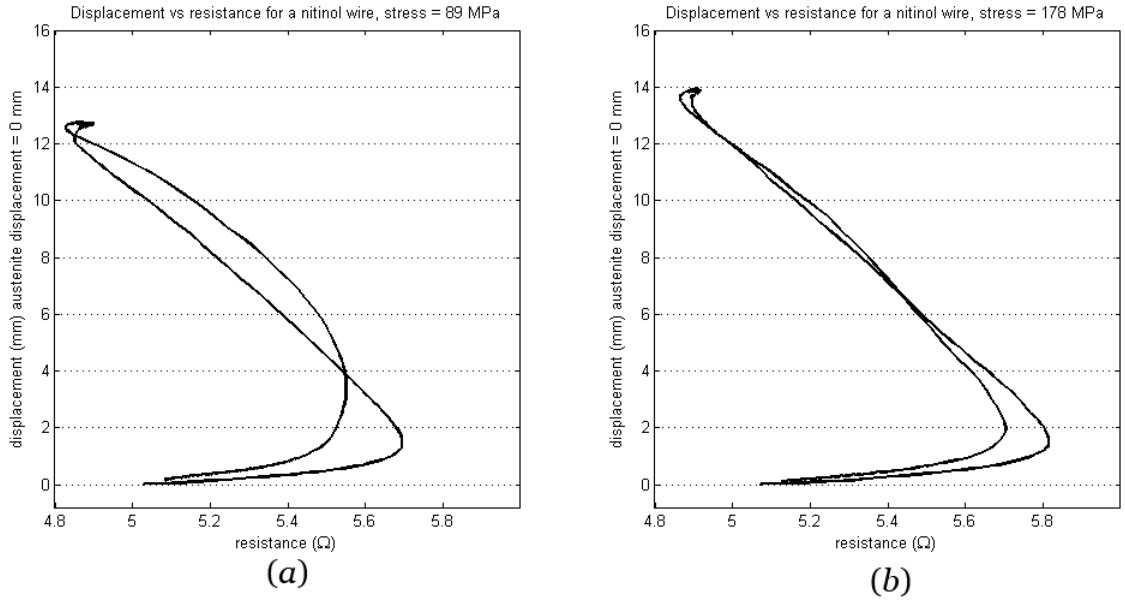

Figure 5.2: Resistance vs. strain plot for a complete heating and cooling cycle. (a) low stress on the nitinol wire. (b) high stress on the nitinol wire.

While [3, 21] demonstrated the usefulness of resistance feedback for position control, neither had developed a mathematical model to explain the resistance behaviour of nitinol wires. A more recent paper by V. Novák *et al* [23] attempted to develop such a model. In [23], V. Novák *et al* considered the overall resistivity characteristics of an SMA wire to be a linear combination of individual resistivity behaviours of each of the M-, R- and A- phases. Depending on the phase composition of the wire, the contribution of the resistivity function of each of the three phases to the overall resistivity would vary, and the weighted average of the three resistivity functions is the total resistivity of the nitinol wire, ρ_{tot}, according to (5.2):

$$\rho_{tot} = \rho_A(1 - \xi_R - \xi_M) + \rho_R\xi_R + \rho_M\xi_M \tag{5.2}$$

where ξ_R and ξ_M are the R- and M-phase fractions respectively, and ρ_A, ρ_R, ρ_M are the resistivity functions of the A-, R- and M-phases respectively. These three functions are calculated according to (5.3) to (5.5):

$$\rho_A = \rho_{0A} + (T_{0A} - T)\frac{\partial \rho_A}{\partial T} + \sigma\frac{\partial \rho_A}{\partial \sigma} \tag{5.3}$$

$$\rho_R = \rho_{0R} + (T_{0R} - T)\frac{\partial \rho_R}{\partial T} + \sigma\frac{\partial \rho_R}{\partial \sigma} + (90 - \alpha_R)\frac{\partial \rho_R}{\partial \alpha_R} + \varepsilon_R^{tr}\frac{\partial \rho_R}{\partial \varepsilon_R^{tr}} \tag{5.4}$$

$$\rho_M = \rho_{0M} + (T_{0M} - T)\frac{\partial \rho_M}{\partial T} + \sigma\frac{\partial \rho_M}{\partial \sigma} + +\varepsilon_M^{tr}\frac{\partial \rho_M}{\partial \varepsilon_M^{tr}} \tag{5.5}$$

where T and σ are the nitinol wire's temperature and stress respectively, ρ_{0i} $(i = A, R, M)$ are "base" resistivity of individual phases measured at temperatures T_{0i}, $\alpha_R$the rhombohedral distortion of the R-phase and ε_M^{tr} and ε_R^{tr} are "transformation strains" induced by the martensite and R-phase, respectively [23]. All other quantities, represented by the partial derivative terms, are constant coefficients that specify the resistivity functions' dependency on T, σ, α_R, ε_R^{tr} and ε_M^{tr}, and were all identified experimentally in [23]. A micromechanical model [25], developed by the same researchers, allows ξ_R, ξ_M, α_R, ε_R^{tr} and ε_M^{tr} to be calculated. Overall, the independent inputs to the resistivity model are temperature and stress and the output is the resistivity of the SMA wire. Taken from [23], Figure 5.3 shows the experimental and simulated electrical resistivity as a function of the nitinol wire temperature and stress.

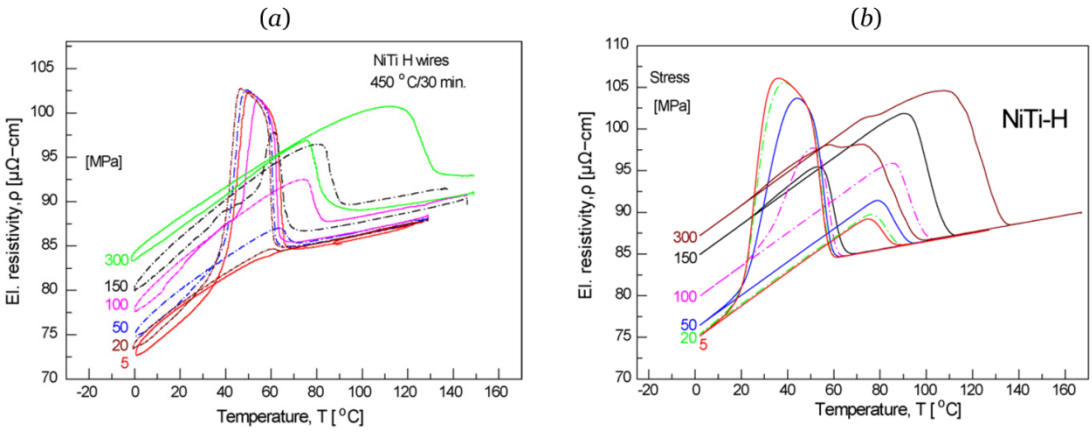

Figure 5.3: Variation of the electrical resistivity for the case of thermal cycling at various constant applied stresses. (a) Experimental (b) Simulated. Figure reproduced with permission from the copyright holders of [23].

Some notable features of this model include:

- Upon heating, the resistivity of the nitinol wire undergoes a linear increase, then peaks, then drops to a minimum, and then finally a slower linear increase. The maximum-to-minimum resistivity drop during heating is attributed to the M→A phase transformation. Upon cooling, the resistivity behaviour is reversed from that of heating, however due to hysteresis, the temperature at which minimum and maximum resistivity occurs are shifted downwards.

- At very low stress levels (stresses up to 100 MPa), R-phase is generated during A→M transformation. R-phase has a high resistivity compared to M- and A-phase, which causes a large peak in the resistivity graph during cooling.

- In both the M- and A- phase temperature regions (i.e. not in the phase transformation zone), the resistivity model exhibits a linear and positive resistivity-temperature relationship, represented in the model as the temperature-dependency coefficients $\partial\rho_M/\partial T$ and $\partial\rho_A/\partial T$, with the A-phase coefficient lower than the M-phase coefficient. The values of the coefficients do not change with stress. (the same temperature-dependency

coefficient for R-phase was also identified, but [23] never specified how it was determined, given that the nitinol wire never enters a stable R-phase). In [23], the linear resistivity-temperature behaviour is attributed to the fact that, like most other metals, the resistivity of each phase becomes higher as the temperature of the material is increased.

- Increasing stress levels positively offsets the absolute resistivity in M-phase.
- Increasing stress levels also shift up the temperatures at which the maximum and minimum resistivity peaks occur. This is consistent with the fact that the phase transformation temperatures increase as load increases.

In a paper by John Shaw *et al* [24], similar trends of resistivity-temperature behaviour to [23] are observed. There are a few notable results when compared to [23]:

- In [24], Shaw *et al* did not try to fit a mathematical equation to the resistivity-temperature-stress data that they experimentally collected; Novak *et al* did develop a predictive model in [23].
- Comparing the experimental data, the M-phase resistivity of the SMA in [23] is around 10% lower than in [24] for all stresses. However for moderate to high stresses (>150MPa) the simulated resistivity in [23] matches the experimental data in [24].
- Shaw *et al* included data on how the resistivity behaviour evolves as the number of heating-cooling cycles increases. Both the magnitudes of the resistivity peaks and the temperature hysteresis decrease as the number of heating-cooling cycles on a single wire is increased [24].

While no useful formulae can be extracted from the John Shaw paper [24], the relationship between resistivity, temperature and stress as presented in [24] is mostly consistent with that in [23]. The differences between the John Shaw paper and the Novak paper could be attributed to different experimental methods and alloy composition.

5.2 Developing a model for the in-fridge experiment

The mathematical model from [23] is an intuitive approach to describing the electrical resistivity characteristics of nitinol wires; therefore a modified version of that model is used to model the SMA resistance in this project. There are several differences between this research and [23] that warrant a modification of the resistivity model of [23].

- The Flexinol® wire used in this research has an almost exactly 50%-50% Ni-Ti composition, while the NiTi-H wire used in [23] has a Ti-Ni ratio of 54.5%-45.5%.
- The goal of resistance model here is to allow an inverse model to be developed that allows the SMA actuator's resistance to be used for feedback control, so the resistance will be the output of the model instead of resistivity.
- Unlike [23], in this research only the M→A transformation is investigated, in which R-phase does not form, so R-phase will be ignored.
- In [23], ξ_R, ξ_M, α_R, ε_R^{tr} and ε_M^{tr} are also calculated using a detailed and highly complex micromechanical model [25]. For this research, because we only need to consider major loop behaviour, a relatively simple phase fraction model will be used for describing ξ_M; while the α_R, ε_R^{tr} and ε_M^{tr} terms in (5.3) to (5.10) will be omitted.

A thermodynamic model and a phase fraction model are also created that work synchronously with the resistance model to fully describe the resistance behaviour of the SMA actuator used in this research project.

It should be emphasized that since the control system in this research is designed for priming SMA toggle actuators where only major loop behaviour needs to be considered, it is sufficient to use a relatively simple equation to describe the shape of the phase transformation major loop, as will be described in Subsection 5.2.3.

5.2.1 Resistance model

A modified version of the resistivity model in [23] is used for describing the resistance behaviour of the SMA actuator system, as shown in Equations (5.6) to (5.8):

$$R_{tot} = R_M \xi_M + R_A(1 - \xi_M) \tag{5.6}$$

$$R_M = R_{0M} + (T - T_{0M})\frac{\partial R_M}{\partial T} + \sigma \frac{\partial R_M}{\partial \sigma} \tag{5.7}$$

$$R_A = R_{0A} + (T - T_{0A})\frac{\partial R_A}{\partial T} + \sigma \frac{\partial R_A}{\partial \sigma} \tag{5.8}$$

where R_{tot} is the total resistance of the SMA wire, R_M and R_A are the M- and A- phase resistances respectively, ξ_M is the martensite phase fraction, T is the temperature of the wire, σ is the wire stress, and all other symbols are parameters (see Table 5.1). There are eight parameters in total and they need to be identified empirically.

Table 5.1: Resistance model parameters.

Parameter	Description
$R_{0M}(R_{0A})$	Nominal wire resistance in martensite (austenite) phase
$T_{0M}(T_{0A})$	Temperature at which the nominal resistances were measured
$\partial R_M/\partial T\ (\partial R_A/\partial T)$	Linear temperature dependence of martensite (austenite) resistance
$\partial R_M/\partial \sigma\ (\partial R_A/\partial \sigma)$	Linear stress dependence of martensite (austenite) resistance

Equations (5.6) to (5.8) calculate the resistance of the SMA based on three independent variables of the SMA: stress σ, temperature T and martensite phase fraction ξ_M. Unfortunately T and ξ_M cannot be measured physically on the experimental setup so in order to be able to use the model at all T and ξ_M must be estimated with the thermodynamic model and phase fraction model respectively.

5.2.2 Thermodynamic model

In [8, 6], a convective model was used to predict the temperature of nitinol wires in the absence of temperature sensors. In this research, the same model is adopted with slight parameter variations. The temperature dynamics of the nitinol wire can be estimated using (5.9) and (5.10):

$$CV\rho\frac{dT}{dt} = P(t) - hA(\Delta T(t)) \tag{5.9}$$

$$P(t) = \frac{V_s(t)^2}{R_{sma}(t)} \cdot dc(t) \tag{5.10}$$

where the time-varying variables are defined in Table 5.2 and parameters are listed in Table 5.3. The parameters in Table 5.3 are assumed to be constant during the operation of the SMA actuator.

Table 5.2: Thermodynamic model variables.

Variable	Description
$P(t)$	Power consumed by the SMA (W)
$\Delta T(t) = T - T_{amb}$	Wire temperature above ambient (°C)
$V_s(t)$	Source voltage (V)
$R_{sma}(t)$	Computed wire resistance (Ω)
$dc(t)$	PWM driver duty cycle(%)

Table 5.3: Thermodynamic model parameters.

Variable	Value	Description
ρ	6.45×10^{3} kg/m^3 [11]	Nitinol density
C	465.2 J/(kg °C) [11]	Specific heat
V	1.434×10^{-8} m^3	Wire volume
h	131 W/(m^2 °C)	Convection heat transfer coefficient

A	2.258×10^{-4} m^2	Wire surface area

Taking the Laplace transform on (5.9) yields the following first-order transfer function:

$$T(s) = \frac{\frac{1}{CV\rho}}{s + \frac{hA}{CV\rho}} P(S) \tag{5.11}$$

Note that parameters ρ and C are taken from the data sheet of the SMA wire, V and A are calculated from the SMA wire's physical dimensions and h is calculated using experimental data. The parameter h is dependent on the characteristics of the air flow around the SMA wire, modelled thermodynamically as a horizontal cylinder. It is important to determine a value for h that is accurate for the experimental set up in this research project for two reasons:

- Given a constant input power P, the estimated wire temperature T at steady state would be at different values given different h values. It will be seen later on that the resistance model parameters in Table 5.1 are determined using steady state regime R_{sma}-T datapoints so the accuracy of h directly contributes to the accuracy of the parameter values.

- It will also be seen in Chapter 6 that the thermodynamic model is also used by the controller to perform on-line estimation of the temperature of the SMA wire, so it is important that the transient behaviour of the temperature of the SMA wire is modelled accurately. As shown in (5.11), the time constant of the system is directly affected by the numerical value of h.

The literature shows much variation in the convection coefficient. For example, in [8], h = 70W/(m^2°C) for an SMA wire while in [26] h = 150W/(m^2°C). Since the rate of convective heat transfer is very much dependent on the movement of the air surrounding the SMA wire, the discrepancy in h can be attributed to different experimental conditions. An h value of

131W/(m^2°C) was calculated based on an iterative method using experimental data, and a detailed description of that method can be found in Subsection 5.3.1.

5.2.3 Phase fraction model

In addition to the wire temperature *T*, the martensite phase fraction ξ_M must also be estimated in order to use (5.6) to model the SMA resistance. In general, the martensite phase fraction is difficult to model mathematically because of the hysteresis in the ξ_M-T function. However in this research project, the focus is specifically on the heating side of the major loop and we do not have to deal with the hysteresis, so a relatively simple model can be used. Equation (5.12) is adopted from [9] to model the gradual transition from M-phase to A-phase:

$$\xi_M = \frac{1}{1 - e^{a(T - b\sigma - c)}} \tag{5.12}$$

where ξ_M is the martensite phase fraction, T is the wire temperature, σ is the wire stress and a, b, c are constants. The "width" of the phase transformation temperature range is controlled by a; while b and c define the temperature of the point of inflection of the martensite phase fraction curve.

Note that equation (5.12) was chosen since it had been used regularly in the past to analytically describe the shape of the phase transformation major loop, albeit with slightly different parameter symbols [8, 9].

The parameters are determined experimentally using strain data and the procedure is presented in detail in Subsection 5.3.2.

5.3 Experimental identification of parameters in the resistance model

To identify the parameters in the SMA resistance model, experimental trials are performed to collect Resistance-Temperature data. In these trials, the SMA wire stress is held constant across all trials but the PWM duty cycle of the SMA driver is set to a range of different values to allow the SMA to reach different steady state temperatures. During each trial, the V_s, dc, R_{sma}, and strain data are collected.

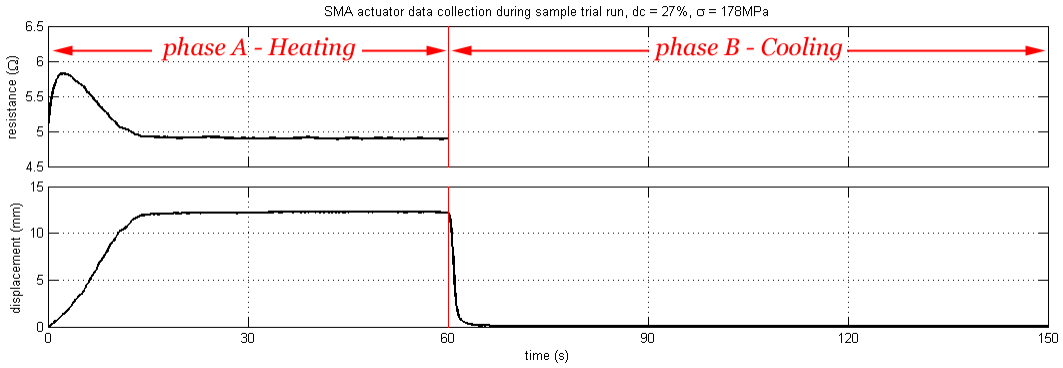

Figure 5.4: Sample trial run for identifying parameters in the SMA resistance model. Each trial is divided into two phases, phase "A" and phase "B".

As illustrated in Figure 5.4, each trial run is divided into two phases. The wire is first heated by the SMA driver for 60 seconds with a preset heating duty cycle dc_{high} ("phase A") followed by 90 seconds of applying 0% duty cycle ("phase B") to allow the wire to cool completely to the ambient temperature prior to the next trial run. The set dc_{high} values is 1.5% to 17.5% in 1% increments, and 18% to 35% in 0.5% increments. Each of these dc_{high} values allow the SMA wire to be heated to a different temperature when steady state is reached at the end of "phase A". The order of these trial runs is randomized to prevent data skewing that may result from incomplete cooling in-between trials.

Four sets of trials are performed in total, each for a different stress as summarized in Table 5.4. These stresses correspond to the typical range of operating stress levels of the SMA wire actuator.

Table 5.4: Resistance model identification test stress settings.

Set #	**1**	**2**	**3**	**4**
Load (g)	460	652	920	1375
Equiv. stress (MPa)	89	126	178	266

For each trial in each set, the V_s, dc, R_{sma}, data are post-processed to estimate the wire temperature for the entire duration of each trial. The resistance and temperature values achieved at steady state of all trials in each set are then used to generate an overall resistance-temperature function for that stress level. This set of trials is then repeated for different SMA wire stress levels to generate a family of resistance-temperature functions. The model parameters listed in Table 5.1 can then finally be identified by examining the resistance-temperature curves.

Since in these experimental trials we can only collect data for wire temperatures above the ambient temperature, a low ambient temperature was used for all trials so the model can be applied to most real-world applications where the operating ambient temperature is above the ambient temperature of these trials. Therefore the ambient temperature for these trials is set to -30°C, the minimum temperature achievable in the test chamber.

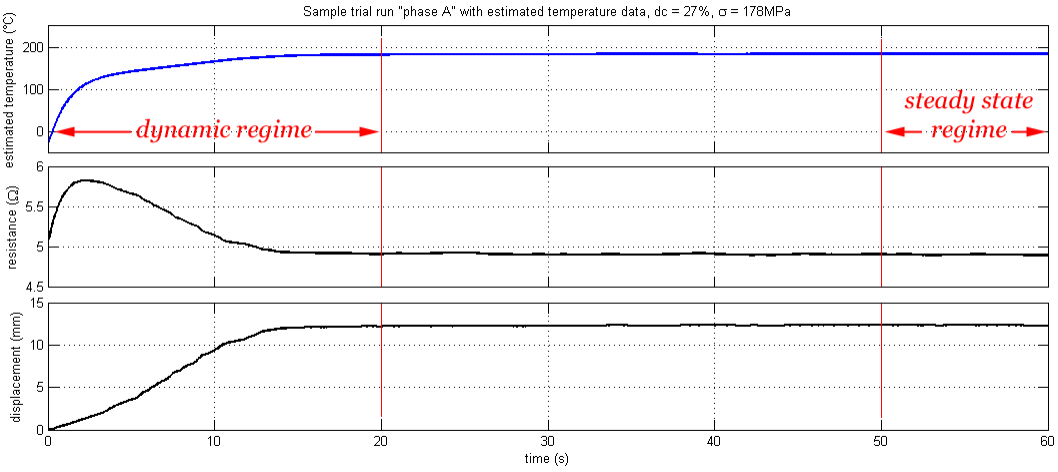

Figure 5.5: The strain, resistance and estimated temperature of the nitinol wire during "phase A" in a single trial run. "dynamic regime" denotes the initial transient region, and "steady state regime" denotes the final 10 seconds of "phase A".

Figure 5.5 shows the estimated wire temperature during a sample trial run. Experimental data shows that for most trials, the steady-state condition in phase A is reached within about 20 seconds. Since the air in the testing chamber is cooled using a fan and heat exchanger combination, fluctuations in the airflow near the SMA wire would likely be present, and therefore, at steady state there are still small variations in the SMAs wire resistance. Thus, the steady-state resistance, wire strain and estimated wire temperature values are taken by averaging the values in the last 10 seconds of "phase A" of each trial, as indicated by *steady-state regime* in Figure 5.5. Figure 5.6 shows the steady-state resistance-temperature $R_{ss}(T)$ and displacement-temperature $d_{ss}(T)$ graphs obtained from a single set of trial runs at a constant stress of 178MPa, overlaid with a smooth spline curve-fit. Note that the curve-fit presented in Figure 5.6 is *not* generated using the model equations listed previously, but is generated to act as a smooth interpolating function to provide higher-resolution $R_{ss}(T)$ data that is used in subsection 5.3.1. Near the end of this section, the fit using the SMA resistance model equations will be presented.

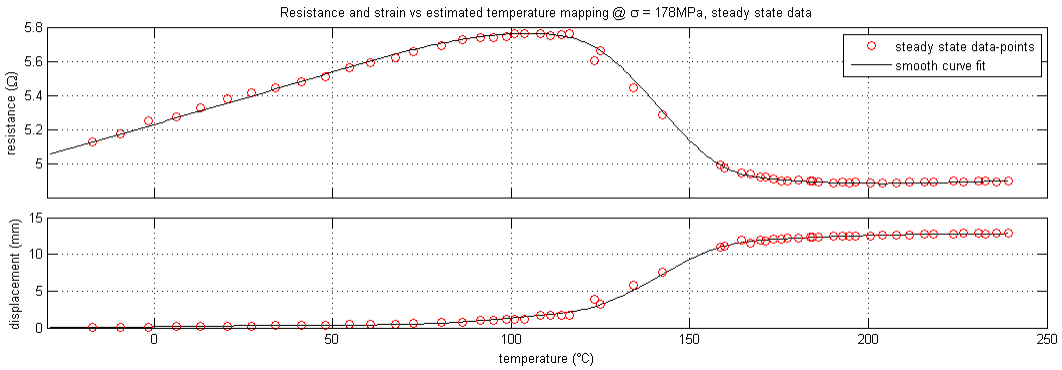

Figure 5.6: The steady-state data points from all trials in the 178MPa trial set are used to generate spline curve fits for the $R_{ss}(T)$ and $d_{ss}(T)$ functions.

5.3.1 Refining the thermodynamic model

As previously mentioned, the wire temperature cannot be measured directly and so must be estimated using (5.9) and (5.10). In the air-cooled experimental setup, the convective heat transfer coefficient h depends on the characteristics of the airflow around the SMA wire, such as the air temperature, velocity, turbulence, etc.

A novel empirical method was devised to compute an accurate h value from the data collected during the experimental trials previously described. The method is based on the idea that the resistance-temperature mapping during the dynamic regime of each trial should be the same as the steady-state resistance mapping computed for entire trial set. The temperature behaviour during the dynamic regime is affected by the time constant of the transfer function (5.11), which can be calculated as $\tau = CV\rho/hA$. Since C, V, ρ and A are all constants, h is the sole factor which affects the time constant. As illustrated in Figure 5.7a, for any given trial, an undervalued h would increase the time constant, hence the estimated wire temperature would take longer to reach its final value than the actual wire temperature would; while an overvalued h means the estimated temperature would reach the final value sooner than the actual wire temperature would. This can be graphically illustrated in Figure

5.7b as a shape distortion of dynamic $R_{sma}(T)$ data collected in any single trial, caused by inaccurate h.

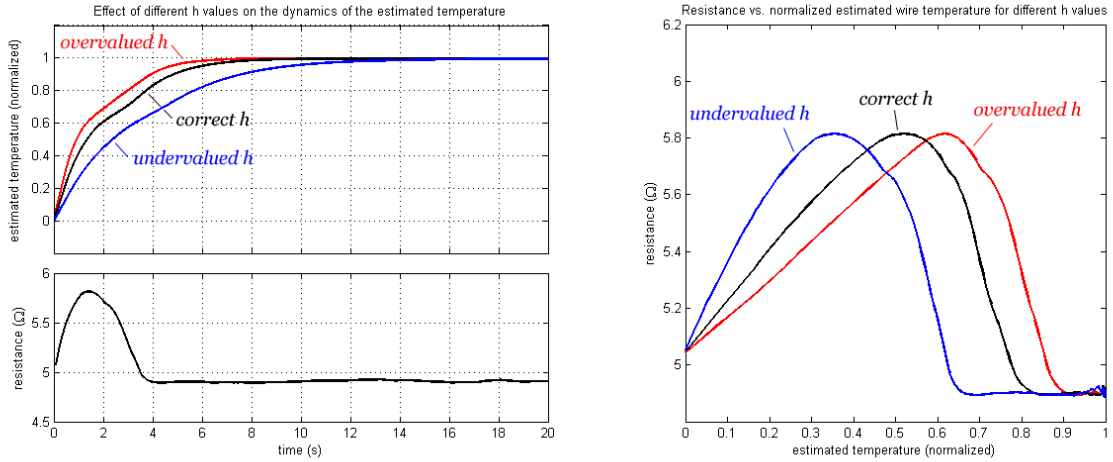

Figure 5.7: (a) R_{sma} and estimated temperature T in the *dynamic regime*. (b) R_{sma} as a function of T. The estimated wire temperature is normalized between its minimum and maximum values to highlight the change in shape of the $R_{sma}(T)$ function when h is changed. dc = 35%, σ=178MPa.

On the other hand, as illustrated in the Figure 5.8, the graph of the steady-state $R_{ss}(T)$ data from each trial set would not suffer a shape distortion as a result of varying h, it would only see a scaling in the estimated T values of all data-points.

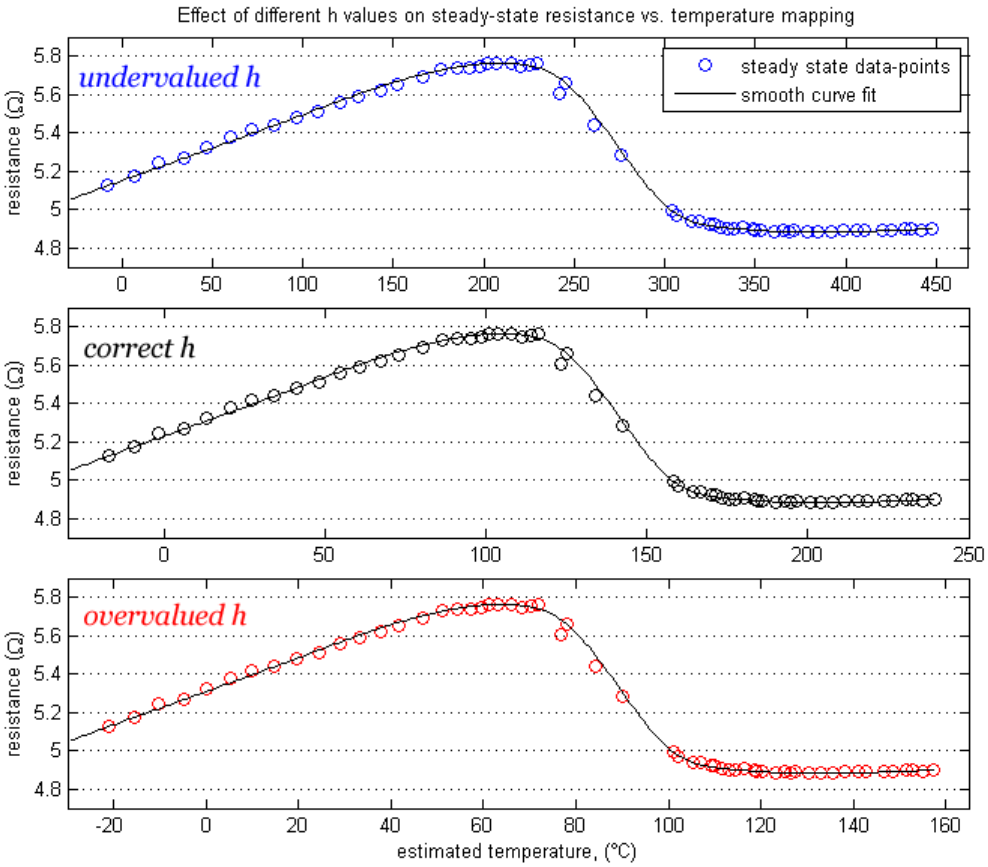

Figure 5.8: Steady-state resistance vs. estimated temperature for different *h* values.

If h is accurate then the *dynamic regime* $R_{sma}(T)$ function from any of the trials in each trial set would match the $R_{ss}(T)$ function of that trial set. In reality, the thermodynamic model equations (5.9) and (5.10) cannot achieve absolute accuracy since two important assumptions were made:

- The convection characteristics near the SMA are assumed to be invariant. In reality, turbulences in the flow and temperature distribution of the air would cause small variations in the convective heat flow from the wire to the surrounding air.

- The value of the parameter C is assumed to be constant, while in reality C would be higher during phase transformation than it would be when the wire is entirely either M-phase or A-phase.

Because of these two assumptions, an appropriate h is calculated by minimizing the error between the dynamic resistance-temperature data and the steady state data during post-processing of the experimental data. Specifically, the following procedure was used to iteratively calculate h using data from each of the four trial sets:

1. Data from one of the four trial sets is used for steps 2 to 8. In steps 2 to 8, the experimental data from each trial in this set is used to generate estimated temperature functions for that trial set, using (5.9) and (5.10). The initial temperature is the ambient temperature of the test chamber during these trials, i.e. -30°C.

2. Two values, h_{high} and h_{low}, are picked as boundary values for the estimate of h used in (5.10). One of these is higher and one of these should be lower than what the "real" h should be. The h values of 70W/(m^2°C) from [8] and 150W/(m^2°C) from [26] are used as initial estimates.

3. The interval between h_{high} and h_{low} is divided evenly into 5 segments by picking 4 other evenly spaced h values (in total, six h values including h_{high} and h_{low} are chosen).

   For each of the six h values:

   4. The steady-state $R_{ss}(T)$ function is generated using the steady-state data from all trials in the set, similar to Figure 5.6. Depending on the choice of h, the T axis would be scaled differently from that of Figure 5.6.

   5. During the *dynamic regime* of each trial (such as shown in Figure 5.5) the estimated temperature $T(t)$ is used to generate a time-series $R_{sim}(t)=R_{ss}(T(t))$. This represents the "simulated resistance" during the dynamic regime using the $R_{ss}(T)$ function. The

(experimental) R_{sma} is compared to R_{sim} total square error (TSE) between the two resistance quantities in *dynamic regime* is calculated. Basically, the TSE indicates the mismatch between $R_{sma}(T)$ and $R_{ss}(T)$ functions for each trial.

6. The TSE values from all trials in the trial set are summed together to calculate a total error e_{total}. e_{total} is a quantitative measure of the total amount of deviation of $R_{sma}(T)$ from $R_{ss}(T)$ for the entire trial set.

7. The six e_{total} values for the six h choices are compared and the two h values with the lowest e_{total} are chosen as new h_{high} and h_{low} for the next iteration.

8. Repeat step 3 – 7 until the difference between successive h_{high} and h_{low} values are small, to arrive at an acceptable h for the trial set

9. Repeat steps 1 – 8 for the other three sets, and calculate the average of all four h values to determine the overall value of h.

Figure 5.9 shows the above procedure for the 178MPa trial set, for three iterations until successive h values differ by less than one. Using this method a final h value of 130.8 W/(m^2°C) was calculated for the 178MPa trial set. For all four trial sets, the h values were determined to be 134 W/(m^2°C), 135.6 W/(m^2°C), 130.8 W/(m^2°C) and 122.5 W/(m^2°C) (from the lowest stress to the highest), resulting in an overall average h of 131 W/(m^2°C) .

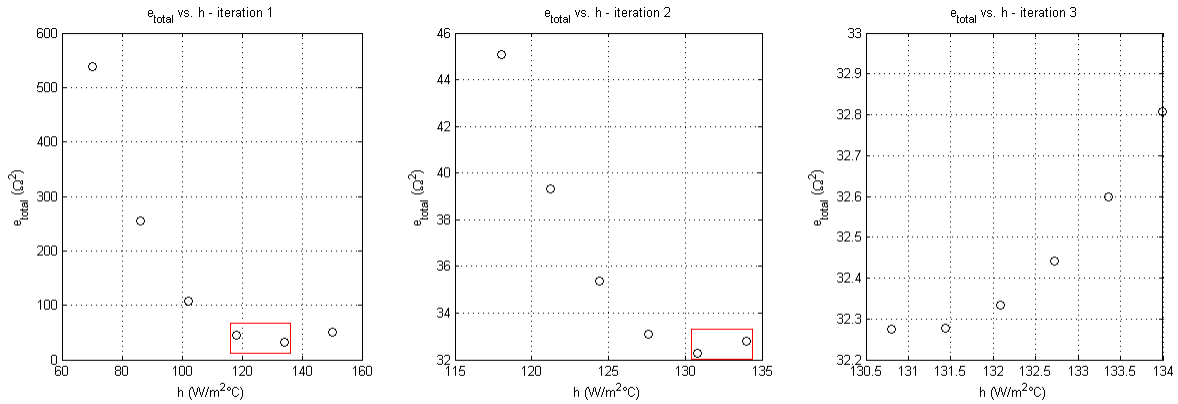

Figure 5.9: Iterative procedure for computing *h*. (a) First iteration. (b) Second iteration. (c) Third iteration.

5.3.2 Procedure for identifying parameters in the phase fraction model

For nitinol SMA actuators, the strain-temperature curve and ξ_M -*T* curves are very similar, so the displacement measurements in combination with the estimated wire temperature data was used for data fitting to identify the parameter in the phase fraction model, Equation (5.12). First, for each of the four trial sets of different wire stresses, the steady state displacement-temperature data points from the end of "phase A" are collected and normalized to values between 0 and 1. Then all four normalised data sets are combined and fitted using (5.12) to calculate the parameters in those equations.

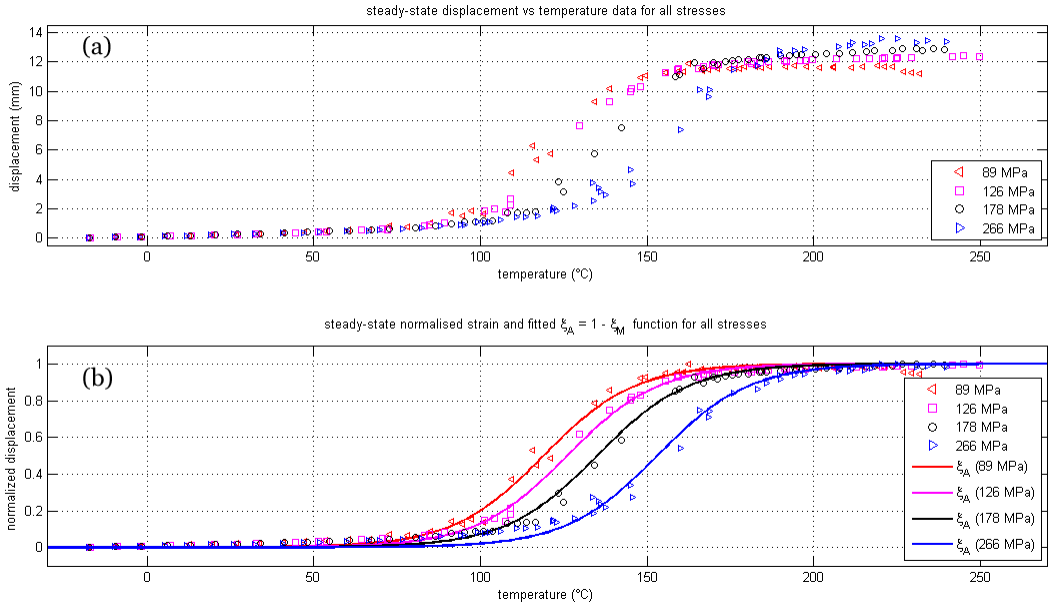

Figure 5.10: Steady-state wire strain: (a) experimental trial data from all four stress sets (b) normalized strain, used for fitting using Equation (5.12).

Figure 5.10 shows the result of the data fitting. As a result of the fitting, the parameters in (5.12) were determined to be:

$$a = 0.07268\ (°C^{-1})$$
$$b = 0.1932\ (\frac{°C}{MPa})$$
$$c = 101.77\ (°C)$$

And the numerical form of (5.12) is:

$$\xi_M = \frac{1}{1 - e^{0.07268(T - 0.1932\sigma - 101.77)}} \tag{5.13}$$

5.4 Resistance model parameter identification

As shown in Figure 5.11a, using the steady-state data obtained from all four sets of experiments, a family of *R*-*T* curves at different stresses is obtained.

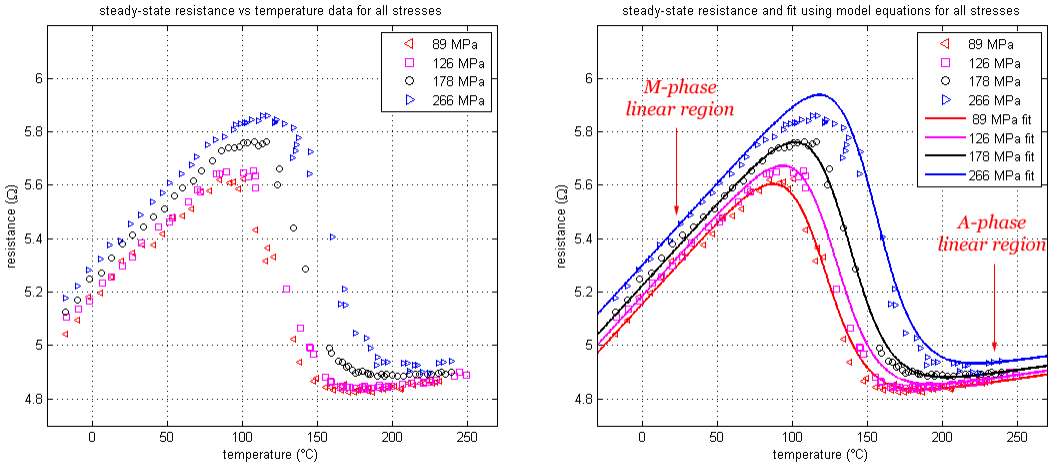

(a) (b)

Figure 5.11: Steady-state R_{sma}-T data (a) from the experimental trials, (b) fitted using the resistance model.

It can be seen qualitatively from Figure 5.11a that the experimental result corroborates with the work of [23] in that 1) resistance change vs. temperature change is approximately linear in both the M- and A- phases; 2) the resistance rate of change $\partial R/\partial T$ in M-phase is larger than in A-phase; 3) a resistance maximum and a minimum are observed between the linear regions; and 4) increasing wire stress causes an overall upshift in the measured resistances as well as the temperatures at which the resistance maximum and minimum occur.

By examining the resistance response in the linear M- and A-phase regions, the parameters in Equations (5.7) and (5.8) can be identified. They are presented in Table 5.5. Using these parameters in combination with the identified phase fraction equation (5.13), the SMA wire resistance is simulated for varying stresses and shown in Figure 5.11b. It can be seen that for most of the stress values, the simulation matches experimental data. Notably, there is a slight mismatch between the simulation and experimental resistance-temperature curves at the 266MPa stress, the cause of this may be due to the discrepancy between the normalized

displacement-temperature function and the subsequently fitted ξ_M -T function for that stress, as shown in Figure 5.10.

Table 5.5: Parameter values for the SMA resistance model

parameter	Value	Parameter	value
R_{0M}	5.08 Ω	R_{0A}	4.82 Ω
T_{0M}	0 °C	T_{0A}	225 °C
$\partial R_M/\partial T$	6.14 mΩ/°C	$\partial R_A/\partial T$	0.802 mΩ/°C
$\partial R_M/\partial \sigma$	0.821mΩ/MPa	$\partial R_A/\partial \sigma$	0.390 mΩ/MPa

We can also see that the temperatures at the resistance maximum and minimum approximately correspond to the temperatures at the start and end of the M→A phase transformation respectively, or the A_s and A_f temperatures. Since for each stress level there is a unique resistance maximum at a unique temperature, knowledge of any one of the resistance, temperature or wire stress values at that maximum would allow the other two quantities to be calculated. In the controller design chapter presented following this chapter, it will be seen that this relationship is exploited in the design of the priming controller.

Chapter 6

Controller design

This chapter presents the design of the controller that was developed in this research. Like [6], the essence of the controller is the concept of priming, i.e. pre-emptively bringing the SMA actuator to the point of onset of actuation. This chapter is organized as follows: in Section 6.1, tangible control system objectives are presented; in Section 6.2 the idea of using resistance feedback to allow the onset of actuation to be detected is presented and in Section 6.3 the design of the priming controller is presented in technical detail.

6.1 Control system objectives

As mentioned in Chapter 2, there are two problems associated which the controller design aims to solve. At the *actuation command time* – defined as the time that the actuation command is given to the SMA actuator system – there is an initial delay prior to the onset of the M→A phase transformation. This delay is the time it takes to heat the SMA up to A_s from T_{amb}, and will be called *actuation delay* in this thesis. While conditions may be present that permit the actuation delay to be small (such as the case when T_{amb} is close to A_s), in general this delay is non-negligible and may be significant enough to be detrimental to time-domain performance of the SMA actuator in its application. If the wire could be pre-heated to A_s and subsequently maintained at that temperature prior to actuation command time, then the subsequent actuation delay can be minimized.

Secondly, the energy taken to increase the SMA wire temperature to A_s, as well as the power required to maintain the wire temperature at A_s, vary with changes in ambient temperature T_{amb} and wire stress σ. It was shown in the SMA resistance model developed in Chapter 5 that changes in σ causes A_s to change, while variations in T_{amb} would naturally cause the temperature difference between A_s and T_{amb} to vary. Both of these factors contribute to the need to adjust the input power P in order to maintain the SMA at A_s under different operating conditions. Insufficient P for the conditions increases the inconsistency in the time taken by the SMA wire to fully contract, and excessive P for the conditions will cause the SMA wires to start contracting prematurely. In practical applications, such premature actuations are to be avoided and a consistent actuation time is highly desirable.

The priming controller presented in this thesis was designed to tackle these two challenges, and it does so by accomplishing two control objectives in two sequential stages, prior to the time of the actuation command:

1. *Preheating stage* – Preheat the wire from its initial temperature to the A_s temperature. The objective of this stage is to allow the wire to be driven to its A_s pre-emptively.

2. *Maintenance stage* – Maintain the wire at A_s until the actuation command time. During this time the controller adjusts P intelligently to compensate for the effects of changing ambient temperature and wire stress.

These objectives are intended to minimize the actuation delay immediately following actuation command time. The overall series of control actions in the controller's preheating and maintenance stages is defined in this thesis as *priming*; and when the SMA is being kept at A_s in the maintenance stage, it is said to be in a *primed state*.

In practical implementations, a complete SMA actuator control system would also include an *actuation stage* following the actuation command, during which time an appropriate actuation strategy is implemented based on the particular performance requirements of the application. For completeness, during the experimental evaluations in this thesis, the

controller includes such an actuation strategy that allows the actuation delay to be examined; however the design of the priming stages is the main focus of this research, as the actuation controller design is application-specific.

6.2 Using resistance as feedback

The motivation for investigating the resistance behaviour of the SMA actuator was presented in Chapter 2, where it was argued that one of the benefits of SMA actuators is that the SMA resistance could serve as a self-sensing feedback mechanism, thereby potentially precluding the need for other sensors that would increase the size and cost of an SMA actuator system. Research work done in the past shows that the resistance of an SMA actuator can indeed be used to indicate the phase composition of an SMA actuator. Note that this is only true given the assumption that the SMA operates only along the major loop of the phase transformation hysteresis, which is the case for SMA toggle actuators. In Chapter 5, the resistance behaviour of an SMA actuator during heating was investigated in detail, and a mathematical model was developed to predict the SMA resistance as a function of temperature and stress. As we will see later in this chapter, an inverse model based on the SMA resistance model developed in Chapter 5 will be incorporated into the priming controller design to allow the stress of the nitinol wire to be recovered.

The unique resistance behaviour of the SMA wire also allows us to determine when the wire starts to actuate during heating. In either of its two stable phases, the resistivity of nitinol, like most other metallic materials, increases with temperature, primarily due to reduced electron mobility. This increase is approximately linear above –200°C [27]. As a result, we observed that the M-phase and A-phase resistances were approximately linear functions of temperature, and were able to model them as such in Chapter 5. A competing effect results from the change in lattice structure from M-phase to A-phase, which results in a decrease in resistance during the M→A transformation. This decreasing effect dominates during transformation; therefore a resistance peak is produced when the SMA wire begins to

actuate, when the rate of resistance decrease from the phase transformation is equal to the rate of increase due to the temperature rise. As a result, the resistance peak temperature, T_{peak}, and A_s are nearly the same for any stress, as shown in Figure 6.1. For the purposes of controller design in this research, T_{peak} can be used as a proxy for A_s.

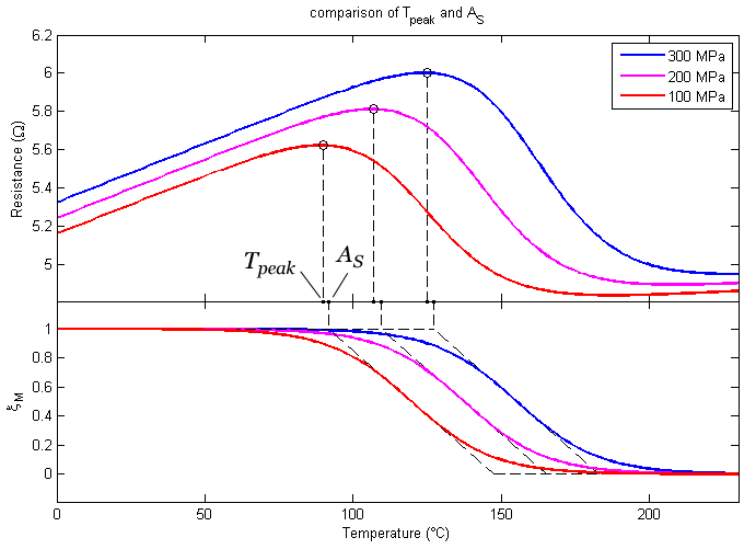

Figure 6.1: Proximity of T_{peak}, and A_s, according to the SMA resistance model developed in Chapter 5.

6.2.1 Relationship of this work with previous controller development in [6]

The idea of using the resistance feedback as part of a priming controller to detect the start of phase transformation was explored previously in [6]. In this section, the aspects of the priming controller designs in [6] are examined.

The controller designs in [6] make use of a probing phase to identify a "threshold" PWM duty cycle value for the heating current that causes the SMA wire to start contracting. In [6], *dc* is gradually raised in 1% increments during the probing phase, each increment lasting one second. Once the wire resistance is detected to be decreasing 60% of the time in any given 1s segment (interpreted as when the resistance peak has been reached and passed), the value of

dc in that segment is identified as the *maintenance duty cycle*, *Mtn_duty*, and the heating current is turned off so that the wire would not be heated further and caused to fully contract. *Mtn_duty* is subsequently used as an indicator of the input power required to cause the wire to start contracting but not fully contract, i.e. to reach a temperature slightly higher but still close to A_s.

While using resistance decrease to detect the resistance peak is an effective method, the use of *Mtn_duty* determined by ramping the duty cycle in 1%/s increments proves problematic for two reasons. First, heating the SMA using any *dc* value for 1s would not cause the SMA to achieve a steady state temperature, as it was shown experimentally in Chapter 5 that the SMA wire in the experimental setup usually takes between 10s to 20s to reach steady state. Therefore, the *Mtn_duty* value determined using probing in [6] would cause the SMA wire to reach a steady-state temperature much higher than the A_s.

Secondly, *Mtn_duty* does not always correspond to the value of *P* that is sufficient to drive the SMA to A_s. The average input power over one PWM cycle can be calculated as

$$P = \frac{{V_S}^2}{R_{SMA}} * dc\%$$

which shows that *P* is also dependant on V_s and R_{sma}. Therefore, a change in V_s would result in a change in *P* even if *dc* is held constant. Furthermore, it was shown that the SMA resistance is constantly changing during heating and, especially in the phase transformation region, the decreasing resistance has a positive feedback effect that causes an increase in the *P*. For these two reasons *dc* should not be used as the sole indicator of the power used to heat the wire.

The controller designs in [6] addressed these issues by using *Mtn_duty* as an intermediate quantity for determining the duty cycle value *priming_duty* that would adequately prime the SMA wire. Three priming controller designs were presented in [6], two open-loop and a third, closed-loop. In the first open-loop design, *priming_duty* is set to half of *Mtn_duty*; in

the second open-loop design a *priming_duty* = *Mtn_duty* -4.5% is used; and in the closed-loop controller design the heating duty cycle is initially ramped to 80% of *Mtn_duty* then a resistance peak detection algorithm is used in combination with a bang-bang controller to allow the wire temperature to servo around the temperature at the resistance peak (in this design there is no steady state "*priming_duty*", rather priming is achieved using alternating high and low *dc* values).

These priming control strategies were tested under constant T_{amb} (-30°C, -15°C, 0°C , 20°C, 40°C) and σ (178MPa) conditions, along with no-priming actuation tests at those conditions. The effectiveness of the control strategies was measured using an equivalent metric to the actuation delay mentioned previously. The priming controllers all show varying degrees of success compared to no-priming, with the *priming_duty* = *Mtn_duty* -4.5% controller showing the most improvement in the actuation delay over no-priming actuation.

There are two additional concerns that were not addressed in [6]. First, *Mtn_duty*, used by all control strategies in [6], is identified experimentally via a probing segment prior to any priming action being performed. The probing phase implemented in [6] may take more than ten seconds to complete and during that time the SMA wire was also caused to partially contract. The probing duration and wire contraction aspects of the probing phase may not be feasible in practical applications.

Secondly, the controller designs in [6] assume that T_{amb} and σ remain invariant between the probing and priming controller phases. Under this assumption, the controllers are able to use the *Mtn_duty* determined in the probing phase to calculate *priming_duty* and actuation duty cycle used later on in the priming and actuation phases. In practical applications, the invariance of T_{amb} and σ are not guaranteed, and as mentioned in 6.1, these changes must be compensated for in a control system which drives the SMA to the cusp of actuation in advance to actuation.

In this research, the notion of detecting the resistance peak is still applied in the design of the priming controller. However, instead of using the resistance feedback to identify a "threshold" *dc* value such as *Mtn_duty* in [6] that is associated with the onset of actuation, it is used to estimate the wire temperature directly, which allows the temperature at the resistance peak – i.e. T_{peak} – to be identified. The appropriate *dc* value can then be calculated based on the identified T_{peak}.

6.3 Design

The controller is based on the idea that since contraction of the SMA wire is achieved through an increase in the wire temperature, the wire temperature should be the quantity to be controlled. Thus, in order to prime the wire, the input to the SMA plant (i.e. *dc*) should be generated in a way that causes the SMA wire temperature to first increase to T_{peak}, then track a temperature setpoint, T_{peak}.

Figure 6.2a illustrates the overall design of the feedback control system, while Figure 6.2b shows the exploded structure of the physical plant being controlled. The priming controller design can then be broken up into these two hierarchical systems, an *inner system* and an *outer system*, as shown in Figure 6.2a:

- *Inner system*: In this closed-loop system, the plant is the thermodynamic model of the SMA actuator system. The output of the plant is the estimated SMA temperature, $\tilde{T}$ and the input to the SMA plant is the input power *P*. Closed-loop feedback control is used to drive the plant output value to the reference value generated by the outer system. The overall output of the inner closed-loop system is *dc* and $\tilde{T}$. Essentially, the purpose of the inner system is to allow the SMA temperature to be estimated and thusly controlled.

- *Outer system*: The outer system generates a reference temperature, T_{ref}, as the input to the inner system. In the controller's maintenance stage, T_{ref} should be ideally equal to T_{peak} and since T_{peak} is dependent on σ, the outer system must find a way to detect changes in σ

accurately and update T_{peak} accordingly in real-time, which it does using $\tilde{T}$ generated from the inner system and R_{sma}. In the preheating stage, an appropriate T_{ref} signal is generated so that the wire is pre-heated up to T_{peak}.

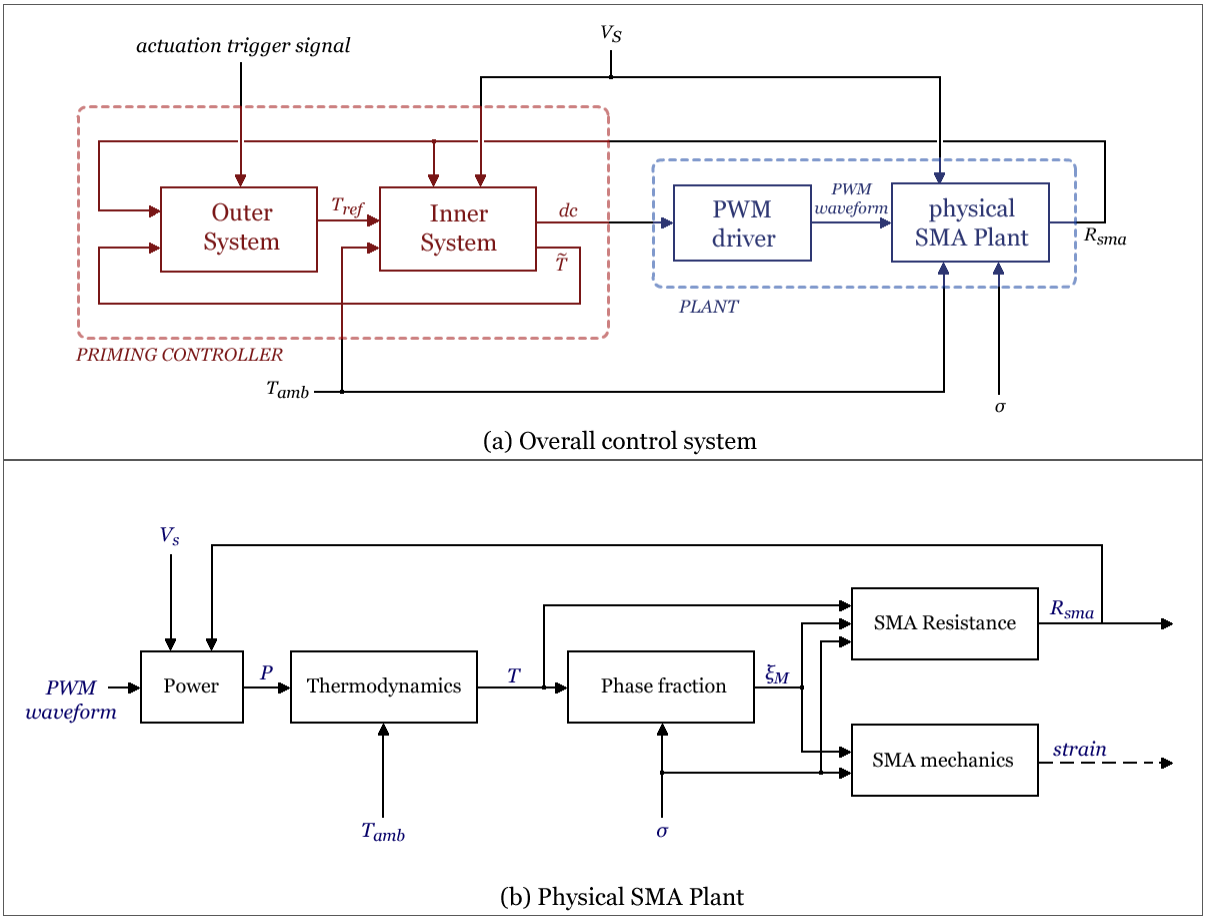

Figure 6.2: The overall control system block diagram. (a) The control system diagram showing exploded views of the controller and plant. (b) A more detailed view of the physical SMA actuator plant.

6.3.1 Design of the inner system

Simply put, the purpose of the inner system is to allow feedback control on the SMA wire's temperature to be implemented. The inner system is constructed based on the standard controller-plant negative feedback system similar to the one shown in Figure 6.3.

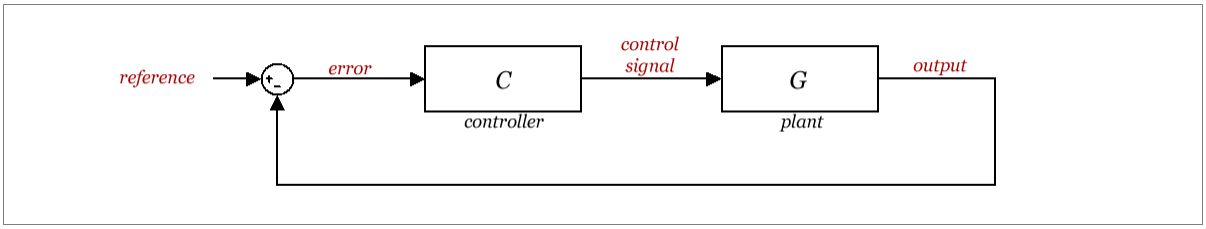

Figure 6.3: The basic negative feedback controller-plant system on which the inner system design is based.

The plant *G* in Figure 6.3 is the thermodynamic model of the SMA wire which allows the temperature of the wire to be estimated during on-line operation:

$$CV\rho\frac{d\tilde{T}}{dt} = P(t) - hA(\tilde{T}(t) - T_{amb}(t)) \tag{6.1}$$

where $\tilde{T}$ is the estimated wire temperature, T_{amb} the ambient temperature, P the input power, and equation parameters taken from Table 5.3. Here, we assume that, since air movement can quickly transport the convective heat loss away from the SMA actuator site, T_{amb} is not affected by the temperature changes of the SMA wire.

We can define $\tilde{\theta} = \tilde{T} - T_{amb}$, thus (6.1) becomes:

$$CV\rho\frac{d\tilde{\theta}}{dt} = P(t) - hA(\tilde{\theta}(t)) \tag{6.2}$$

and the following transfer function is derived[2]:

$$\tilde{\Theta}(s) = \frac{\frac{1}{CV\rho}}{s + \frac{hA}{CV\rho}} P(s) \tag{6.3}$$

Note that in many applications, such as automotive, the change in ambient temperature is very slow compared to the change in the SMA temperature. We can therefore use a first-order approximation to determine the approximate wire temperature based on measured T_{amb} and the dynamics $\dot{\tilde{\theta}}$, and assume $\dot{T}_{amb} \approx 0$.

Since (6.1) is a first order linear transfer function model with input *P*, a linear controller can be used for generating the control signal *P*. Once *P* is known, the corresponding *dc* can be calculated simply using the known quantities V_s and R_{sma} and the following equation derived from (5.10):

$$dc(P, V_s, R_{sma}) = \frac{R_{sma}(t)}{V_S(t)^2} \cdot P(t) \tag{6.4}$$

Figure 6.4 illustrates the exploded structure of the inner system. The inputs are T_{ref}, V_s, R_{sma} and T_{amb}, and the outputs are *dc* and $\tilde{T}$. Intermediate signals are e_θ, *P*, θ_{ref} and $\tilde{\theta}$.

Note that Equations (6.2) and (6.3) are the same as Equations (5.9) and (5.11) in Chapter 5, except that ΔT is replaced with $\tilde{\theta}$. This is to indicate that here the thermodynamic model is used for real-time wire temperature prediction instead of calculating the wire temperature using past data.

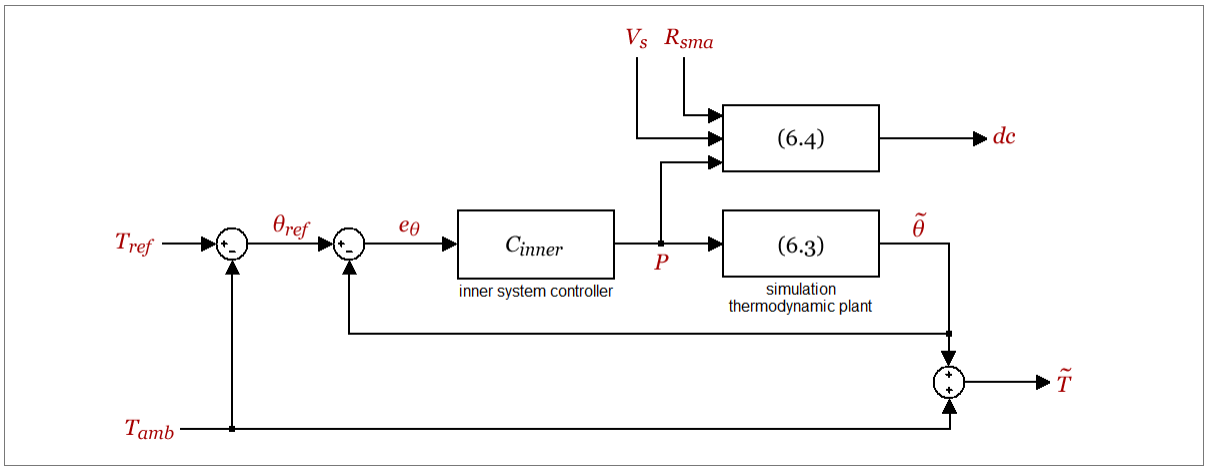

Figure 6.4: Detailed construction of the inner system.

A PI controller, called C_{inner} as shown in Equation (6.5), is implemented to control the temperature estimation plant, modelled by Equation (6.3). With this controller, perfect tracking of step θ_{ref} is achieved, overshoot is avoided, and the tracking speed can be adjusted via a tunable parameter.

$$C_{inner} = (hA + K_e)\left(1 + \frac{hA}{CV\rho} \cdot \frac{1}{s}\right) \tag{6.5}$$

Figure 6.5 shows the detailed structure of the inner system with C_{inner} in place.

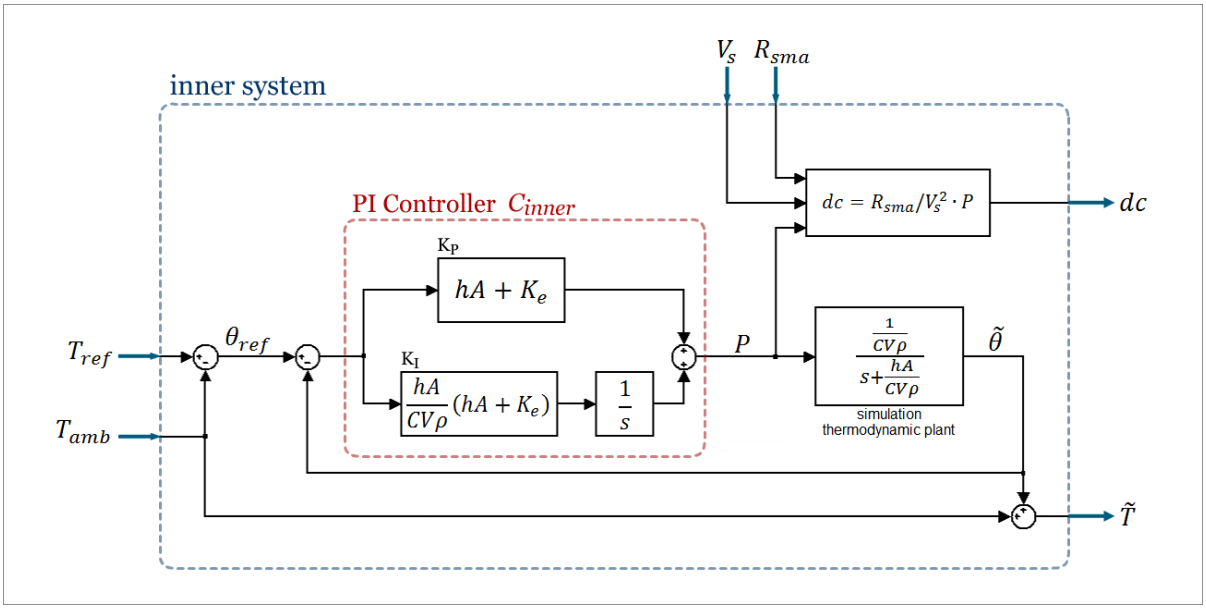

Figure 6.5: inner system, showing the controller C_{inner} and the simulated SMA temperature plant.

The closed-loop transfer function from Θ_{ref} to $\widetilde{\Theta}$ is:

$$\frac{\widetilde{\Theta}(s)}{\Theta_{ref}(s)} = \frac{\frac{1}{CV\rho}(hA + K_e)}{s + \frac{1}{CV\rho}(hA + K_e)}.$$

The closed-loop transfer function can be shown to have a steady-state gain of 1 for a step θ_{ref} signal, i.e. perfect step tracking. The parameter K_e in Equation (6.5) allows the transient performance to be adjusted. The step and ramp response for various K_e values are graphically shown in Figure 6.6, and are summarized in Table 6.1.

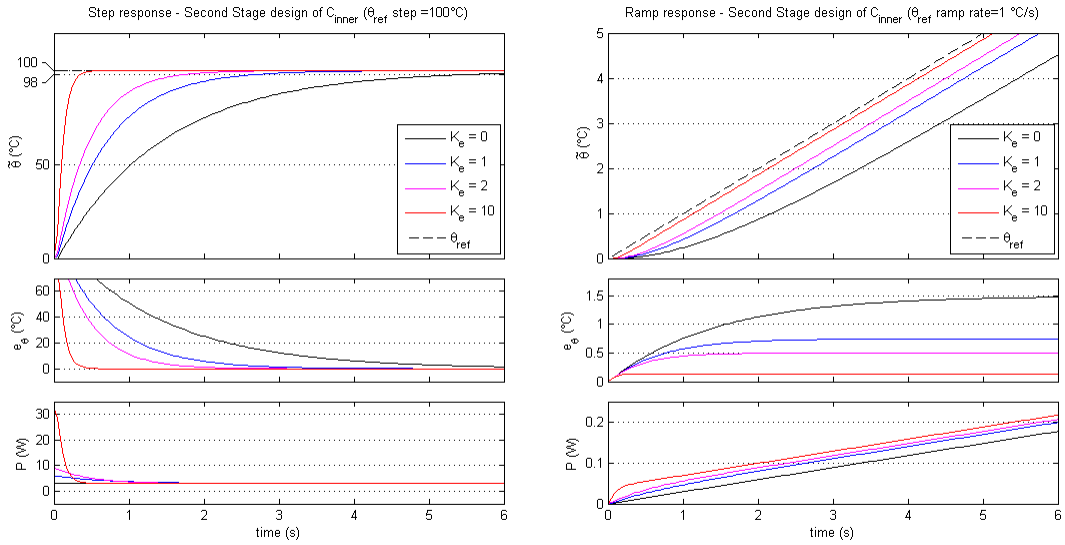

(a) (b)

Figure 6.6: Time-domain response of the second stage design of C_{inner} for various K_e values. (a) Step response. (b) Ramp response for a θ_{ref} ramp rate of 1°C/s.

Table 6.1: 2% settling time (for step tracking) and steady state error (for ramp tracking) for various K_e values.

θ_{ref} type	Step (100°C)	Ramp 0.5°C/s	Ramp 1°C/s	Ramp 2°C/s	Ramp 10°C/s
Performance spec.	2% settling time	e_{ss} steady state error			
K_e=0	5.6s	0.75 °C	1.5 °C	2.99 °C	14.9 °C
K_e=1	2.72s	0.37 °C	0.75 °C	1.49 °C	7.5 °C
K_e=2	1.76s	0.25 °C	0.5 °C	1.0 °C	5.0 °C
K_e=10	0.35s	0.07 °C	0.14 °C	0.27 °C	1.36 °C

The choice of K_e value is based on constraints in the outer system design. We can also see from Figure 6.6a that higher K_e values allow the transient performance to be better, but also causes more power to be drawn momentarily when tracking a step reference signal resulting in an initial power spike, therefore both the choice of K_e as well as the design of the outer system which generates the reference signal for the inner system needs to take the maximum

available power of the system into account. As will be seen in Section 6.3.2, to avoid the initial power spike behaviour, the reference signal is designed to only use ramp and holds, instead of steps. A K_e = 8 was deemed to be an adequate choice, where the 2% settling time for step tracking is 0.47s and a ramp tracking e_{ss} = 0.17°C for a ramp reference slope of 1°C/s. The process of determining this K_e value will be presented in the outer system design section (Section 6.3.2).

6.3.2 Design of the outer system

The goal of the outer system is to generate an appropriate temperature setpoint T_{ref} for the SMA wire. The overall algorithm of the outer system can be divided into three portions, one of each of preheating, maintenance and actuation stages of the overall control system. The preheating and maintenance stages together are called the "priming stages" of the controller, while the actuation stage is activated when the actuation command is received, at actuation command time.

6.3.2.1 Preheating stage

The goal of the preheating stage control algorithm (henceforth called "*preheating algorithm*") is to cause the SMA wire to be heated up to T_{peak}. Because the goal of the overall priming controller is to minimize the actuation delay which occurs after the actuation command time, the exact method or the rate of heating during preheating stage is relatively unimportant, and the design of the preheating algorithm can be tailored to the application constraints.

In this research, the preheating algorithm works by using a linear ramp as T_{ref} signal for the inner system to track and then passing the resultant *dc* signal to the physical system. If the ramp rate is set too low, the time taken for preheating will be long and may not be practical. In addition, the controller uses a resistance peak detector to determine when the SMA has reached T_{peak}, so with a low T_{ref} ramp rate, the effects of thermodynamic disturbances near

the SMA wire and noises in voltage measurements would be more pronounced in the resistance feedback and may cause false peaks to be detected. To experimentally determine the minimum ramp rate at which the effect of the noise in the voltage measurement becomes negligible, the ramp rate was gradually raised, starting from 5°C/s, in 5°C/s increments. At low T_{ref} ramp rates false peaks would cause an incorrect T_{peak} to be determined. However, at a high enough "threshold" T_{ref} ramp rate, the true resistance peak would be detected which allows the correct T_{peak} to be determined. When the ramp rate is increased further, the determined T_{peak} would still remain correct since the detected resistance peaks would still be true peaks. The minimum T_{peak} ramp rate can then be determined as the "threshold" ramp rate for which higher ramp rates produce the same T_{peak} value at the instant the resistance peak is detected. Using this method, a minimum ramp rate of 30°C/s was determined that ensures no false peaks are detected. Note that this value is specific to the experimental setup used in this research. For other applications, differences in the electrical and environmental conditions might cause a higher amount of noise in the voltage measurements and more disturbances in the thermodynamic characteristics of the SMA actuator, and would warrant a new minimum T_{ref} ramp rate to be determined.

While there is some flexibility in the method and rate of preheating, the preheating time should still be short since it should be complete before the actuation signal arrives and the timing of this is unknown. However, high preheating rates reduce the accuracy of quantities determined at the resistance peak. Because the controller is a sampled data system with a fixed sampling time, a preheating rate that is too high reduces the precision of T_{peak} determined at peak time. This would cause the determined T_{peak} value to be higher than that real T_{peak} value.

Through experimental testing, the slope of T_{ref} ramp in the preheating algorithm was selected to be 80°C/s, which allows the SMA wire temperature to be increased from -30°C to 130°C in about two seconds. Note that -30°C represented the minimum ambient temperature

that could be set in the testing chamber and 130°C represents the upper limit of T_{peak} for all the stresses tested in Chapter 5.

The SMA wire is assumed to be at T_{amb} at the beginning of the preheating stage, so the outer system sets the initial value of T_{ref} to T_{amb} during preheating.

T_{peak} Detection and Transition to Maintenance stage

The ramping of T_{ref} is halted to prevent actuation when the resistance peak is detected. The peak detector computes the difference between the current and previous samples in the R_{sma} feedback, and generates a trigger event "*trg.R*" when that difference is non-positive to indicate that the peak has been detected, i.e.:

$$(R_{sma}[k] - R_{sma}[k-1] \leq 0) \Rightarrow trg.R$$

trg.R is the cue for switching from the preheating to maintenance stage. $\tilde{T}$ and R_{sma} data from one sample prior to *trg.R* are used to identify T_{peak} and σ at the beginning of the maintenance stage, which will be explained in detail in Subsection 6.3.2.3.

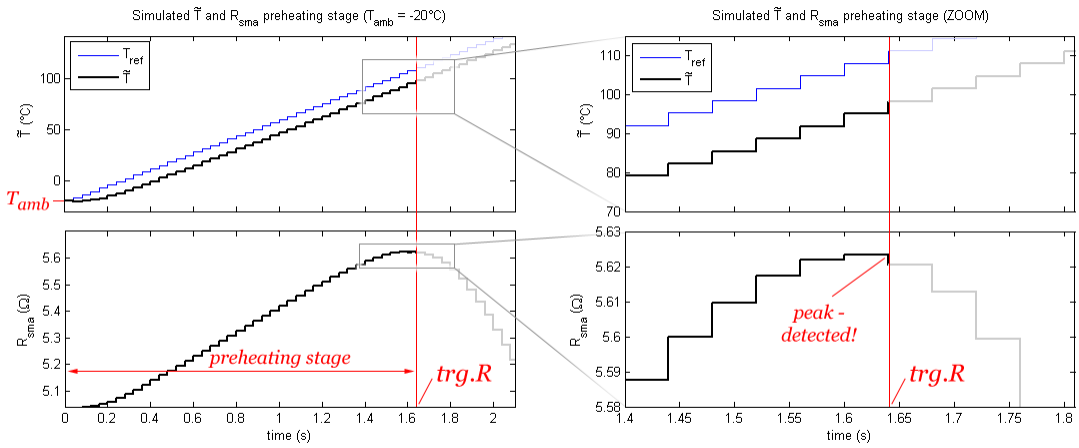

Figure 6.7: Preheating state algorithm and generation of *trg.R* event.

The preheating algorithm is graphically illustrated in Figure 6.7.

6.3.2.2 Maintenance stage

As stated earlier, one objective for the priming controller is that it must be able to adjust the input power in a way that keeps the SMA at T_{peak} in the presence of changing stress and ambient temperature. Changes in T_{amb} can be compensated effectively with the availability of T_{amb} measurement and the closed loop design of the inner system, so the outer system would only need to have a way to compensate for σ changes in the maintenance stage (henceforth called the *maintenance algorithm*).

It was shown in the SMA resistance model developed in Chapter 5 that given different σ values, the *R*-*T* function follows different curves. As a result both T_{peak} and the peak resistance value R_{peak} are different for different stresses. Figure 6.8 shows the family of *R*-*T* functions for a range of different σ values. Using the T_{peak}, R_{peak}, and σ data from the resistance model as shown in Figure 6.8, the following linear curve fit functions can be identified to map σ to T_{peak} and R_{peak}.

$$T_{peak} = f(\sigma), \tag{6.6}$$

$$R_{peak} = g(\sigma). \tag{6.7}$$

Since these are linear functions, they are also invertible. We can then also define a mapping between T_{peak} and R_{peak}, i.e.

$$T_{peak} = q(R_{peak}) = f\left(g^{-1}(R_{peak})\right). \tag{6.8}$$

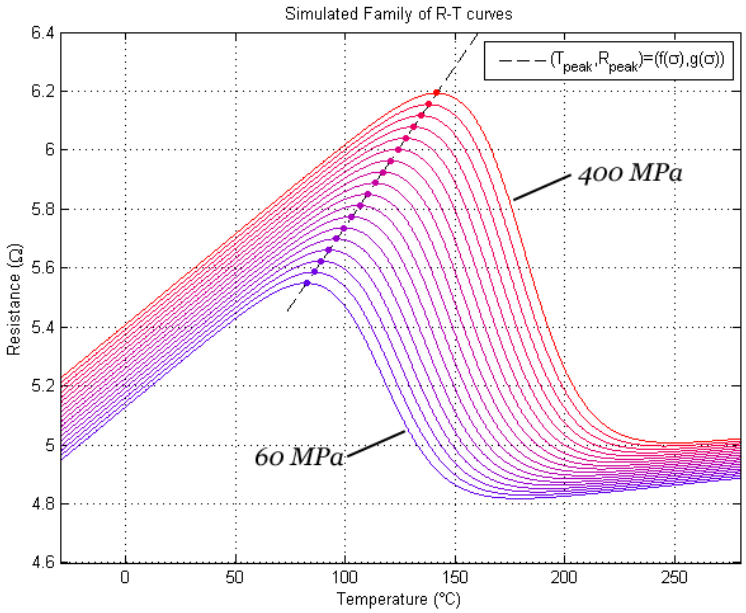

Figure 6.8: A family of *R*-*T* curves for various stresses, generated using the SMA resistance model developed in Chapter 5.

When the resistance peak is reached and T_{peak} is determined at the end of the preheating phase, the stress can be inferred from the family of curves in Figure 6.8. During the maintenance stage, however, a peak in R_{sma} cannot be detected since it is expected that R_{sma} would be *staying at* its peak, so another method must be used to find T_{peak}.

Inverse SMA resistance model

It can be observed from Figure 6.8 that changing stress causes a proportional change in resistance, at all temperatures. Another way to look at this is that at any given temperature, the isothermal resistance to stress mapping is one-to-one. Therefore, at any time in maintenance stage, R_{sma} and the wire temperature estimation $\tilde{T}$ can be used to pinpoint the *R*-*T* curve the SMA is currently on from the family of *R*-*T* curves, allowing σ to be determined. Mathematically, this is expressed as the following *inverse model* equation:

$$\sigma(t) = \Psi\big(\tilde{T}(t), R_{sma}(t)\big). \tag{6.9}$$

where Ψ is the inverse SMA resistance model to compute σ. Once σ is known, T_{peak} can be calculated simply by $T_{peak}(t) = f(\sigma(t))$ according to Equation (6.7) and the outer system can subsequently update the T_{ref} signal to match T_{peak}.

Figure 6.9 illustrates this process graphically for a sample σ change from 200MPa to 100MPa during the maintenance stage.

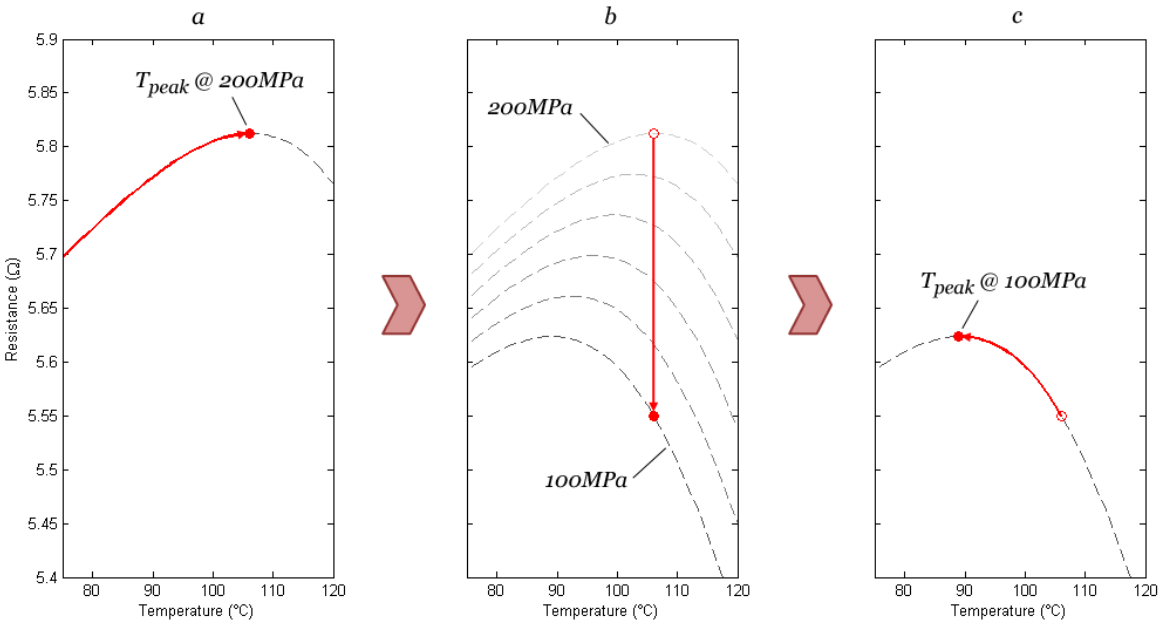

Figure 6.9: Illustration of the maintenance stage algorithm. (a) The SMA wire, initially at 200MPa stress, is preheated to T_{peak}. (b) The stress suddenly changes from 200MPa to 100MPa, causing the *R-T* function to change. (c) T_{peak} is updated based on this new stress.

It can be observed from Figure 6.9 that a sudden change in stress causes $\tilde{T}$, maintained at the previous T_{peak}, to deviate momentarily from the new T_{peak}. This is because while T_{ref} can be updated immediately when the stress change is detected, $\tilde{T}$ cannot follow T_{ref}

instantaneously. This would be a problem in the case of a negative stress change, as T_{peak} is shifted to a lower value resulting in the wire temperature being briefly higher than T_{peak}, which in turn would cause the wire to begin unintended actuation. Since T_{peak} was defined earlier to be the temperature where actuation starts, $\tilde{T}$ should not exceed T_{peak} to avoid actuation during the maintenance stage.

Since in any practical application, it would take at least some time for the wire stress to transition continuously from one value to another, a realistic assumption is that the stress change cannot be instantaneous and the rate of stress change is upper bounded. In the evaluation experiments, the stress change is tested by gradually adding or removing a 2lb weight (equivalent to a σ change of 176MPa) to the load of the SMA actuator in an approximately one second period, so $d\sigma/dt$ = 176MPa/s is the most extreme stress change for which countermeasures are designed.

A two-part countermeasure is devised to prevent unwanted actuation. The first part is to design the inner system controller to have a fast response time. This can be achieved by setting the error gain K_e to a high value. The second part is to set T_{ref} at a slightly lower temperature than A_s, so even if a stress change causes A_s to decrease rapidly, the slightly lower T_{ref} combined with the fast response time of the inner system would prevent $\tilde{T}$ to from exceeding A_s. Mathematically, this can be expressed as:

$$T_{ref}(t) = T_{peak}(t) - T_{buffer}. \tag{6.10}$$

where T_{buffer} is an acceptable "buffer" temperature. It's clear that the larger T_{buffer} is, the lower the wire temperature would be from T_{peak} during the maintenance stage, and the longer the actuation delay would be. Thus, the choice of T_{buffer} represents a design trade-off between robustness to sudden decreases in stress, and actuation delay.

For the controller design here, T_{buffer} is set to 5°C. Using this T_{buffer} value, K_e can be set so $\tilde{T}$ does not exceed A_s for a stress change of -175MPa/s. Through iterations, K_e = 8 was

determined to be sufficient. Figure 6.10 illustrates the simulated time-domain behaviour of T_{peak}, T_{ref} and $\tilde{T}$ using this countermeasure method. The maximum stress change condition is simulated as a σ change from 100MPa to 275MPa at 10–11s, and 275MPa to 100MPa at 15–16s. Figure 6.11 shows the same simulation, but with resistance information shown.

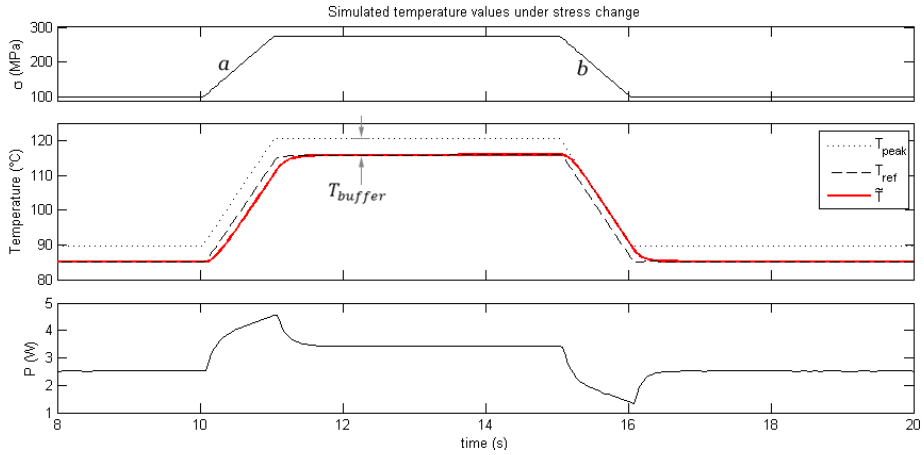

Figure 6.10: Simulated time-domain behaviour of the controller during the maintenance stage.

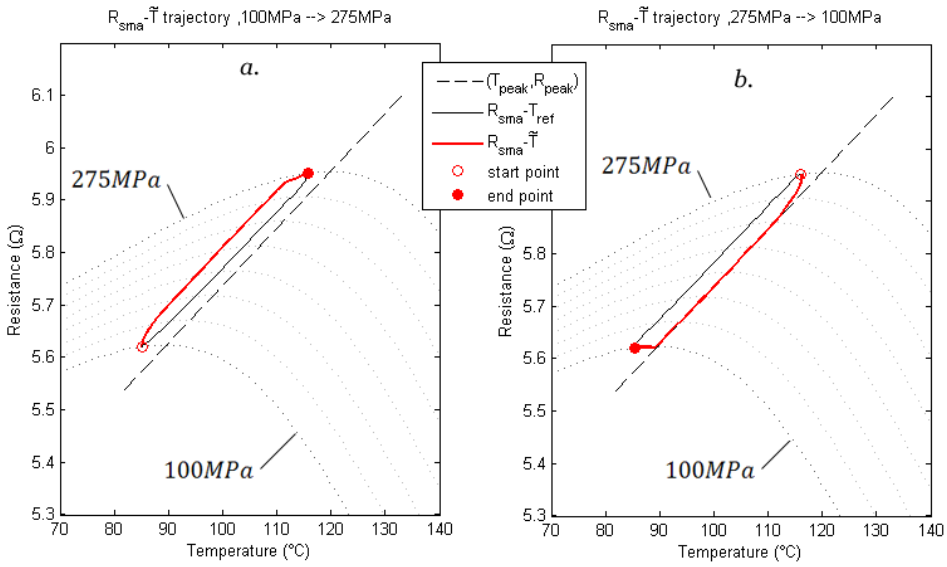

Figure 6.11: Simulated *R-T* behaviour of the SMA actuator during the maintenance stage (a) during a stress increase from 100MPa to 275MPa, and (b) during a stress decrease from 275MPa to 100MPa.

There is also a trade-off between T_{buffer} and K_e, as a larger K_e value makes the inner system respond faster, which would allow a smaller T_{buffer} to be set. At the same time, a higher peak power consumption is required for a higher K_e value, which may be a limiting factor in application. In this system, the maximum power available may be estimated using nominal source voltage Vs=10.5V and nominal SMA resistance Rsma=5.5Ω:

$$P_{max} = (10.5V)^2/5.5\Omega \approx 20W.$$

Figure 6.10 shows that the simulated power consumption is far from the above maximum power.

In Simulink, the determination of σ from $\tilde{T}$ and R_{sma} (i.e. Equation (6.9)) is implemented as a 2-dimensional lookup table. The Ψ data-points in the lookup table have T and R resolutions of 1°C and 0.01Ω respectively, and σ resulting from any intermediate T and R inputs is calculated via linear interpolation.

The $T_{peak} = f(\sigma)$ function is implemented as a one dimensional lookup table. Since it was observed that $f(\sigma)$ is a linear function, it was also appropriate to use linear interpolation with this lookup table.

6.3.2.3 Identifying A_s and wire stress at the start of maintenance stage

The *trg.R* event is an indication that the SMA has just reached T_{peak} and the controller should transition from the preheating stage to the maintenance stage. At *trg.R* time, the controller must determine the initial σ value for the maintenance stage, which we may call σ_0. Recall that at one sample prior to *trg.R*, $(\tilde{T}, R_{sma})$ is equal to (T_{peak}, R_{peak}), so if $k_{trg.R}$ represents the *trg.R* sample in time and assuming that σ has not changed since one sample prior to $k_{trg.R}$, then two possible σ_0 can be determined, as either

$$\sigma_{0,a} = f^{-1}\big(\tilde{T}[k_{trg.R} - 1]\big), \tag{6.11}$$

derived from (6.6), or

$$\sigma_{0,b} = g^{-1}\big(R_{sma}[k_{trg.R} - 1]\big). \tag{6.12}$$

derived from (6.7). Since T_{peak} is computed according to (6.6) during the maintenance phase, two possible initial T_{peak} values may be determined as a result of the two possible σ_0 values, ie.

$$T_{peak0,a} = f\left(f^{-1}\big(\tilde{T}[k_{trg.R} - 1]\big)\right) = \tilde{T}\big[k_{trg.R} - 1\big], \tag{6.13}$$

or

$$T_{peak0,b} = f\left(g^{-1}\big(R_{sma}[k_{trg.R} - 1]\big)\right). \tag{6.14}$$

where $T_{peak0,a}$ and $T_{peak0,b}$ are the two possible initial T_{peak} values in maintenance stage. In simple terms, Equation (6.13) says that the initial T_{peak} is the estimated wire temperature at *trg.R* time; while Equation (6.14) says that the initial T_{peak} is found using the inverse resistance model. In theory, both $T_{peak0,a}$ and $T_{peak0,b}$ should be identical and in simulation it

was shown that the two values were nearly the same[3]. However there are two reasons why (6.14) should not be used to calculate the initial T_{peak} value.

First, SMA wires are subject to fatigue as a result of repeated actuation cycles. The nominal length of the wire would change over the life of the actuator, altering its resistance behaviour. The manufacturer's data sheet for the Flexinol SMA wire notes that even though the mechanical characteristics of Flexinol wires are stable compared to similar alloys, around 1% permanent strain will develop after 100,000 cycles during operation, even at a very most stress of 138MPa [11]. Experimentally, it was found that between the time that the SMA model was developed and experimental testing of the priming controller, the nominal wire length had permanently changed from 28.3cm to 29cm.

Secondly, the resistance model and its inverse model are only accurate for the SMA actuator used in the lab at the time that the SMA resistance model was developed. For other actuators where the SMA wire length or diameter is different, modifications to the model and inverse model are needed.

Based on these two reasons, (6.13) is used for determining the initial T_{peak} value, T_{peak0}, i.e.

$$T_{peak0} = \tilde{T}\left[k_{trg.R} - 1\right]. \tag{6.15}$$

However this would imply that the R_{sma} values during the maintenance stage would be inconsistent with the resistance as predicted by the SMA resistance model, and the maintenance algorithm could not use Equation (6.9) to determine σ accurately during the maintenance stage. The two reasons mentioned above for using (6.13) have to do with a change in the wire dimensions, which has a linear scaling effect on the measured resistance of the SMA wire. For example, if the wire has become 1.1 times longer, it would have R_{sma} values that are 1.1 times more than the values predicted using the SMA resistance model, at

[3] Because all signals are sample-based, the peak R_{sma} sample may not be the true R_{peak} and $\tilde{T}$ may not be the true T_{peak}. This causes a very small difference between $T_{peak0,a}$ and $T_{peak0,b}$ in simulation.

all temperature and stresses. Thus, to be able to use Equation (6.9) which is based on the SMA resistance model, the predicted resistance values of the forward resistance model could be multiplied by the scaling factor, i.e. we "scale" the resistance model to match with the resistance characteristics of the physical SMA wire. Equivalently, R_{sma} may be multiplied by the inverse of this factor to use with the un-modified inverse resistance model. Mathematically this process can be formulated as:

$$R_{peak,old} = q^{-1}(T_{peak}), \tag{6.16}$$

$$c_{scaling} = \frac{R_{sma,peak}}{R_{peak,old}}. \tag{6.17}$$

In the formulas above, $R_{peak,old}$ is the predicted peak resistance based on T_{peak}, $R_{sma,peak}$ is the actual R_{sma} peak value, and $c_{scaling}$ is the scaling factor determined by the ratio between the measured and predicted peak values. The subscript "old" indicates the idea that under the assumption that the wire's resistance behaviour had changed, $R_{peak,old}$ is what would have been the resistance had the resistance behaviour not changed. Once $c_{scaling}$ is determined at *trg.R* time, its inverse is used to generate scaled versions of R_{sma} during maintenance stage:

$$R_{old}(t) = R_{sma}(t) \cdot c_{scaling}^{-1}. \tag{6.18}$$

Once R_{old} is computed, it is used in place of R_{sma} in (6.9) for dynamically identifying σ during the maintenance stage. The inverse SMA resistance model can be updated as:

$$\sigma(t) = \Psi\big(\tilde{T}(t), R_{old}(t)\big) = \Psi\big(\tilde{T}(t),\ R_{sma}(t) \cdot c_{scaling}^{-1}\big). \tag{6.19}$$

Note that the inner system also uses R_{sma} to calculate the duty cycle of the PWM driver, and in that use the un-modified R_{sma} is used.

Assuming that the same brand of Flexinol® SMA wires are used for SMA actuators of different dimensions, using the $c_{scaling}$ turning parameter allows the existing inverse SMA resistance model to be used instead of needing to re-model the SMA actuator.

6.3.3 Actuation stage

The actuation stage controller design (called the *actuation algorithm* from hereon) is responsible for actuating the nitinol wire, i.e. causing wire contraction by heating the wire. The objective of the *priming stages* was to ensure that the SMA wire is close to T_{peak} (specifically, T_{peak} - T_{buffer}) at the beginning of the actuation stage. The transition from the maintenance stage to the actuation state is triggered when the actuation command is received at actuation command time.

Like the preheating algorithm, the actuation algorithm may be independently designed to meet performance specifications in specific applications. Nonetheless, for experimental evaluation of the priming controller design, an actuation algorithm is included in the priming controller design. During the actuation stage, T_{ref} is ramped at a slope of 60°C/s starting from its last value (i.e. the T_{ref} value at actuation command time, which we may call $T_{ref,act}$) until it has reached a temperature that is 100°C+T_{buffer} above $T_{ref,act}$. $T_{ref,act}$ is in fact equal to T_{peak} - T_{buffer} at actuation command time, and it was observed in the SMA resistance model that heating the wire to 100°C above T_{peak} ensures the wire is fully actuated. The 60°C/s ramp rate is used for fast actuation to be achieved, but not so fast that the initial acceleration due to rapid wire contraction causes over-stress on the SMA wire which would have a detrimental impact on the cycle life of the SMA actuator.

In practice, the actuation strategy implemented will depend on the application. Since the principle interest in this thesis is the priming controller, we do not focus on actuation strategy design. As long as the actuation strategy used is consistent in all experimental trials, the priming controller's performance may still be evaluated.

Chapter 7

Experimental results and discussion

In this chapter, the experimental results of the evaluation of the priming controller's performance are discussed. In addition, the design and experimental evaluation of an actuation strategy where priming was not implemented are also presented, as a benchmark for assessing the benefits of priming. These experiments were performed to measure the performance of the priming controller using the criteria outlined in Chapter 3, namely the quality, repeatability and consistency of priming.

This chapter is organized as follows: in Section 7.1 the design of an SMA actuator controller without priming is presented, where the actuation stage strategy is identical to that of the priming controller. However, there are no preheating and maintenance stages. In Section 7.2 the test procedure for the experiments is presented. Section 7.3 describes in detail the different operating conditions in which the priming controller and No-priming Controller are tested. Section 7.4 defines the metrics with which the performance of the priming controller is measured. In Section 7.5 the experimental data is presented and discussed. Finally in Section 7.6, conclusions are made from the experimental results with respect to the three criteria for judging the controller's performance.

7.1 Design of the No-priming Controller

To show that the priming controller design (called the *Priming Controller* in this chapter) improves the response time of SMA actuators and to quantify that improvement, a *No-priming Controller* is also designed and tested to provide a benchmark for comparison. The No-priming Controller uses a controller design based on the same design as the Priming Controller, in that the controller design consists of an outer system for generating a T_{ref} signal and an inner system that allows an appropriate *dc* signal to be generated. The difference between the No-priming Controller and the Priming Controller is that the preheating and maintenance stages are not implemented in the No-priming Controller, and the controller directly goes to the actuation stage upon system activation. Without a maintenance stage, the No-priming Controller does not need to dynamically adjust *dc* to compensate for σ changes, so an inverse SMA resistance model is also not implemented as part of the No-priming Controller.

The actuation algorithm of the No-priming Controller is largely similar to that of the Priming Controller. To heat the SMA, a 60°C/s ramp T_{ref} signal is generated by the outer system and an appropriate *dc* value is generated and sent to the PWM driver. To avoid ramping T_{ref} overheating the SMA actuator, a ceiling temperature is determined in a similar way to the priming controller. In the Priming Controller design, the T_{ref} ceiling temperature during actuation is set to 100°C above the last determined T_{peak} during the maintenance stage. In the No-priming Controller, the $\tilde{T}$ value at the first time that an R_{sma} peak is detected used as T_{peak}, which allows the ceiling temperature to be determined as T_{peak}+100°C. Note that in the No-priming Controller, the determination of T_{peak} does not rely on an inverse SMA resistance model, and is solely used for calculating the temperature ceiling during actuation. The time-domain plot of a No-priming Controller trial run is presented in Figure 7.3.

7.2 Experimental procedure

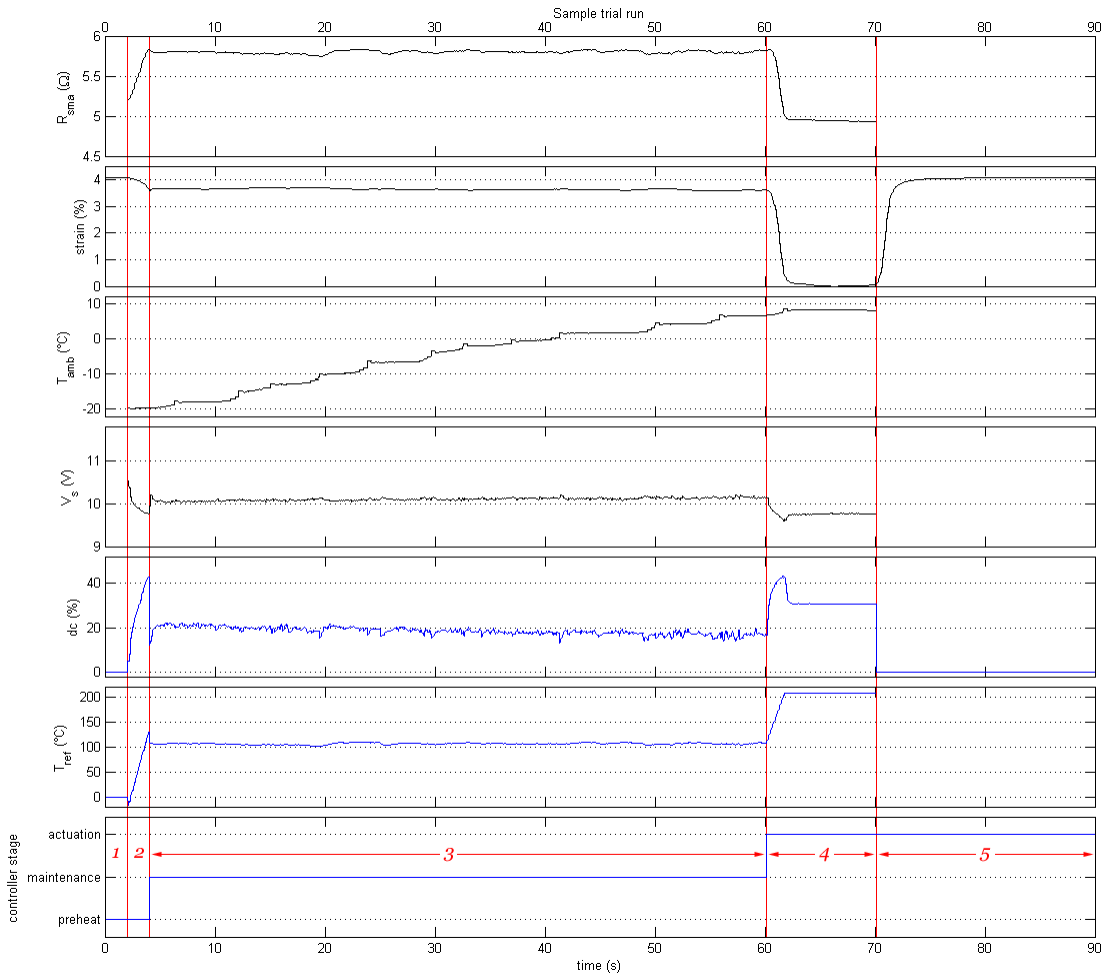

Figure 7.1: Segments for Priming Controller test trials. 1. Buffer segment. 2. Preheating segment. 3. Maintenance segment. 4. Actuation segment. 5. Cool-down segment.

As illustrated in Figure 7.1, each experimental trial for Priming Controller testing can be divided into the following 5 sequential segments.

1. *Buffer*: The first two seconds of the trial is an inactive "buffer" period. This is done because it was discovered that the MultiQ interface board may experience glitchy "freezes" during the first second of each trial which causes an incorrect PWM signal to be sent to

the driver circuit and also incorrect data to be received. This "freeze" behaviour never happens after the first second so all experimental actions will take place after two seconds (an extra second was added to the initial buffer period as an extra "buffer"). Another effect possibly caused by these "freeze events" is that the data stream from the MultiQ interface board seems to be slightly delayed when they are imported into Simulink.

2. *Preheating*: This segment, which starts at 2s, is where the SMA is heated using the preheating algorithm of the controller. The heating phase is ended once a peak in the resistance feedback is detected. The transition from the preheating segment to the subsequent maintenance segment is triggered automatically by the Priming Controller.

3. *Maintenance*: in this segment, the controller subsystem generates a duty cycle value according to the maintenance algorithm described in Subsection 6.3.2.2 to attempt to maintain the wire at its primed state. This segment starts whenever the pre-heating phase ends, and ends when the actuation command occurs, at actuation command time.

   In some trials, the ambient temperature T_{amb} and wire stress σ were deliberately varied during this time, according to the test condition for those trials.

4. *Actuation*: this is the segment where the SMA wire is commanded to actuate using the actuation method of the control algorithm. The actuation command time is at 60 seconds, and this segment lasts for 10 seconds.

5. *Cool-down*: The last segment is the cool-down segment which starts from the end of the actuation phase and lasts for 20 seconds. During this phase, current to the SMA is turn off by setting the duty cycle to zero to allow the wire to cool to the ambient temperature so it will be ready for the next trial.

Figure 7.1 shows the wire strain as a positive value at the beginning of the trial run, and a strain of 0% when the wire is fully actuated. To compute the strain, the steady-state displacement of the wire in the actuation segment as measured by the encoder is used as the

zero-strain value as shown in Figure 7.2, and the difference between the displacement value at all other times and the zero-strain is divided by the nominal wire length of 28.3cm to arrive at a percentage strain value. Since the wire is longer in martensite, the martensite strain is a positive value compared to the austensite strain.

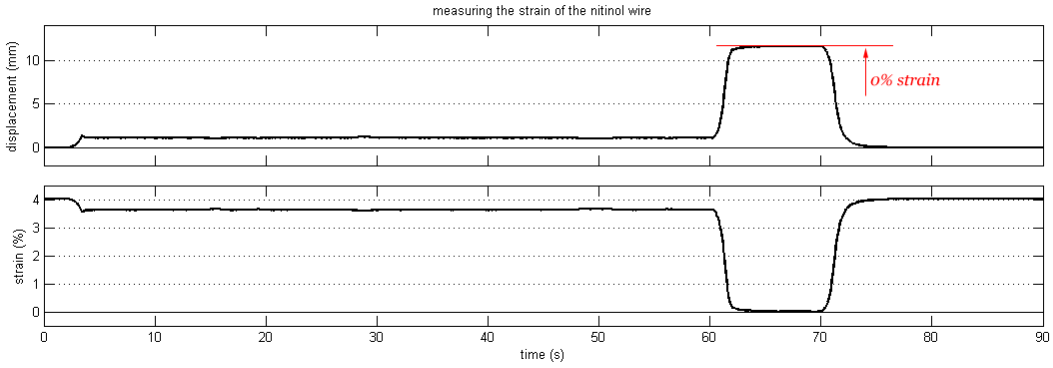

Figure 7.2: Determination of the wire strain (where the actuated wire has zero strain) from the displacement measurement.

In Figure 7.1, it can be seen that for trials that experience a changing T_{amb} during the maintenance segment, the T_{amb} feedback signal has an unusual "staircase" appearance even though in reality the ambient temperature would be expected to change in a gradual and smooth fashion. Investigations into this behaviour reveals that this behaviour is not caused by the complexity of the software system, nor do parameters such as the fundamental frequency of the software or the PWM frequency have any effect. Furthermore, the "stairs" does not seem to be associated with any quantified T_{amb} or time values, as T_{amb} changes in a range smaller than depicted in Figure 7.1 also exhibit this behaviour but on a smaller scale. Therefore, it is concluded to be an artefact of either the thermocouple that measures the ambient temperature or the NEWPORT® thermocouple signal conditioner. Unfortunately there is no way to deal with this sensor error in the experimental trials, and, as shown later, may hinder the performance of the Priming Controller during the experimental evaluation. Note that when T_{amb} is relatively constant, this behaviour is not observed. Also note that in

practical applications, the ambient temperature sensor should be chosen so that the effect of this strange behaviour is minimal.

7.2.1 Experimental procedure for testing the No-priming Controller

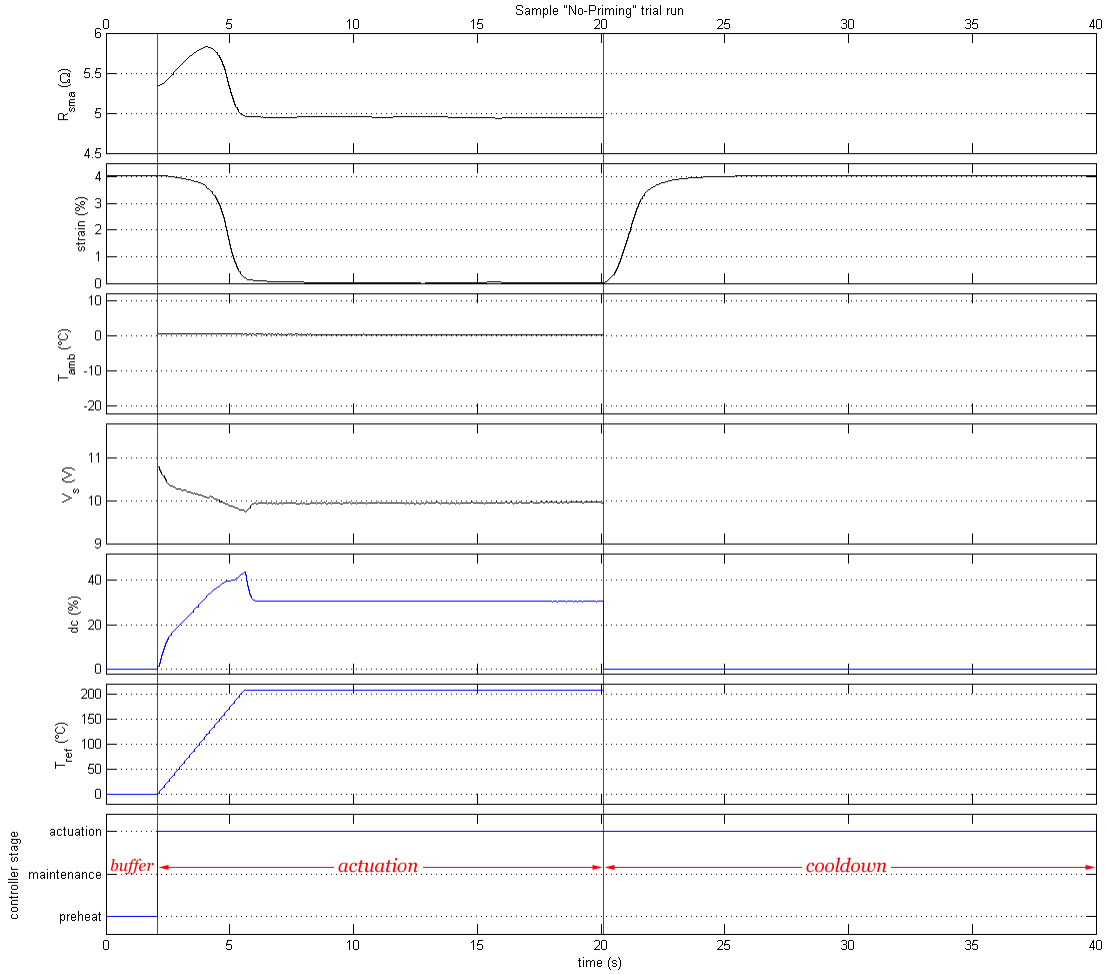

Figure 7.3: Segments for No-priming Controller test trials.

Figure 7.3 illustrates the experimental procedure for testing the No-priming Controller. It is identical to the procedure for testing the Priming Controller, except for the following two changes:

- The preheating and maintenance segments are skipped, since there are no preheating and maintenance stages in the No-priming Controller;
- The actuation command time is immediately after the initial two second buffer period.
- The actuation segment lasts for 20 seconds (the additional time compared to the priming controller test procedure is to allow for the actuation delay), after which is the cool-down segment.

7.3 Test conditions

The performance of the Priming Controller is evaluated in three ambient conditions, as described below.

Test condition A: Constant T_{amb}, constant σ

For this test condition, the experiments are performed at ambient temperatures of -30°C, -15°C, 0°C, 15°C, 30°C and at wire stresses of 101MPa, 189MPa and 277MPa, for a total of 15 different ambient temperature and stress combinations. For each T_{amb} and σ setting, ten trials are identically performed, for a total of 150 trials.

The three stress conditions are created by placing 1 lb, 2 lb or 3 lb weights in the load cage (which itself weights 0.154 lb), while the ambient temperature conditions are set using the OMEGA temperature controller. Note that, as mentioned earlier, a hysteresis of +2.5/-2.5°C exists for these ambient temperature set-points.

Test condition B: Varying T_{amb}, constant σ

For this test condition, the experiments are performed while the ambient temperature is varied during the maintenance segment, while the wire stress is held constant at 101MPa, 189MPa or 277MPa. The ambient temperature is varied by keeping the refrigeration system running with a constant setpoint, while manually opening and closing the fridge

door. When the door is opened, T_{amb} increases and when the door is closed, T_{amb} decreases. From the experimental feedback data of T_{amb} measurements, the range of T_{amb} variations during the trials is from -25°C to 15°C, while the maximum rate of change of T_{amb} is 1.5°C/s.

At each of the three stress settings, ten trials are performed, for a grand total of 30 trials.

Test condition C: Varying T_{amb}, varying σ

In this test condition, both ambient temperature and wire stress vary during the maintenance segment, to test the controller's ability to track the resistance peak under such conditions. Ambient temperature variation is achieved in the same way as test condition B, i.e. by opening and closing the fridge door. An increase in stress is tested by a one-time change of wire stress from 101MPa to 277MPa, achieved by adding a 2lb weight, in a gradual fashion, to the load cage with a 1lb weight in it initially, over a period of approximately one second. Conversely, a decrease in stress is tested by removing 2lb from the load cage initially at 3lb, again in a gradual fashion. The transition between the two stress regimes takes place at an arbitrary time during the maintenance segment. An effort was made to keep the ambient temperature varying during the stress change, but since the fridge door must be open in order to change the stress, experimental data shows that the ambient temperature during that time is increasing or stable for a majority of the trials.

For this test condition, ten trials are performed for a low-to-high stress transition scenario (referred to as "*l2h* scenario") and ten are performed for a high-to-low stress transition scenario ("*h2l* scenario"), for a total of 20 trials.

Since σ can only be changed by manually changing the weight attached to the SMA wire, there is no way to keep T_{amb} constant since the fridge door must be opened to perform that operation. Therefore, the fourth possible test scenario of "Constant T_{amb}, varying σ" cannot be tested.

While the Priming Controller was tested under all of the above conditions, the No-priming Controller could only be evaluated under test condition A. This is because test conditions B and Cs were meant only for testing the Priming Controller*'s* performance under varying ambient conditions, to which the No-priming Controller is not applicable.

7.4 Performance measurement

Recall that the goal of the Priming Controller, as stated in Chapter 6, is to minimize the actuation delay time by a) preheating the SMA actuator up to T_{peak} and b) maintaining the wire as close as possible to, but not exceeding T_{peak} until actuation. Experiments are performed to measure how well the Priming Controller design performs using the criteria described in Chapter 3, namely the quality, repeatability and consistency of priming. Recall that the quality of priming was defined as a measure of the improvement in actuation response time using priming and how well the "primed state" is maintained; the repeatability of priming was defined as a measure of the repeatability of the Priming Controller*'s* performance under the same test conditions; and the consistency of priming was defined as how consistently the Priming Controller performs under different conditions.

Since the main goal of priming is to improve the response speed of SMA actuators, the actuation delay concept from the previous chapter can be used as time-based metric for the performance of the Priming Controller.

Actuation Delay (t_{AD}): as shown in Figure 7.4, t_{AD} is measured as the time between the actuation command time and the time when the resistance peak is first reached during the actuation phase. Qualitatively this metric indicates indirectly the deviation between the SMA wire temperature and T_{peak} at the start of the actuation phase. Since the goal of the controller during the maintenance stage is to maintain the wire as close to T_{peak} as possible, the smaller t_{AD} is, the closer the wire temperature would be to T_{peak}, and the higher the quality of priming is.

By comparing the t_{AD} of the Priming Controller to that of the No-priming Controller, the improvement in actuation response time of the SMA actuator using priming can be quantified. Comparing t_{AD} across trials performed in the same test condition as well as in different test conditions allows the repeatability and consistency criteria to be measured.

Note that two factors related to Priming Controller design also impact the t_{AD}: T_{buffer} and the power used in the actuation stage. A higher input power heats the wire faster, thereby reducing the time between the actuation command and resistance peak time. Since we are trying to use t_{AD} as a measure of how far the wire temperature is from T_{peak} during maintenance, we use the same value of T_{buffer} and the same actuation strategy in all trials, in order to minimize these effects.

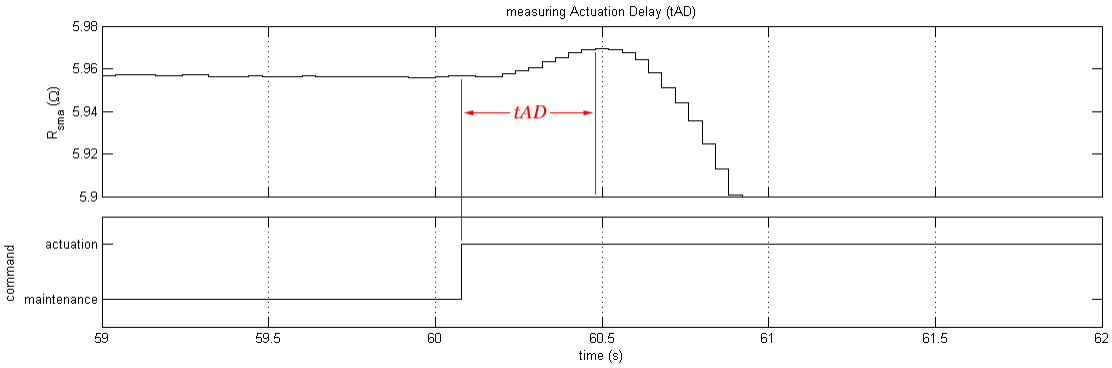

Figure 7.4: Determining the *Actuation Delay*, or t_{AD}.

In addition to t_{AD}, two strain-based metrics – *mean strain* and *strain variation* – are also used to measure performance. These two metrics are calculated based on the wire strain during the maintenance segment of each trial run, so they are only applicable to priming strategy trials (the no-priming strategy trials lacks a maintenance segment).

Mean Strain (SM): illustrated in Figure 7.5, SM is defined as the mean value of the wire strain during the maintenance segment of each trial. One would expect SM to be the same across trials in the same test condition as well as across different test condition, given the stress is the same, since a "primed" SMA actuator should have roughly the same "primed"

strain regardless of ambient temperature. Therefore, SM is a measure of both the repeatability and consistency criteria.

As shown in Figure 7.6, for trials performed in test condition C, the high stress and low stress regimes have noticeably different SM values. This is because of the fact that the nitinol wire has a finite elastic modulus, so different stresses will cause the wire to have different strains, even though during the maintenance segment the priming controller (presumably) keeps the nitinol wire at the same phase state. Therefore, for test condition C trials, two SM values are computed, one for the high stress regime and one for the low stress regime.

Strain Variation (SV): as illustrated in Figure 7.5, SV is defined to be the range of wire strain variations during the maintenance segment. In test conditions A and B, σ is constant, thus T_{peak} should not change during priming and therefore the strain is ideally also constant (i.e. a SV of zero). Undetected ambient temperature or air flow variations near the wire would cause the wire temperature to vary slightly, and would result in a non-zero SV value. A large SV value may also be produced if the controller does not predict T_{peak} accurately during the maintenance segment, causing T_{ref} to be set far off of T_{peak}, which in turn causes the SMA wire to undergo positive or negative length change during the maintenance stage. A low SV value indicates good rejection of ambient temperature variations during the maintenance segment and accurate T_{peak} determination, and is an indicator of a high quality of priming. Comparing SV across trials in the same test condition and different conditions also allow the repeatability and consistency of priming to be measured.

For test condition C trials, two SV values are computed (for the same reason two SM values are computed) for each trial as shown in Figure 7.6, one for the low-stress regime and one for the high-stress regime.

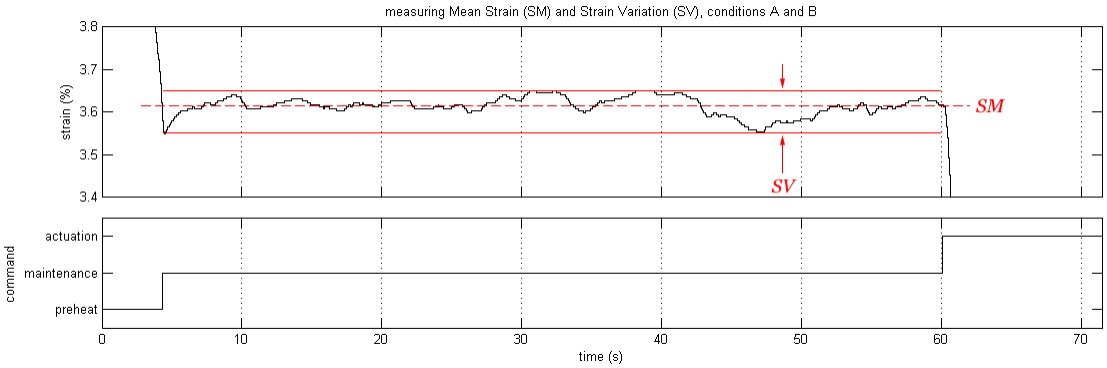

Figure 7.5: Determining the Mean Strain (SM) and Strain Variation (SV) for test condition A and B trials

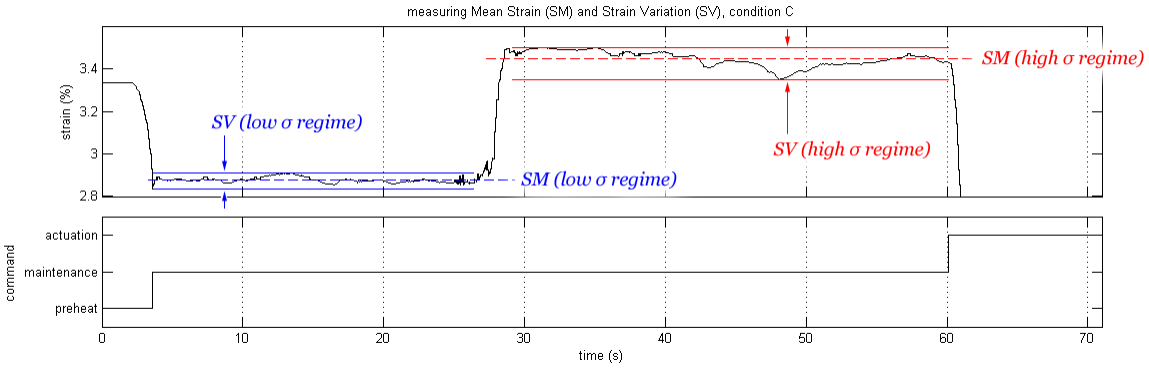

Figure 7.6: Determining SM and SV for the low-stress and high-stress regimes of test condition C trials.

7.5 Results

7.5.1 Measuring performance using t_{AD}

7.5.1.1 No-priming Controller

The test condition A t_{AD} performance of the No-priming Controller is shown in Figure 7.7 – Figure 7.10. In Figure 7.7 – Figure 7.9, the t_{AD} is plotted against $T_{amb,act}$, defined as the T_{amb}

value at actuation command time (i.e. the start of the actuation segment), for each of the three σ conditions. In Figure 7.10, t_{AD} for all nominal ambient temperatures and stresses are all shown together. Note that due to the sampling time of 0.04s of the controller, the values of all t_{AD} data collected are quantized to multiples of 0.04s.

With the No-priming Controller, the wire is not primed in advance to actuation, so it is expected that:

- t_{AD} should decrease with higher $T_{amb,act}$;
- The decreasing t_{AD} vs. $T_{amb,act}$ trend should be linear, since the actuation algorithm relies on a linear T_{ref} ramp; and
- t_{AD} should increase with higher σ, since increasing σ causes T_{peak} to increase.

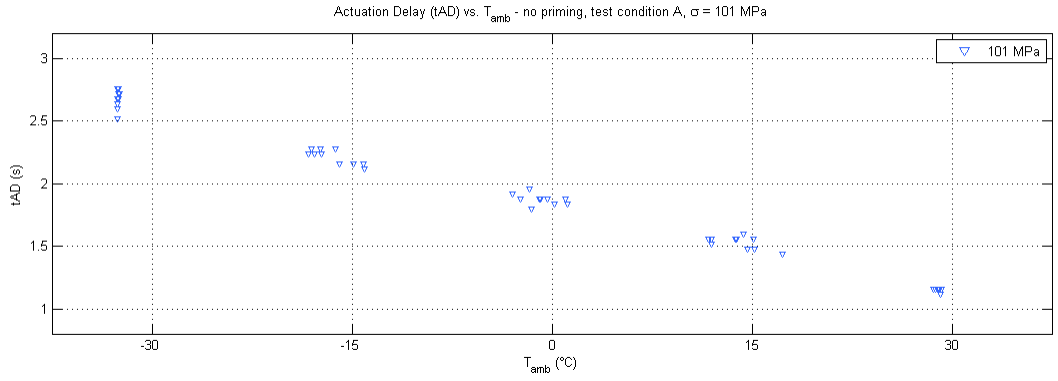

Figure 7.7: t_{AD} data for all No-priming Controller trials at σ = 101MPa.

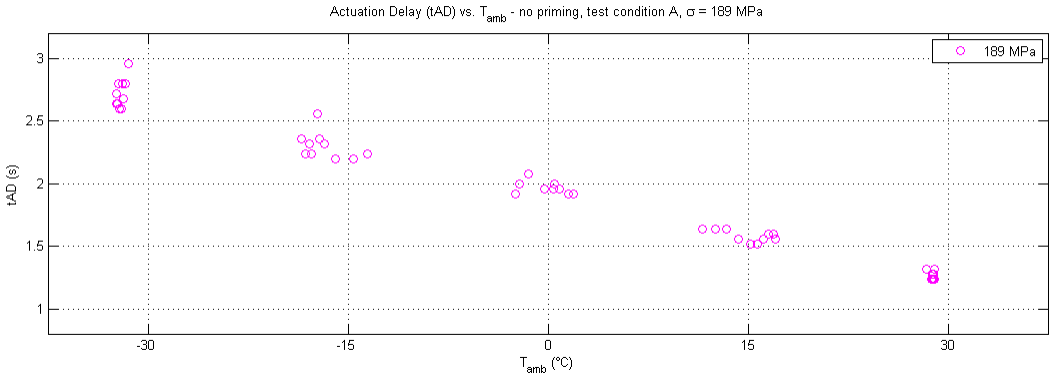

Figure 7.8: t_{AD} data for all No-priming Controller trials at σ = 189MPa.

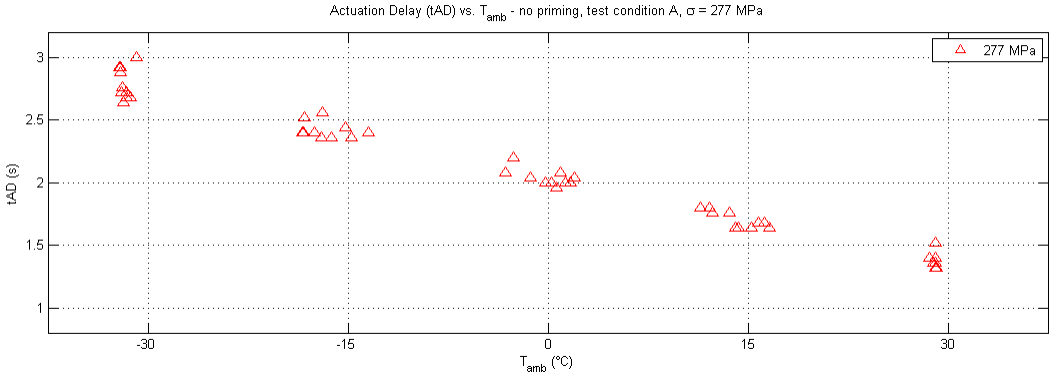

Figure 7.9: t_{AD} data for all No-priming Controller trials at σ = 277MPa.

It can be seen from the Figure 7.7 to Figure 7.9 that there is a spread in $T_{amb,act}$ the value for each nominal T_{amb} setting, due to the ±2.5°C hysteresis band for the OMEGA temperature controller. There is a larger spread for the middle nominal T_{amb} settings than there is for the two extreme T_{amb} settings, and this is because there is almost no hysteresis action exhibited by the temperature controller for those two settings. It was observed that at the two extreme T_{amb} settings, a static equilibrium was established within the ambient temperature hysteresis band in the test chamber such that the bang-bang controller action was not needed to maintain the temperature within the hysteresis band. In Figure 7.10, all data from the Figure 7.7 to Figure 7.9 are presented in the same plot, organized into five "bins" for each of the

five nominal T_{amb} settings. Within each bin, the t_{AD} data for each stress setting is horizontally shifted differently to better illustrate the relationship between the t_{AD} and stress.

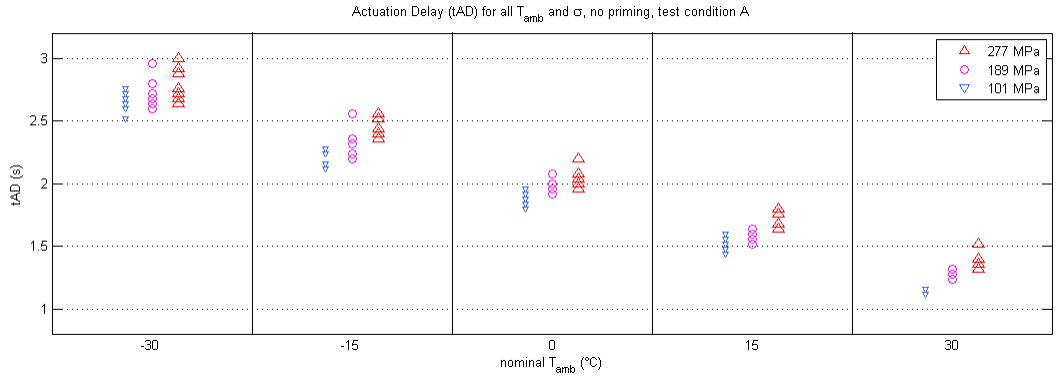

Figure 7.10: t_{AD} data for all No-priming Controller trials at all stresses, plotted against the nominal T_{amb} setting for each trial.

For all T_{amb} and σ settings, the No-priming Controller t_{AD} data for each set of ten trials are statistically summarized in Figure 7.11 using the mean and standard deviation measures.

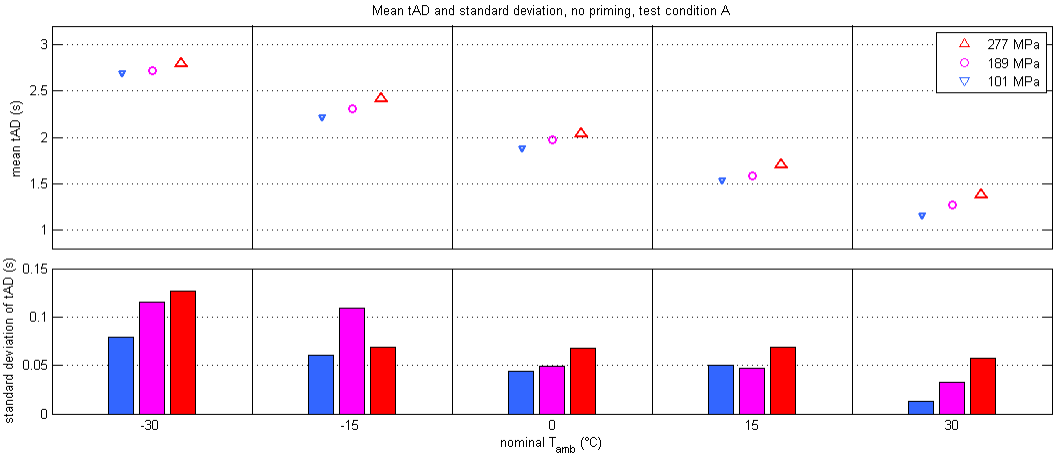

Figure 7.11: Mean and standard deviation of No-priming t_{AD} data at each T_{amb} and σ setting.

It can be seen from Figure 7.11 that without priming, t_{AD} for the SMA actuator is in the range of around 1.1s to 2.8s for the ranges of T_{amb} and σ tested, and there is a definite correlation between t_{AD} and $T_{amb,act}$. The experimental data shown above is consistent with the expected linear decreasing trend between t_{AD} and $T_{amb,act}$.

Furthermore, it is seen that the higher σ also cause t_{AD} to be higher. Once again this is consistent with the prior knowledge that higher stresses cause A_s, which is approximated by T_{peak}, to shift to a higher temperature. The difference in t_{AD} for the three σ values is approximately the same for all five T_{amb} conditions.

It can also be observed that at higher T_{amb} values, there is less variation in t_{AD} for the same T_{amb} and σ condition. The cause is hypothesized to be the fact that at lower ambient temperatures, the SMA is more sensitive to air flow disturbances. A disturbance in the air flow near the SMA wire would cause the convective heat loss from the SMA wire to vary slightly, which may be modelled as a disturbance in h in (5.9). Because T - T_{amb} (where T is the SMA's temperature) is also in the term with h in (5.9), the effects of these convection disturbances is magnified when T - T_{amb} is large, as is the case with a lower T_{amb} value.

Overall, t_{AD} for the No-priming Controller experimental trials exhibit expected trends under different T_{amb} and σ conditions, and there is a small amount of t_{AD} variation for trials performed at the same T_{amb} and σ condition.

7.5.1.2 Test condition A

t_{AD} data for the Priming Controller is presented in Figure 7.12 – Figure 7.16. Figure 7.12 to Figure 7.14 show t_{AD} data against $T_{amb,act}$ for each of the three stresses tested, Figure 7.15 combines t_{AD} data for all nominal T_{amb} and σ settings on the same plot, and finally Figure 7.16 presents the mean and standard deviation of t_{AD} for each of the set of 10 trials performed at the same T_{amb} and σ setting.

The Priming Controller design ideally keeps the nitinol wire temperature at T_{peak}-T_{buffer} prior to actuation (T_{buffer} being 5°C in the controller design), so experimentally it is expected that:

- t_{AD} should stay at the same value regardless of $T_{amb,act}$.
- t_{AD} should stay at the same value regardless of σ.
- t_{AD} increase linearly with higher T_{buffer} settings. Unfortunately only one T_{buffer} setting (T_{buffer} = 5°C) was tested, so this hypothesis cannot be tested.

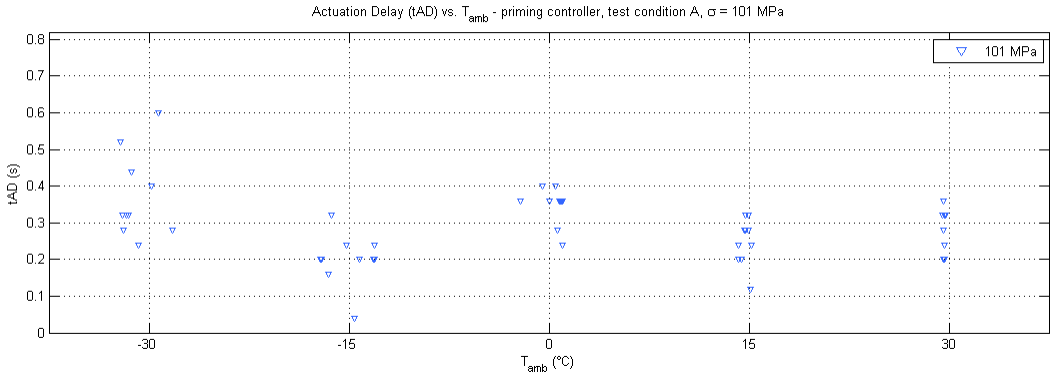

Figure 7.12: t_{AD} data for all test condition A (Priming Controller) trials at σ = 101MPa.

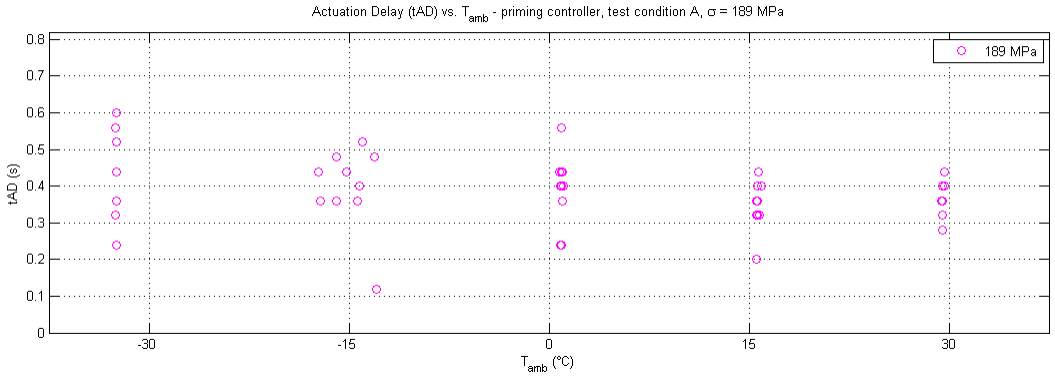

Figure 7.13: t_{AD} data for all test condition A trials at σ = 189MPa.

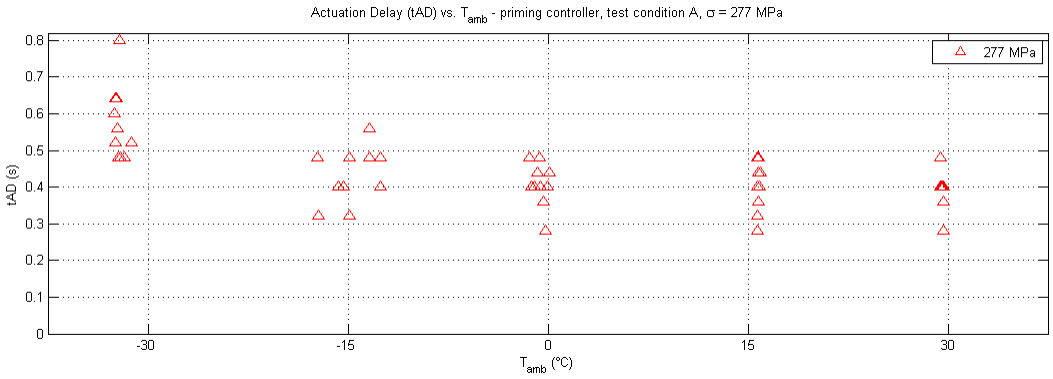

Figure 7.14: t_{AD} data for all test condition A trials at σ = 277MPa.

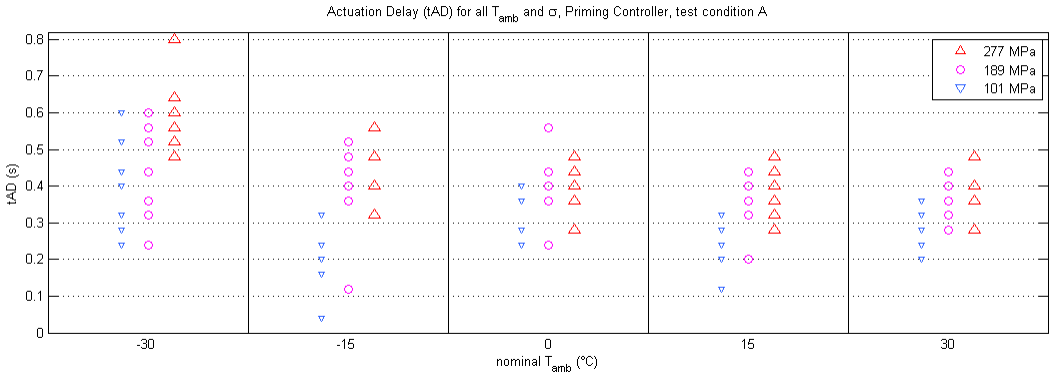

Figure 7.15: t_{AD} data for all test condition A trials at all stresses, plotted against the nominal T_{amb} setting for each trial.

The mean and standard deviation of t_{AD} values for each T_{amb} and σ setting is shown in Figure 7.16.

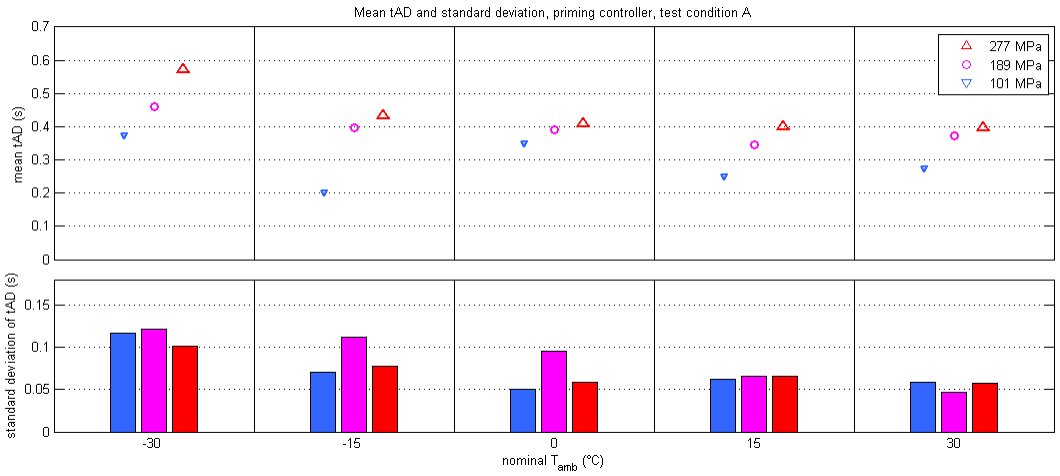

Figure 7.16: Mean and standard deviation of test condition A t_{AD} data at each T_{amb} and σ setting.

As seen from Figure 7.16, the mean t_{AD} for the Priming Controller is approximately in the range of 0.2s to 0.6s. There is no significant t_{AD} vs. T_{amb} trend, except that the mean t_{AD} values for -30°C nominal ambient temperature are higher than the mean t_{AD} at other T_{amb} settings. This shows the difference between the wire temperature and T_{peak} is greater at the T_{amb}=-30°C setting than at other T_{amb} settings, which causes t_{AD} to be larger at this setting.

There is, however, a noticeable trend in t_{AD} vs. σ. This shows that although the Priming Controller was designed to allow a consistent t_{AD} to be achieved regardless of T_{amb} and σ, it is probably more effective in compensating for different constant T_{amb} values than different constant σ values.

Looking at the standard deviation of t_{AD} for trials at each T_{amb} and σ, one can see that a smaller deviation in t_{AD} is exhibited with higher T_{amb}. These results indicate that even with the Priming Controller in place, the sensitivity of the SMA to air flow variations is still greater at lower ambient temperatures, leading to a larger variability in t_{AD}, similar to the behaviour observed in the No-priming Controller trials.

Finally, an anomaly in t_{AD} in all trials performed at the T_{amb}=-15°C, σ=101MPa setting can be observed when compared to other ambient settings (the t_{AD} for this setting is a lot lower than t_{AD} at other settings). Upon further investigation, it was seen that in the data collected for all trials at this setting, the initial buffer segment did not span the full 2 seconds designed duration and the actuation command time for all trials are slightly before 60s, indicating that the Simulink software environment may have experienced some issues and became desynchronized with computer hardware that was executing the controller algorithm. The t_{AD} anomaly for this T_{amb} and σ setting is hypothesized to be due to the same hardware issues where the controller algorithm executed slightly differently from the other T_{amb} and σ trial sets.

Figure 7.17 below is a comparative presentation of the mean and standard deviation t_{AD} data for both the Priming Controller and No-priming Controller trials.

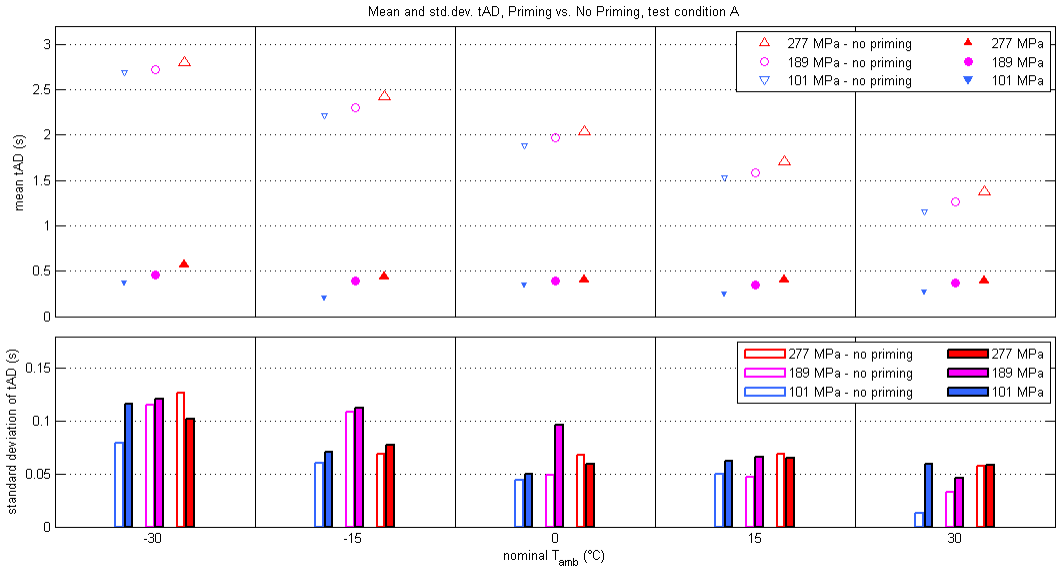

Figure 7.17: Comparison between test condition A No-priming and Priming Controller t_{AD} data at each T_{amb} and σ setting.

It can be seen that the 0.2s to 0.6s t_{AD} range of the Priming Controller is a significant improvement from the 1.1s to 2.8s t_{AD} range of the No-priming Controller. Furthermore, t_{AD} of the Priming Controller is also much more consistent at different T_{amb} settings than the No-priming Controller, which shows that the Priming Controller is very successful at compensating for different T_{amb} values.

For the Priming Controller, the difference in t_{AD} for the same T_{amb} but different stresses is comparable to that of the No-priming Controller, with that difference being slightly less at higher ambient temperatures. This shows that at different but invariant σ settings, the Priming Controller offers little to no improvement in actuation response speed over the No-priming Controller.

As shown in Figure 7.17, at each T_{amb} and σ setting, the standard deviation in Priming Controller t_{AD} is similar to that of the No-priming Controller, with the trials tested at the highest stress (277MPa) being the most similar. For lower stresses, the standard deviation of t_{AD} of the Priming Controller is generally slightly higher than the No-priming Controller, demonstrating that there is a small trade-off between using priming to achieve a lower t_{AD} and consistency in t_{AD} under identical conditions.

Overall, the Priming Controller allows a much smaller and more consistent t_{AD} to be achieved at different T_{amb} settings than the No-priming Controller, while there is no significant improvement in the consistency of t_{AD} at different σ settings. Additionally, for repeat trials performed at the same (invariant) T_{amb} and σ setting, the variability of the t_{AD} of the Priming Controller is comparable to that of the No-priming Controller.

7.5.1.3 Test condition B

The t_{AD} data for all experimental trials conducted in test condition B are shown in Figure 7.18, where the t_{AD} for each trial is plotted against the $T_{amb,act}$ of that trial. In Figure 7.19 the mean and standard deviation of t_{AD} for each stress setting is presented and also compared to those of test condition A.

It is expected that the t_{AD} data from test condition B trials should be similar to those in test condition A trials. Due to the transient T_{amb} sensor error previously described in Section 7.2 it is also expected that there may be more variability in test condition B t_{AD} data than in test condition A.

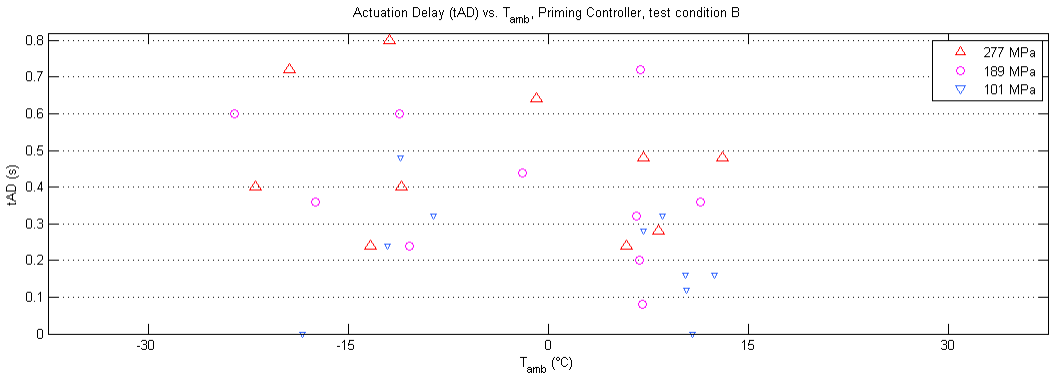

Figure 7.18: t_{AD} data for all test condition B trials.

There does not appear to be a correlation between t_{AD} and $T_{amb,act}$ in Figure 7.18. Since in test condition B T_{amb} is changing during the maintenance segment, Figure 7.18 shows that the Priming Controller is able to keep t_{AD} in the same range regardless of what value T_{amb} has changed to at actuation command time.

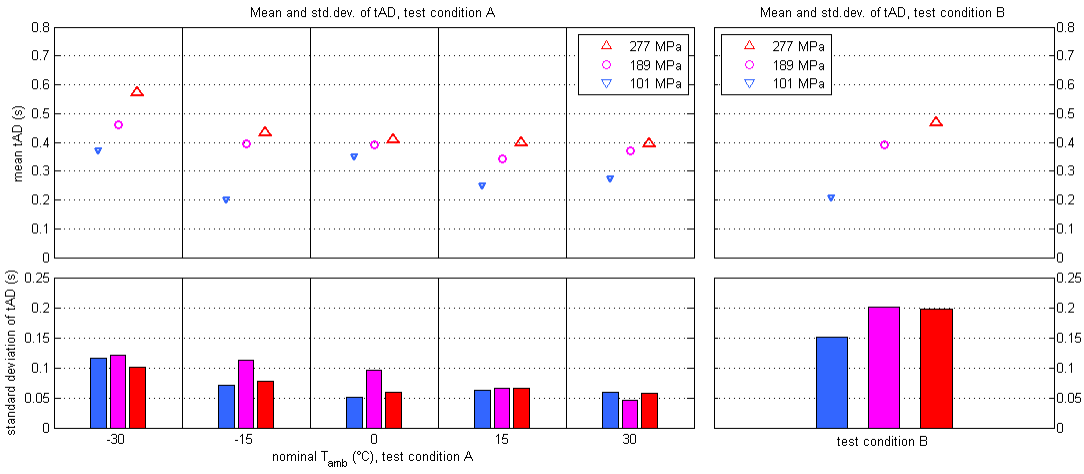

Figure 7.19: Mean and standard deviation of (right) test condition B t_{AD} data at each σ setting, compared to (left) the t_{AD} data for test condition A.

From Figure 7.19, it can be seen that the range of mean t_{AD} for test condition B trials is 0.2s to 0.5s, similar to the mean t_{AD} range of test condition A. Recall that the mean t_{AD} range for No-priming trials was 1.1s to 2.8s. It can then be concluded that in a condition of varying ambient temperature, the Priming Controller still offers a much improved actuation response time than the No-priming Controller, and the t_{AD} improvement is comparable to the t_{AD} improvement of the Priming Controller over the No-priming Controller in test condition A.

Finally, in test condition B, a t_{AD} vs. σ trend similar to that of test condition A is observed. This shows that t_{AD} is roughly the same at each stress setting in both test conditions A and B.

A higher t_{AD} standard deviation can be observed for the set of trials at each stress setting in condition B than in test condition A through Figure 7.19. Recall that in section 7.2 it was mentioned that transient sensor error was observed in the T_{amb} feedback signal on the experimental setup, so it is hypothesized that the higher t_{AD} variance in condition B is caused by the sensor error when the ambient temperature is changing.

Overall, the average t_{AD} of the Priming Controller trials in test condition B is in the same range as the average t_{AD} of the test condition A trials, as expected. There is more variation in

t_{AD} for repeated trials for each of the three stress settings in test condition B than in test condition A, and it is conjectured to be due to sensor error.

7.5.1.4 Test condition C

In trials conducted in test condition C, both T_{amb} and σ are varied during the maintenance segment. Two test condition C scenarios were tested, one where the stress increases from 101MPa to 277MPa (i.e. l2h scenario), and one where the stress change is reversed (i.e. h2l scenario). The t_{AD} data for all test condition C trials are shown in Figure 7.20, where the t_{AD} for each trial is plotted against the $T_{amb,act}$ of that trial. Figure 7.21 shows the mean and standard deviation of t_{AD} for each of the two test condition C scenarios. Also shown in Figure 7.21 are mean and standard deviation of t_{AD} values from test condition A and B.

Once again, the t_{AD} values for test condition C are expected to be in the same range as those for test conditions A and B.

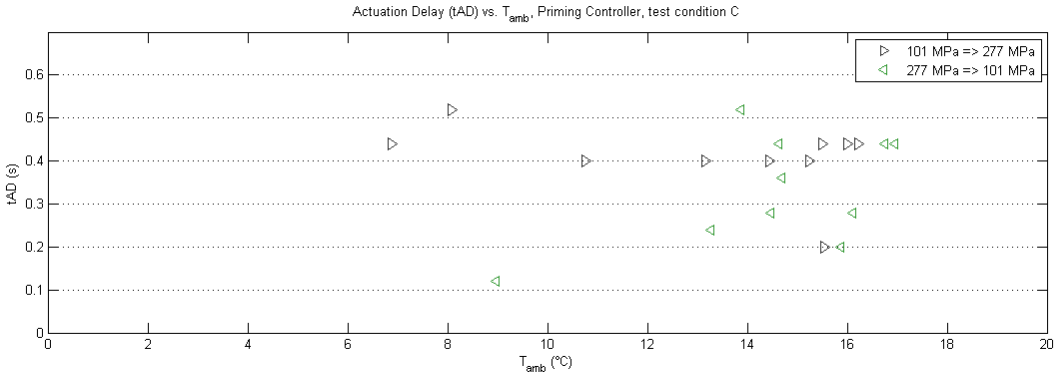

Figure 7.20: t_{AD} data for all test condition C trials.

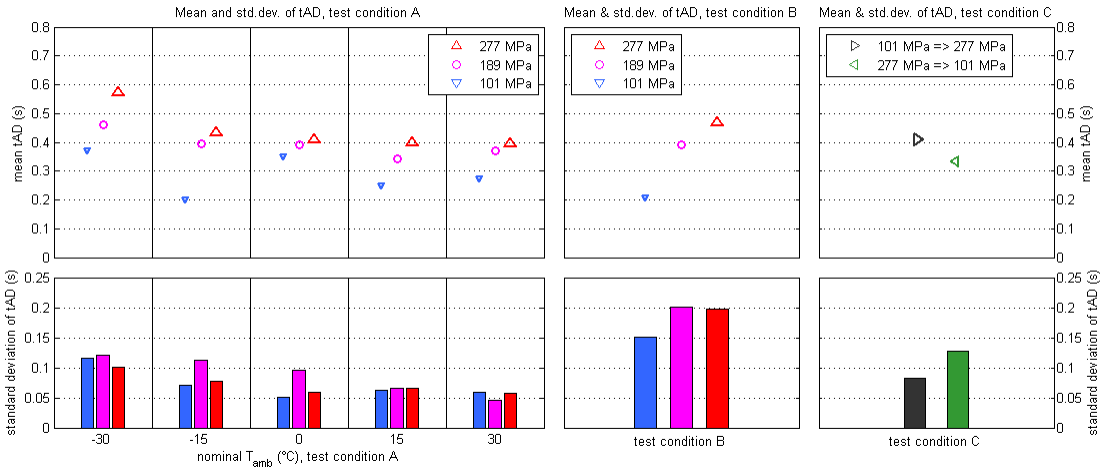

Figure 7.21: Mean and standard deviation of test condition C t_{AD} data at each σ setting (rightmost), compared to the t_{AD} data for test conditions A and B.

It is observed from Figure 7.20 and Figure 7.21 that the average t_{AD} values for test condition C trials are in the same range as test conditions A and B, which shows that the Priming Controller is able to allow the SMA actuator to achieve consistent actuation times regardless of T_{amb} and σ conditions.

Furthermore, it's shown in Figure 7.21 that the standard deviation of t_{AD} for trials performed in each of the l2h and h2l scenarios is also in the same range as test conditions A and B. Specifically, the standard deviation of t_{AD} in test conditions C are generally slightly higher than those of test condition A, while slightly lower than those of test condition B. Because T_{amb} could not be controlled as well in test condition C as it could be in condition B, the range of T_{amb} variation is lower in test condition C trials, and that could be the reason that lower t_{AD} variance values are observed in test condition C.

7.5.2 Measuring performance using SM and SV

In the previous subsection we saw that the Priming Controller has achieved its goal of allowing the SMA actuator to achieve a superior response time compared to the No-priming

Controller. The average t_{AD} range for the No-priming Controller trials was 1.1s to 2.8s while the average t_{AD} range for the Priming Controller trials was 0.2 to 0.6s. Furthermore, the Priming Controller was able to keep the average t_{AD} fairly consistent across all three test conditions. However, since t_{AD} is measured in the actuation segment of the trial runs, it only shows the result of priming, and says nothing of the behaviour of the SMA actuator during the maintenance segment. The Mean Strain (SM) and Strain Variation (SV) metrics were devised to measure how well the Priming Controller keeps the SMA actuator in a "primed state" during maintenance, and the results of SM and SV evaluation are presented in this section. Once again, please note that SM and SV are not applicable to the No-priming Controller trials since those trials lack a maintenance segment.

7.5.2.1 Condition A

Figure 7.22 to Figure 7.24 presents the SM and SV values for all trials performed at each T_{amb} and σ setting in test condition A. In these figures, the SM and SV values are plotted against the $T_{amb,act}$ value of the trials run during the maintenance segment. Figure 7.25 illustrates the mean and standard deviation of SM for the set of ten trials conducted at each T_{amb} and σ setting, while Figure 7.26 illustrates the mean and standard deviation of SV for each T_{amb} and σ setting.

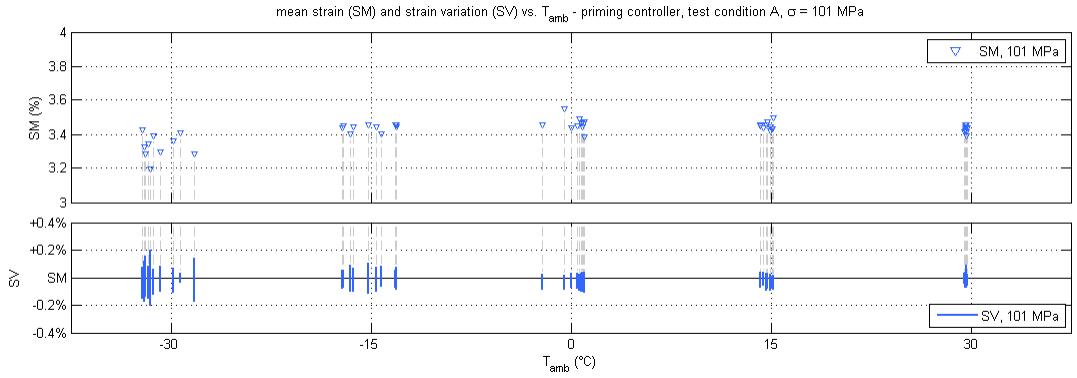

Figure 7.22: SM and SV data for all test condition A trials at σ = 101MPa.

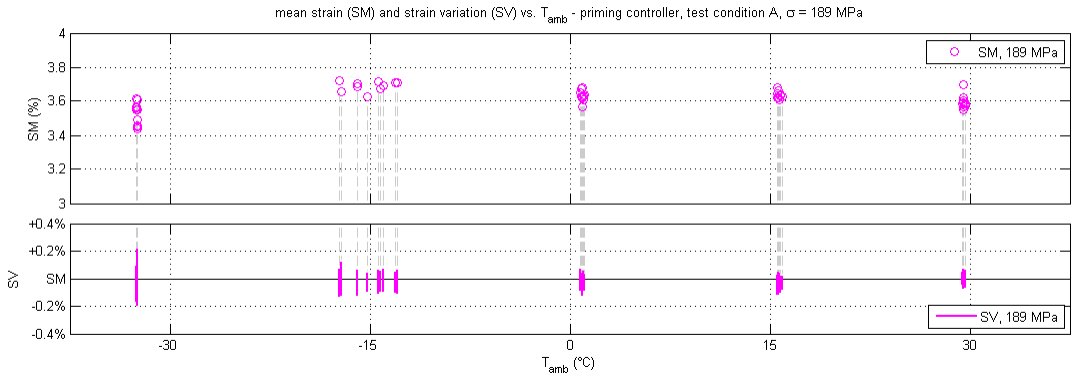

Figure 7.23: SM and SV data for all test condition A trials at σ = 189MPa.

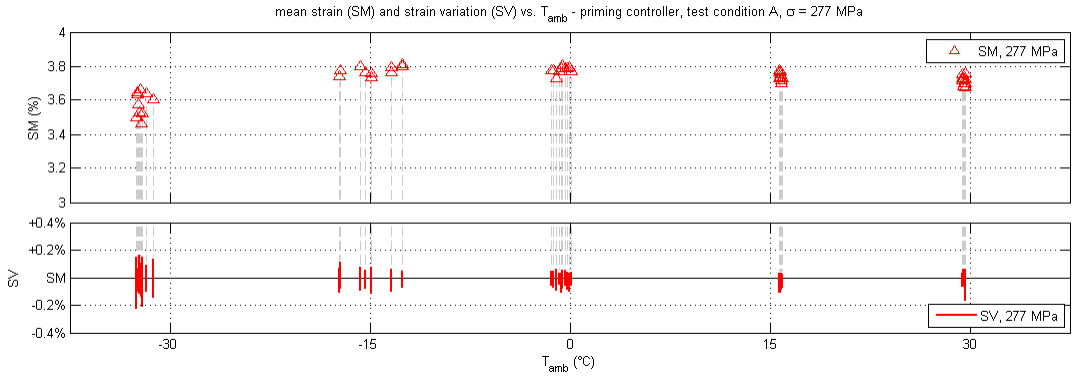

Figure 7.24: SM and SV data for all test condition A trials at σ = 277MPa.

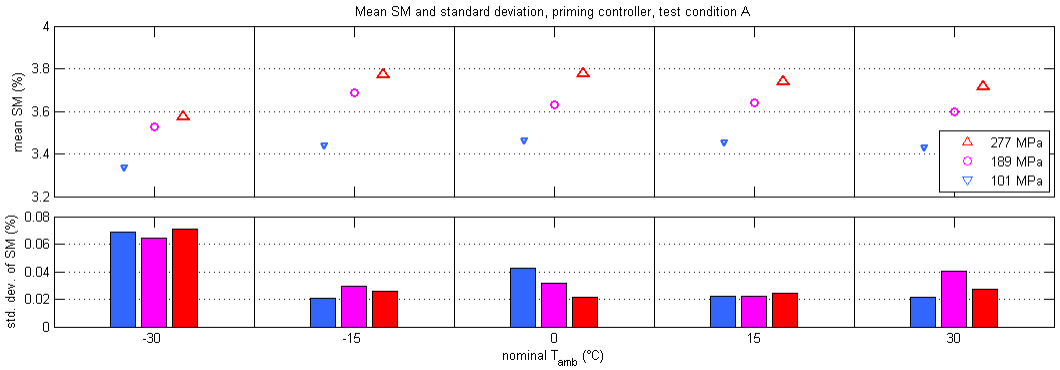

Figure 7.25: Mean and standard deviation of SM for all test condition A trial sets.

From Figure 7.25, it can be seen that, with the exception of trials at T_{amb}=-30°C, the average SM for σ = 101MPa, 189MPa and 277MPa settings are around 3.45%, 3.62% and 3.75% respectively. At T_{amb}=-30°C, the average SM values are lower than those at other T_{amb} settings, suggesting that either a) the SMA actuator was over-actuated during the maintenance segment (resulting in a lower strain); or b) when the wire was fully actuated it did not achieve the same amount of contraction as it did for the other T_{amb} settings, i.e. it was slightly under-actuated during the actuation segment. If the SMA actuator was over-actuated, it would mean that the wire was at a higher temperature than during the maintenance segment compared to the trials at the other T_{amb} settings, resulting in a lower t_{AD}. However, looking at Figure 7.16, the t_{AD} for the T_{amb}=-30°C trials is actually slightly higher than those at the other T_{amb} settings, which means the SMA actuator was not over-actuated. So the lower SM values for T_{amb}=-30°C trials were probably a result of slight under-actuation during the actuation segment.

As for the average SM value at different wire stresses, it can be seen that the SM difference between the lowest stress setting and the highest setting is around 0.3% for all T_{amb} settings. The increased SM with increased σ behaviour is expected, since at a higher stress the wire strain should be larger (assuming that the phase fraction and wire temperature is the same).

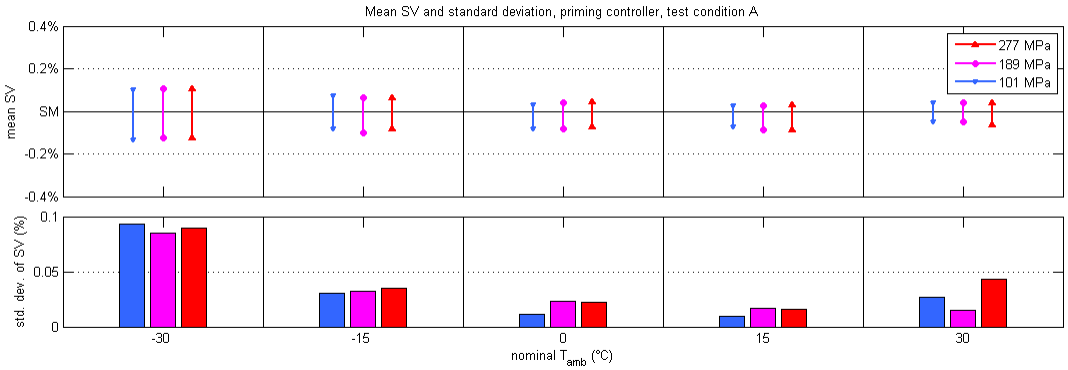

Figure 7.26: Mean and standard deviation of SV for all test condition A trial sets.

Figure 7.26 shows the average SV for all T_{amb} and σ settings are around -0.1% to +0.1%, which correspond to a total displacement variation of 0.57mm for the 28.3cm wire. The SV range decreases with increasing T_{amb}. This is conjectured to be due to the magnified effect of convection disturbances at lower T_{amb} values. When the difference between the wire temperature and T_{amb} is large, the effect of disturbances in the convection characteristics of the air near the nitinol wire is magnified, causing the wire temperature to have greater variations during the maintenance segment compared to the other T_{amb} settings. The result is that at lower T_{amb} settings, the strain variation during the maintenance segment would have been larger. At all T_{amb} settings, the average SV is roughly the same for the three σ settings, showing that the wire stress does not have an effect on the range of strain variation during the maintenance segment.

In terms of the variance of SM and SV values at each T_{amb} and σ setting as measured using the standard deviation of those quantities, the T_{amb}=-30°C trials exhibit the highest SM and SV variance at all stresses tested. This is very similar to the relatively high t_{AD} variance also observed for T_{amb}=-30°C. It is hypothesized that once again at lower T_{amb} the magnified effect of convection disturbances causes a larger variability in both the mean strain and the range of strain variations during the maintenance segment of the trials.

7.5.2.2 Condition B

Figure 7.27 to Figure 7.29 illustrate the SM and SV results for trials performed at test condition B. In, Figure 7.27, the SM and SV data for all trials are plotted in three groups, each group for one of the three σ settings in test condition B. In Figure 7.28 and Figure 7.29, the mean and standard deviation of SM and SV for the set of trials at each σ setting is plotted, along with the same data set for test condition A for comparative viewing.

It is expected that the SM of test condition B trials should be similar to those of test condition A trials at each σ setting.

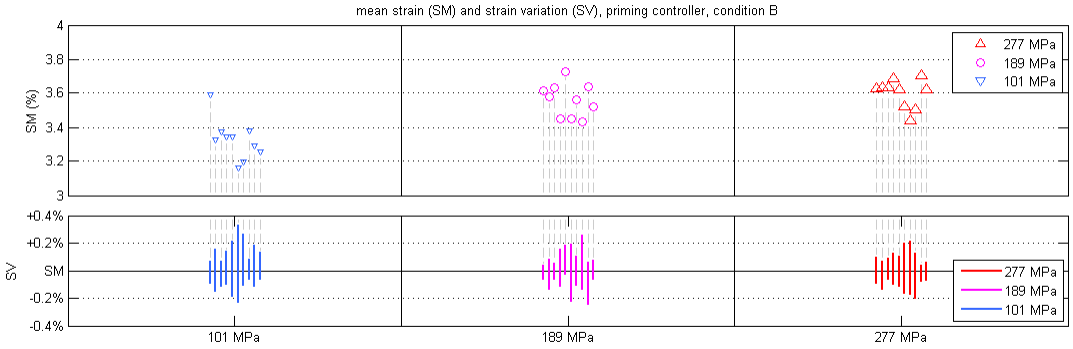

Figure 7.27: SM and SV data for all test condition B trials. For each stress setting, the data are plotted against the order in which the trials were performed.

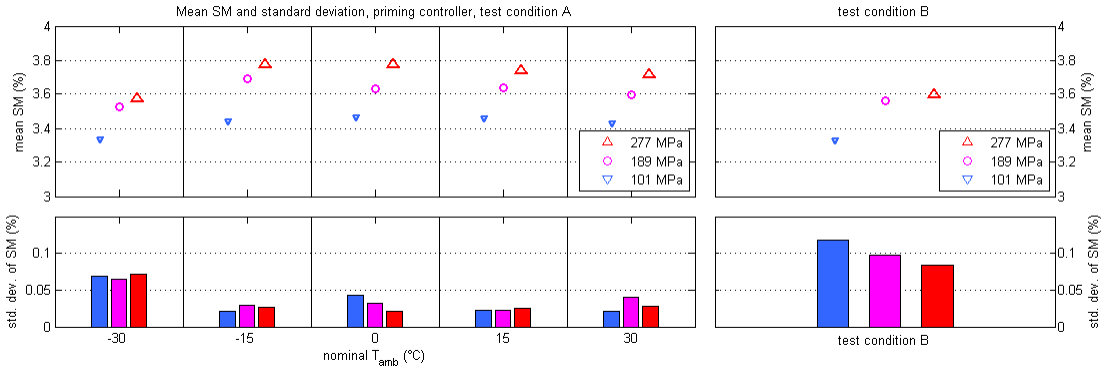

Figure 7.28: Mean and standard deviation of SM for (right) test condition B trial sets compared to (left) those of test condition A trials.

Figure 7.28 shows that the average SM value for test condition B trials is slightly lower than other of most test condition A trials. They are, however, very similar to the SM value of test condition A trials at the T_{amb}=-30°C setting.

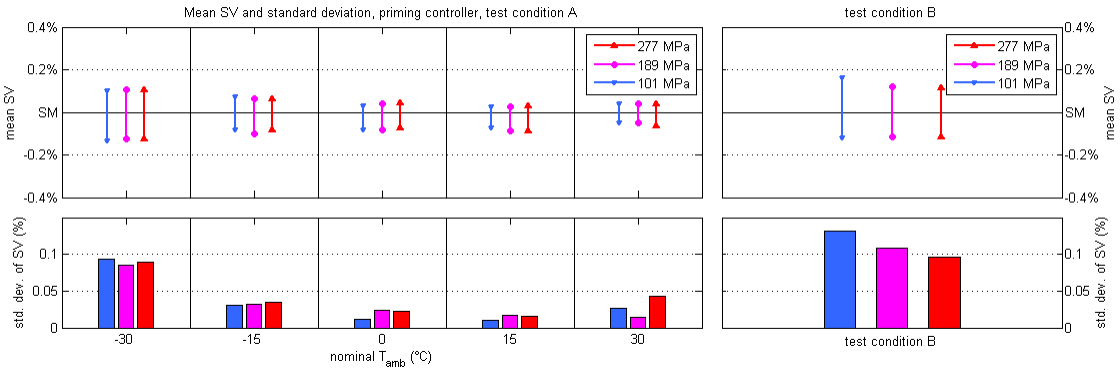

Figure 7.29: Mean and standard deviation of SV for (right) test condition B trial sets compared to (left) those of test condition A trials.

Figure 7.29 shows a higher average SV range for test condition B compared to condition A. This is expected since the ambient temperature is constantly changing in test condition B trials, and since there is some sensor error present in the T_{amb} signal, the controller will not be as good at maintaining a constant wire temperature in test condition B as it is in condition A. However, the average SV range for test condition B is between -0.15% to +0.15% (or ±0.43mm), which is still a small range.

In terms of the variance in average SM and SV values measured using standard deviation, both Figure 7.28 and Figure 7.29 show larger SM and SV variances for test condition B trials than test condition A trials. This is very much similar to the larger t_{AD} variance for test condition B, and the reason is probably the same for both.

7.5.2.3 Condition C

The SM and SV data for test condition C are presented in Figure 7.31 through Figure 7.34. Recall that for test condition C, two stress change scenarios are tested, one where the stress changes from 101MPa to 277MPa (l2h scenario) and one where the stress change is reversed (h2l scenario). For trials tested in each scenario, there is a high stress regime and a low stress

regime during the maintenance segment (as shown in Figure 7.6), so two sets of SM and SV data are generated for each trial, one for each regime.

In Figure 7.2, it was shown that the zero-strain was determined as the displacement measured when the wire is fully actuated. However, for different wire stresses, the length of a fully actuated wire would be slightly different due to the finite elastic modulus of the nitinol wire in A-phase. This means that in test conditions A and B, when the wire was fully actuated and at 0% strain, the absolute wire length would have been slightly different. This also means that for each trial in test condition C, the zero-strain of each of the two stress regimes would be different from each other.

Figure 7.30 illustrates the difference in absolute strain of the fully actuated nitinol wire as a result of different stresses. In Figure 7.30, the SMA actuator was fully actuated using the No-priming Controller, and when it had reached steady-state, the stress on the wire was changed repeatedly between 101MPa and 277MPa. Figure 7.30 shows that the fully-actuated strain difference between the high-σ and low-σ regimes is on average 0.417%.

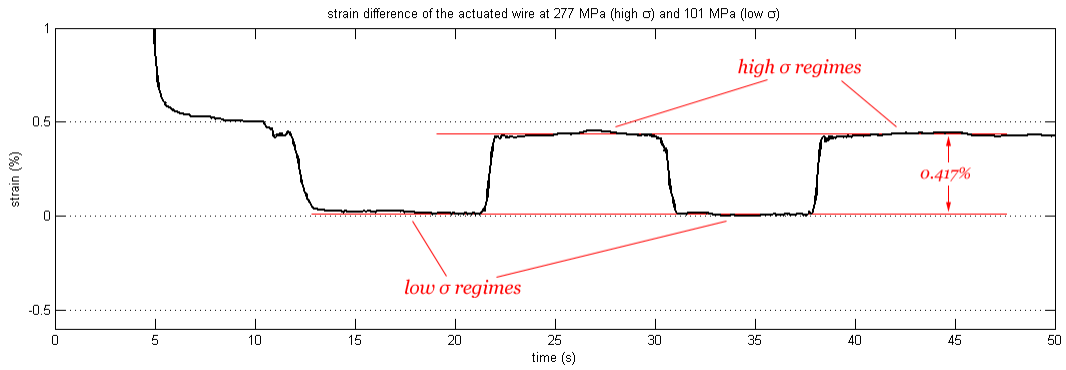

Figure 7.30: Differences in "zero strain" of the SMA wire for a high σ (277MPa) and a low σ (101MPa).

In the l2h scenario of test condition C, the wire was actuated while σ=277MPa, i.e. the stress of the high-σ regime. So to allow the low-σ regime SM value to be compared with the 101MPa SM values in the other test conditions, it was adjusted by adding 0.417% to its

value. Similarly, the high-σ regime SM for the h2l scenario was adjusted by subtracting 0.417% to its value in order to compare with the 277MPa SM values at test conditions A and B.

Figure 7.31 and Figure 7.32 show the SM and SV data for all trials conducted in test condition C; while Figure 7.33 and Figure 7.34 show the mean and standard deviation of SM and SV values for the trials each of the l2h and h2l scenarios, compared to those of test conditions A and B.

It is expected that the high-σ and low-σ regimes SM values for the l2h trials should be similar to the high-σ and low-σ regimes SM values respectively for the h2l trials. It is also expected that the low-σ regime SM values for both condition C scenarios should be similar to the 101MPa SM values from test conditions A and B, while the condition C high-σ regime SM values should be similar to condition A and B 277MPa SM values.

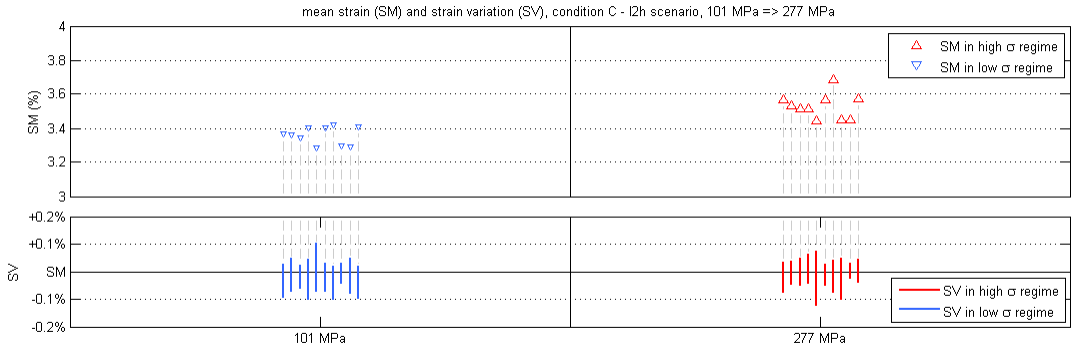

Figure 7.31: SM and SV data for all test condition C trials in the l2h scenario.

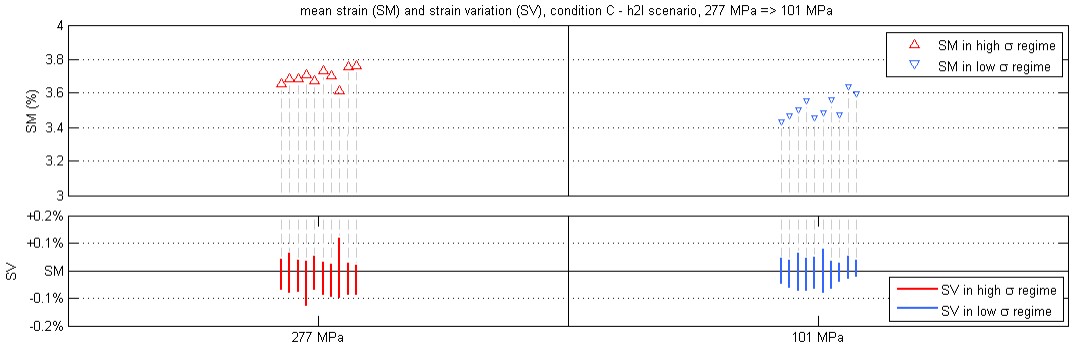

Figure 7.32: SM and SV data for all test condition C trials in the h2l scenario.

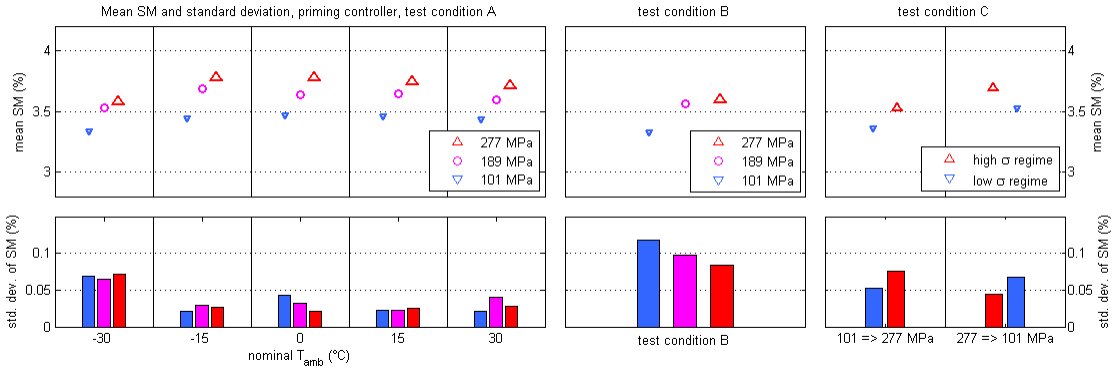

Figure 7.33: Mean and standard deviation of SM for test condition C trial sets (rightmost) compared to those of test condition A and B trials.

It is seen in Figure 7.33 that the average high-σ regime SM in both l2h and h2l scenarios are slightly higher than the average low-σ regime SM values, by about 0.2%. In the l2h scenario, the low-σ regime SM is around 3.3% and the high-σ regime SM is about 3.5%; while in the h2l scenario, the SM values for the low-σ and high-σ regimes are around 3.5% and 3.7% respectively. The positive SM-to-σ observed independently for both test scenarios are consistent with those observed in test conditions A and B. Comparing across the l2h and h2l scenarios, it is seen that the average high-σ as well as low-σ SM differ by about 0.2%, contrary to the expectation. Overall, the average high-σ and low-σ SM values for test condition C trials are in the same average SM range as test conditions A and B.

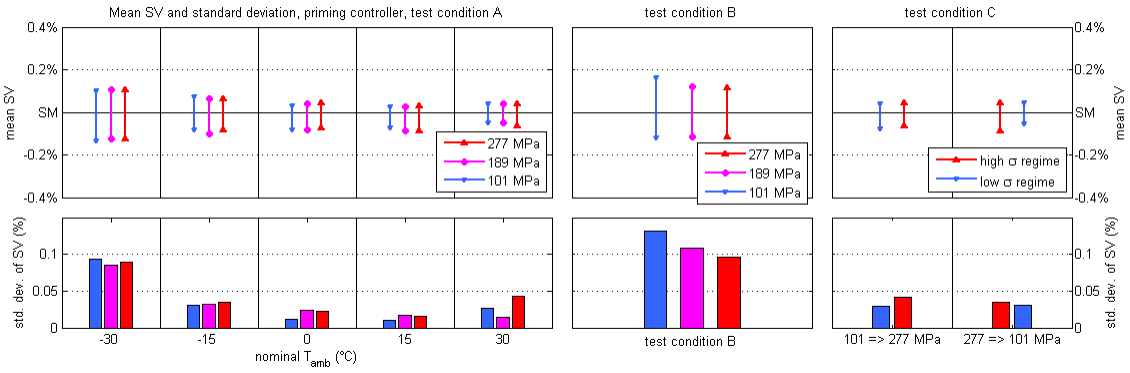

Figure 7.34: Mean and standard deviation of SV for test condition C trial sets (rightmost) compared to those of test condition A and B trials.

From Figure 7.34, it is clear that the SV values in both the high-σ and low-σ regimes for both l2h and h2l scenarios are similar to those of test condition A and lower than those of test condition B. The reasoning behind this is thought to be that the T_{amb} variations during test condition C trials are less extreme than those of test condition B trials, so there is comparatively less T_{amb} feedback error in test condition C which resulted in a smaller average SV.

As for the variances in SM and SV as measured using the standard deviation of those quantities, once again they are comparable to those of test condition A and less than those of test condition B. The reason is also thought to be the same as described in the previous paragraph.

7.6 Conclusions drawn from the results

Analysis and discussion about the experimental results allow conclusions to be made with respect to the Priming Controller*'s* performance in each of the three criteria listed in Chapter 3.

7.6.1 Quality of priming

The data presented in Subsection 7.5.1 and relevant discussion shows that the Priming Controller design has accomplished its goal of improving the response time of SMA toggle actuators. Figure 7.17 shows that in the experimental evaluation of this research, the average t_{AD} for trials where the SMA actuator is actuated without priming is in the range of 1.1s to 2.8s, whereas for trials where priming is implemented, the average t_{AD} is in the range of 0.2 to 0.6s (under constant T_{amb} and σ conditions). Figure 7.35 shows that using priming resulted in a 3.5- to 11- fold improvement of t_{AD} compared to without priming.

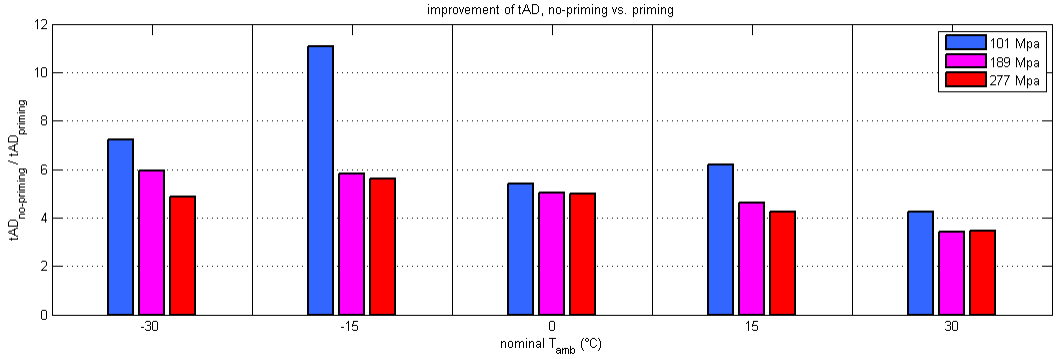

Figure 7.35: Improvement of t_{AD} using the Priming Controller, as a factor compared to using the No-priming Controller. The t_{AD} data are mean t_{AD} values for test condition A Priming and No-priming trials.

Figure 7.21 shows that even in dynamic T_{amb} and σ conditions, the Priming Controller design was able to achieve a t_{AD} time within the same range as static T_{amb} and σ conditions.

The quality of priming was not only measured using t_{AD}, but also using SV or the variation in strain during the maintenance segment. Figure 7.34 shows that in all T_{amb} and σ test conditions, the wire strain varied within the range of ±0.15% on average during the maintenance segment, or ±0.425mm. Considering that the average strain during the maintenance segment for all trials is approximately 3.5% or 9.9mm, the strain variation

represents a less than 5% variation of the "primed" strain of the nitinol wire. This ensures that the SMA actuator would not produce significant movements in practical applications when it is primed.

7.6.2 Repeatability of priming

The repeatability of priming is judged by analysing the variations in t_{AD}, SM and SV measures across trials at each T_{amb} and σ condition. Figure 7.17 shows for static T_{amb} and σ conditions, the standard deviation of t_{AD} for the Priming Controller trials are in general slightly higher than those of the No-priming Controller trials, but very similar regardless; while Figure 7.21 shows that when either T_{amb} or σ is changing, the standard deviation of t_{AD} across multiple trials become higher. From Figure 7.21 it's shown that the maximum standard deviation of t_{AD} in all test conditions is 0.2s, which means in the worse-case scenario, t_{AD} deviated up to 0.2s from the expected value in 68% of the trials repeated at the same T_{amb} and σ condition.

In terms of SM and SV, Figure 7.33 and Figure 7.34 show that there is a larger variance in both SM and SV in dynamic T_{amb} and σ conditions compared to static conditions, similar to the observed variations in t_{AD}. From Figure 7.33 it's seen that the maximum standard deviation in Mean Strain for all test conditions is around 0.12%, meaning that in the worst case scenario, there was a deviation of up to 0.12% from the average strain in 68% of all trials repeated at the same T_{amb} and σ condition.

It could hence be concluded that the repeatability of priming is higher under static T_{amb} and σ conditions than under dynamic T_{amb} and σ conditions. As mentioned previously, there is a high chance that the less optimal repeatability performance for a condition of dynamic T_{amb} is due to the sensor error in the T_{amb} sensor.

7.6.3 Consistency of priming

The consistency of priming is measured by looking at the differences in t_{AD}, SM and SV across different T_{amb} and σ conditions. In Figure 7.21 it is shown that in all test conditions (both static and dynamic) the average t_{AD} for the priming trials are in the range of 0.2s to 0.6s, a 0.4s range, while for the no-priming trials, the average t_{AD} were in the range of 1.1s to 2.8s, or a 1.7s range. This shows that using priming did result in significantly less variability in the response time across different T_{amb} and σ conditions, compared to not using priming.

It was also seen in Figure 7.21 that for different stresses, the t_{AD} of the Priming Controller trials had a similar trend to that of the No-priming trials, while for different ambient temperatures, the t_{AD} is approximately the same for the Priming Controller trials. This shows that the Priming Controller is better at reducing the variability of t_{AD} for different static ambient temperatures than for different static stresses.

Chapter 8

Conclusions and future work

At the beginning of this research, the goal was set out to design a priming controller for SMA toggle actuators that allows a shorter and more consistent response time to be achieved across the range of both static and dynamic operating conditions. Specifically, the operating conditions correspond to the ambient temperature and the stress on the SMA wire, which may be different and changing during actuation events in application. The priming controller works by pre-emptively heating the SMA wire up to the cusp of actuation, then maintaining it there until actuation is triggered. It was seen that, using the same actuation strategy and in the same test conditions, the priming controller did result in a much more rapid and consistent response time for the SMA actuator compared to without the priming controller. In addition, the priming controller was able to compensate for dynamic changes in the ambient temperature and stress while the primed state was maintained, which resulted in a consistent actuation performance for all possible operation scenarios. Furthermore, the only feedback quantities for the priming controller were the SMA resistance and the ambient temperature, and the feedback mechanisms for both quantities are inexpensive to implement and require almost no increase in the system size of the SMA actuator.

While the priming controller achieved its goal and was shown to be more robust than previous priming works in [2, 6], improvements may be made in several areas for future work. First of all, it was shown that when the ambient temperature is changing, the SMA wire exhibited more strain variations as well as greater variations in the Actuation Delay Time and Mean Strain measures compared to a static ambient temperature condition. It was

conjectured that this is due to sensor error in the ambient temperature feedback signal. Therefore, it is highly valuable to implement and test the priming controller design in an experimental setup where the ambient temperature feedback is more accurate.

Secondly, the controller relies on a thermodynamic model to predict the temperature of the SMA wire, and this temperature prediction is used for intelligently adjusting the power output in the presence of dynamic changes in the ambient temperature and stress. The availability of ambient temperature feedback as well as (fairly) consistent convection characteristics of the test chamber resulted in an accurate on-line estimation of the SMA wire temperature. However, this is an open-loop process, and there is no mechanism for correcting the temperature estimation in the case of a mismatch between the estimated and actual wire temperature. In application, the ambient air convection characteristics cannot always be guaranteed to be disturbance-free, thus the robustness of the proposed methods to variations in convective conditions still needs to be tested, and a mechanism for checking the accuracy of the estimated wire temperature should be investigated.

Thirdly, in the design of the priming controller we assumed a maximum rate of stress decrease value, which allows us to define a temperature setpoint buffer T_{buffer} to prevent premature actuation during priming. The value of T_{buffer} is also affected by the tunable gain K_e in the inner system controller. Here, the values of T_{buffer} and K_e were determined in a heuristic manner to work for the SMA actuator system in our lab. However, since the maximum rate of stress decrease in practical applications can be vastly different from the assumed value here, a mathematical relationship between the maximum stress rate of change and the T_{buffer} and K_e values would be useful. Therefore, investigating this mathematical relationship can be a focus for future work.

Fourthly, the experimental platform for this research was designed to be robust against disturbances and noise in the supply voltage of the SMA actuator system. The Wheatstone bridge circuit design ensures that the SMA resistance is computed accurately regardless of the source voltage for heating the SMA wire; while a feed-forward source voltage signal

allows the duty cycle of the PWM driver to be adjusted to maintain the same power output if the source voltage were changed. However, the robustness to source voltage disturbances was not tested in this research, and it would be worthwhile to test this aspect of the design of the electrical system, since in practical applications, variations in source voltage may be more of an issue.

A final recommendation for future work is to extend the concept of robust priming to the reverse A→M transformation. In this work, the priming controller is only designed for priming the SMA actuator for M→A transformation which results in a one-way active actuation; however in many applications, two-way active actuation is required, often by using an antagonistically-arranged two-wire SMA actuator. In such scenarios, a robust priming controller design should also ensure that the cooling response time of the inactive SMA wire is minimized as much as possible.

Appendix A

Design of the experimental testing platform

In this Appendix, the design and implementation details of the electrical and software components of the experimental testing platform will be presented. In Section A.1 the design and implementation of the electrical system are explained, and then the software design is presented in Section A.2.

A.1 Electrical hardware design

The electrical circuitry is implemented on a Global Specialties Proto-Board 204 breadboard. This board is easy to use, flexible, and provides a lot of space for circuit elements. Furthermore, it comes with its own multi-mode power supply providing +5V, +12V, -12V and GND voltage references. In the current setup, only the +12V and GND voltages from this power supply are used, to power the op-amps used for signal amplification.

A.1.1 SMA driver circuit

A.1.1.1 PWM-based power supply

A Pulse Width Modulated (PWM) current is used to power the SMA wire. The most significant advantage to using a PWM voltage signal as opposed to a variable current source as the power signal is that PWM allows the SMA to be powered by a relatively high voltage (10~12 V) that results in a high signal-to-noise (SNR) ratio in the current path [22]. As we

will see later in this chapter, the circuitry design that allows the resistance of the SMA wire to be calculated is part of the driver circuit, so a high SNR ratio is necessary for high precision voltage measurements to be taken. This, combined with the design of the power circuit, eliminates the need for noise filtering in the voltage measurements to compute a clean resistance.

Another advantage of using a PWM driver is the simplicity and efficiency with which the power can be adjusted. The effective power input to the SMA can be changed by varying the pulse width (or *duty cycle*) of the PWM waveform. For example, an SMA wire that is driven at 25% pulse-width would have the full voltage across its two ends during 25% of the PWM driver period and have zero voltage the remaining 75% of the period, and therefore would consume one quarter of the full power on average. Because of this "digital switching" behaviour, power throttling can be achieved using a simple solid-state transistor, such as a MOSFET, that opens or closes the power circuit based on a digital output from the computer. Alternative modes of achieving adjustable power, such as with a variable current source or a fixed current source in combination with a potentiometer, would require a more complicated circuit design, while suffering from low power efficiency.

An Advanced Motion Controls PS16H60 linear AC to DC power supply is used to power the SMA, providing up to 60 V and 16 A of direct current. A high power rating is desirable to minimize transition times when the supply voltage is modulated with a high frequency PWM carrier signal.

It was previously noted that one application area of SMA toggle actuators is the automotive industry, so it was desired that the source voltage of the experimental setup should be made to match the source voltage typically seen in an automobile, which is 12VDC. However, the available high-power PS16H60 DC supply does not have a variable output, therefore an autotransformer is used to reduce the power supply's input voltage from 120V AC to about 24V AC, so that the DC output of PS16H60 power supply is 12V instead of 60V.

Finally, the voltage supply is pulse-width modulated via an IRL3502PBF low-side driver MOSFET.

A.1.1.2 Resistance sensing circuitry

In this research, the SMA wire's resistance is the only feedback from the SMA wire used by the controller, so the circuitry responsible for resistance sensing was designed with great care, with particular attention to the precision of the computed resistance. Compared to the previous electrical setup in [22], a new resistance sensing scheme is designed to improve the precision of circuit measurements. In [22], the SMA resistance is calculated using the measured voltage drop across the SMA wire and the calculated wire current. The wire current is calculated based on the voltage measured across a 0.03Ω current sense resistor connected in series with the SMA. The main problem with this approach is that absolute voltage measurements across the SMA wire and the current sense resistor were sent to the analog-to-digital converter (part of the interface between the circuit and the microprocessor). Since the resistance change of the SMA wire is relatively small relative to the absolute resistance value (around 10%), the voltage changes across the wire and the current sense resistor would be correspondingly small relative to their absolute values. The result is that only a fraction of the entire range of quantization levels on the ADCs are effectively being used to sense that change and both the accuracy and precision of the calculated resistance are negatively affected. Figure A.1 shows that in [22] the resistance signal calculated using the voltage measurements is both noisy and has a distinctive "segmented" shape which could be attributed to the imprecise voltage measurements.

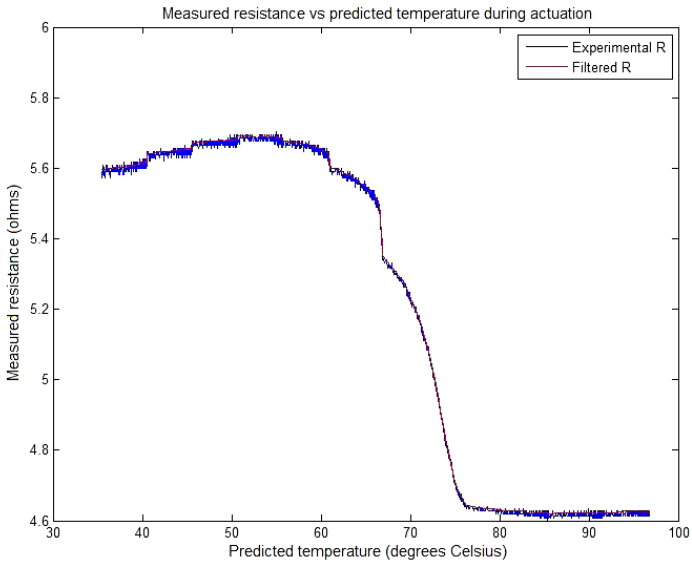

Figure A.1: Computed SMA wire resistance in [22]. Figure reproduced with permission from the copyright holder.

In the new and improved circuit design developed in this research, the circuit is designed so that the signal sent to the ADC represents the change in voltage instead of the absolute voltage value. This is accomplished by identifying a "nominal voltage" value across the SMA wire and offsetting the measured voltage by that nominal voltage using analog circuitry. Because the measured voltage is offset in-circuit, the computer software would need to be calibrated to interpret the measured voltages correctly; however, this would only need to be done once.

This new differential measurement scheme is implemented through a Wheatstone bridge circuit. As illustrated in Figure A.2, the Wheatstone bridge circuit consists of two voltage divider circuits known as "legs"; one would have a varying resistive element R_s (i.e. the resistance of the SMA wire, or *SMA resistance*), call the *unknown leg*; and the other would only have constant resistors, the *known leg*. The resistors R_o, R_{om} and R_{sm} in Figure A.2 are chosen so that the voltage at "A" – the midpoint of the known leg – acts as a nominal voltage reference for the voltage at "B" – the midpoint of the unknown leg. Any deviation from the

nominal voltage at "B" would be detected as a non-zero voltage in the differential voltage V_d. For example, a voltage change from 4.8V to 4.9V across the SMA wire the can be offset using a nominal voltage of 4.8V at "A" to yield a V_d change of 0 to 0.1V. This method allows up to 100% of the ADC resolution to be used for detecting the change in voltage as a result of the SMA resistance change.

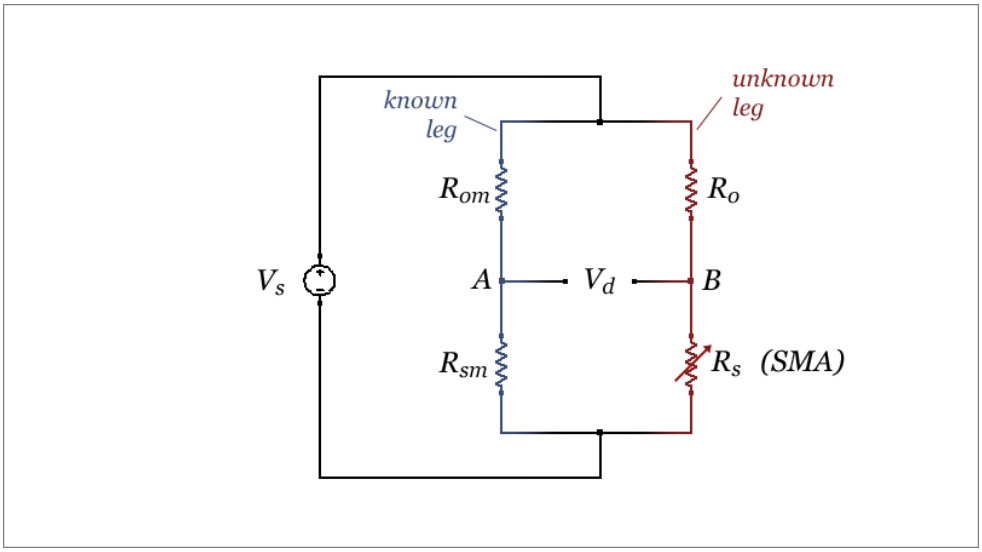

Figure A.2: An illustration of the Wheatstone bridge circuit implementation.

The SMA resistance can be computed by taking two voltage measurements: the voltage across the top and bottom of the bridge circuit (*source voltage*, or V_s); and the voltage drop across the middle nodes of the bridge (*differential voltage*, V_d). The relationship between V_d and V_S can be calculated as follows:

$$V_d = \left(\frac{R_s}{R_s + R_o} - \frac{R_{sm}}{R_{sm} + R_{om}}\right) V_s \tag{A.1}$$

Re-arranging (A.1) allows R_s to be calculated as follows:

$$R_s = \frac{R_O}{1 - \frac{R_{SM}}{R_{SM} + R_{OM}} - \frac{V_d}{V_s}} + 1 \tag{A.2}$$

The main benefit of using the Wheatstone bridge configuration is that small resistance changes in any one of the resistors is precisely detected. Another advantage is that as long as the constant resistance values are known and the voltages precisely measured, disturbances in the source voltage do not affect the accuracy of resistance calculation.

At the same time, there are several shortcomings which may cause complications in the future:

- Any changes in the constant resistor values due to temperature disturbances would reduce the precision of the calculated SMA resistance. If we assume that resistors R_o, R_{om} and R_{sm} are located physically close to each other and have the same Temperature Coefficient (TC), then their resistances would be scaled by the same factor with a temperature disturbance. The voltage at "A" in Figure A.2 would not be affected by this temperature disturbance, since the voltage divider nature of the known leg means changes in R_{om} and R_{sm} effectively cancel each other out. However, there is nothing to compensate for the change in resistance of R_o, so R_s would be inaccurately computed using (A.2).

- Due to the connection of the bridge circuit voltage measurements to the ADC (maximum range of 0 to 10 V), there is a minimum and maximum SMA resistance range that can be accurately measured. Any SMA resistance variations exceeding these min and max limits would cause saturation to 0 or 10V in the ADC. This also means that if the physical dimensions of the SMA wire are changed significantly in the future to cause a larger change in the resistance values, the bridge will need to be redesigned accordingly. Fortunately this is offset by the simplicity of the bridge circuit design, and can be easily modified if the actuator application demands vastly different physical specifications from the experimental setup in this research.

Due to the high precision requirement of these resistor values, the resistances are not arbitrarily chosen. The procedure for appropriately choosing the resistance values are described as follows:

- $\boldsymbol{R_s}$**:** This represents the SMA element. In the "in-fridge experiment" setup the 28.3-cm .010" Flexinol wire has a nominal resistance of 5.5Ω at room temperature. From past data and experimental measurements the SMA resistance is expected to vary in the range of 4.5Ω to 6.5Ω. A 4.5Ω "dummy" resistor was used in place of the SMA wire to allow the other resistors to be selected.

- $\boldsymbol{R_o}$**:** To keep the power dissipation low, the same 0.03Ω current sense resistor used in [22] is used here. The actual measured resistance, including the resistance of the wire connections around this resistor, is 0.0366Ω. This resistance was measured with the four-wire sensing method using a precision ohmmeter.

- $\boldsymbol{R_{sm}}$**:** The "mirror" resistor to R_s. This designed resistance is 26.1kΩ.

- $\boldsymbol{R_{om}}$**:** The "mirror" resistor to R_o. This designed resistance is 230Ω.

The above resistance values are nominal values for the resistors. It is expected that the actual resistances for R_{om} and R_{sm} may be slightly different from these values due to the tolerances or measurement error, so in addition to the effort spent here in carefully choosing the resistors, a system identification procedure was used to calibrate the software algorithm that computes the SMA resistance using V_d and V_s, and will be explained in detail in Subsection A.2.2.1.

Note that both R_{sm} and R_{om} resistances are chosen to be about 5000 times the resistances of R_s and R_o to minimize the power consumption of the known leg.

Figure A.3 shows the diagram for the SMA driver circuit.

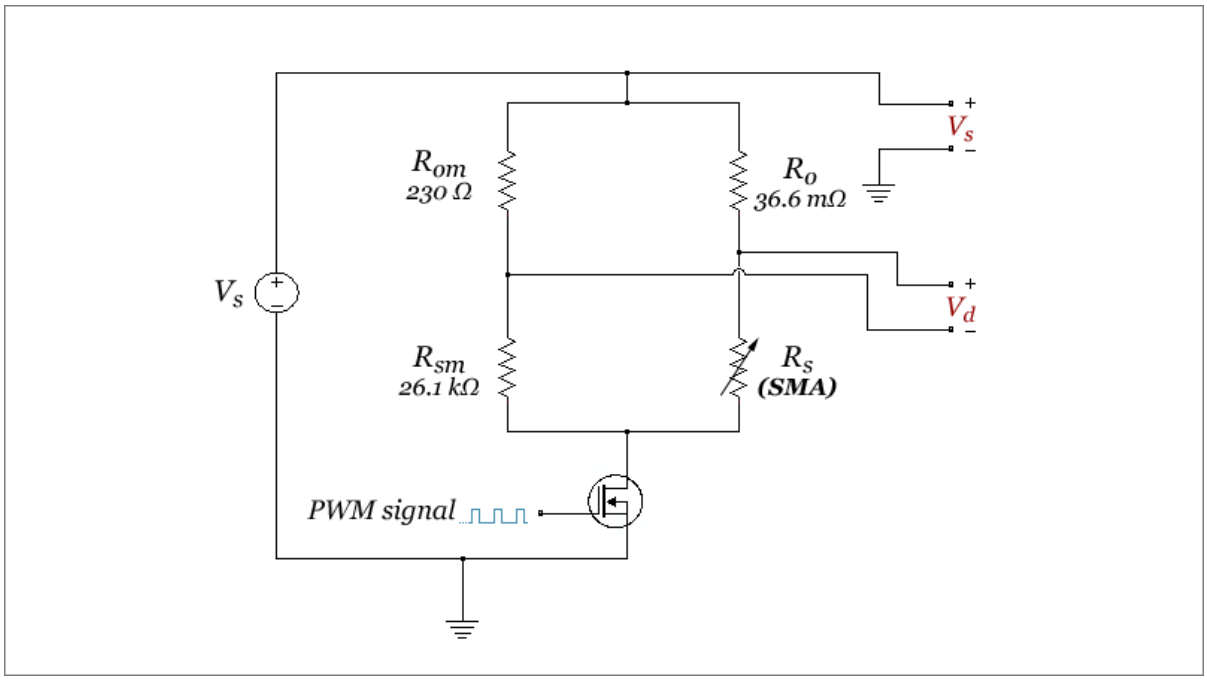

Figure A.3: Diagram of the SMA driver circuit.

A.1.2 Data acquisition

The Quanser MultiQ-PCI data acquisition system is used for data collection and interfacing with the software system. The MultiQ-PCI is used since it was readily available in the lab workspace and also it is straightforward to setup and use. The version of MATLAB has built-in support of the MultiQ-PCI, allowing a greater focus on algorithm design and less on interface coding. It provides 16 analog inputs (ADCs), 4 analog outputs (DACs), 48 digital I/O ports, and 6 encoder inputs [28]. In the current hardware setup 3 analog inputs, 1 analog output and 1 encoder input are used.

- **Analog inputs**: Each of the analog inputs takes input voltages in the range of ±10V and converts the signal to a signed 16-bit binary value (±32767) with a A/D conversion time of 23μs [28].

Of the three analog inputs used, one is for sensing the source voltage V_s, one is for differential voltage V_d and the remaining one is used for sensing the ambient air temperature, T_{amb}.

Even though the input voltages of the ADCs can be bipolar, in actuality only unipolar 0 ~ 10V signals are connected to the ADCs since (as will be shown later) single-supply op-amps are used to amplify V_d and V_s signals before they are connected to the ADCs. Additionally, the positive half of the resolution range is more than adequate for precise voltage sensing.

- **Analog Outputs**: The analog output channels on the MultiQ have a D/A resolution of 14 bits which outputs an analog voltage in the range of ±10V. The conversion time is 11µs. Since this output is used for a 5V PWM modulation signal, the D/A resolution is relatively unimportant, although the fast conversion time ensures the PWM timing is accurate.

- **Encoder Input**: The SMA wire strain encoder interfaces with the encoder input on the MultiQ via a standard 5-pin single-ended DIN connector. No specs on timing were given in [28], however since the encoder input is digital in nature, it is expected that the response speed will be as fast as, if not faster than the analog inputs.

A.1.2.1 Verification of ADC accuracy

In order to ensure data analysis give accurate results, the three ADCs on the MultiQ-PCI board used for feedback of V_d, V_s and T_{amb} are tested for accuracy. In this test, the "+" terminal of a DC voltage supply is connected to a buffer amplifier, then the output of the buffer amplifier is connected to the "+" terminal of each input ADC. MATLAB is setup to interface with the MultiQ board so the ADC reading of that input voltage can be obtained. The GND terminals of the power supply, the buffer amplifier and the ADC are connected to a common ground. The output voltage of the buffer amplifier is measured with a voltmeter. Using multiple DC voltages, each ADC's analog-to-digital conversion can be then calibrated

by comparing its reading with the measured voltages. The test results are presented in Table A.1.

Table A.1: Calibration of the ADCs on the MultiQ-PCI interface board

Analog-IN 1		Analog-IN 2		Analog-IN 3	
Measured Voltage	ADC reading	Measured Voltage	ADC reading	Measured Voltage	ADC reading
2.470V	2.493	2.446V	2.468	2.130V	2.148
3.259V	3.290	3.138V	3.162	2.926V	2.953
3.867V	3.901	3.946V	3.988	3.620V	3.658
4.610V	4.660	4.700V	4.754	4.520V	4.566
5.410V	5.465	5.450V	5.51	5.762V	5.824

It can be seen that in all three input channels, the voltage read by the ADC is slightly larger than the voltage measured by the voltmeter. For each of the three inputs, the ADC reading is about 1.01 times the actual applied voltage so in software a factor of 1/1.01 is multiplied to the analog inputs before any subsequent operations are carried out.

A.1.3 Signal amplification for V_d and V_s

Both V_d and V_s need to be sent to the computer via the data acquisition system so that the SMA resistance can be computed. V_d needs to be amplified first while V_s simply needs to be buffered before connection to the ADCs. Together the V_d amplification and V_s buffer circuit form the *signal amplification circuit*, implemented using the OP284F dual op-amp package. To minimize any effect that variations and disturbances in the SMA driver circuit has on signal amplification, the op-amp package is powered by a separate 12V supply from the SMA driver so that voltage variations due to R_s load changes in the Wheatstone bridge circuit do not affect the op-amps. The requirements for the power supplies for these op-amps are also less stringent, since a) a fast transition time is not required for powering these op-amps as they are not being pulse-width modulated, and b) the op-amps consume very little power.

For this purpose, the +12V power supply which came with the Proto-Board 204 breadboard package is used to power the op-amp chip package. The OP284F op-amp package is used with a single supply (i.e. +12V/GND) to reflect the condition that +12V/-12V dual supply may not always be available in practical applications. As noted in Subsection A.1.2, this also implies that only the positive half of the ±10V input range of the ADCs are used.

A.1.3.1 Amplifying V_d

A differential amplifier is used to amplify the differential voltage V_d since the measurement nodes for V_d in the bridge configuration are readily compatible with a differential amplifier.

A high gain is needed to amplify V_d to a voltage suitable for the 0 ~ 10V input range of the ADC. Assuming a nominal source voltage of V_s =12V, an SMA resistance range of 4.5Ω to 6.5Ω, and nominal R_o, R_{om} and R_{sm} resistances as listed in Subsection A.1.1.2, the variation of V_d would be nominally in the range of 8.01mV to 37.6mV. An amplifier gain of 266 V/V would allow the *amplified* V_d to be in the range of 2.13V to 10V. Since it is possible that in implementation the V_d range may be higher than the nominal range due to imprecise resistor choices, a lower gain of 220 V/V is chosen for the differential amplifier so that the amplified V_d does not exceed the input range of the ADC. Figure A.4 shows the simulated range of V_d and *amplified* V_d values (with a designed gain of 220 V/V) for an SMA resistance range of 4.5Ω to 6.5Ω.

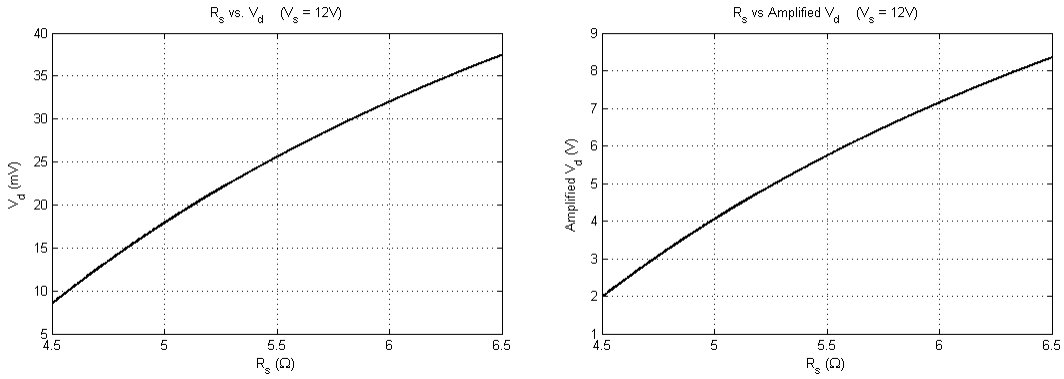

Figure A.4: The nominal mapping from SMA resistance to V_d and the amplification of Vd. Left: the R_s to V_d function. Right: the Rs to amplified V_d function. Both plots are generated from a simulation of the Wheatstone bridge and differential amplifier circuits, using the nominal resistance values.

During testing, five resistances (4.5Ω, 5Ω, 5.5Ω, 6Ω and 6.5Ω) were used as R_s to validate the design of the differential amplifier, and it was observed that when the source voltage is 12V the differential amplifier (for V_d) outputted a consistently low voltage regardless of the value of R_s (around 0.2V to 0.6V). It is hypothesized that the erroneous output is due to a high common-mode voltage in the inputs of the differential amplifier. For V_s = 12V, two nodes in the Wheatstone bridge for V_d measurement have a common-mode voltage of around 11.9V, which is very close to the op-amp's +12V rail voltage. In the OP284F data it is specified that for an op-amp rail voltage of 15V, the common-mode voltage should be below 14V for the op-amp to operate in its linear gain region [29]. While the op-amp rail voltage here is 12V and not 15V, the op-amp may still be liable to the same kind of non-linear behaviour when the common-mode voltage is very close to the rail voltage. To test this hypothesis, V_s was adjusted to 10.5V and it was seen that the *amplified* V_d signal now follows the positively correlated trend as shown in Figure A.4. Therefore, for all experiments and testing performed in this research, the supply voltage of the SMA driver circuit is set to 10.5V.

In the unlikely case that the SMA wire breaks, R_s would have a nearly infinite resistance. If this is the case then the *amplified* V_d signal would swing to the +12V rail voltage of the differential op-amp, exceeding the 10V maximum voltage value of the ADC. As a fail-safe measure, the *amplified* V_d signal is scaled down using a voltage divider built using a 470Ω and a 1.8kΩ resistor. The voltage divider has a scaling ratio of (1.8kΩ) / (1.8kΩ +470Ω) = 0.793, reducing a 12V voltage signal to 9.52V, which is now within the range of admissible ADC input voltages.

Figure A.5 shows the circuit diagram for the V_d amplification circuit.

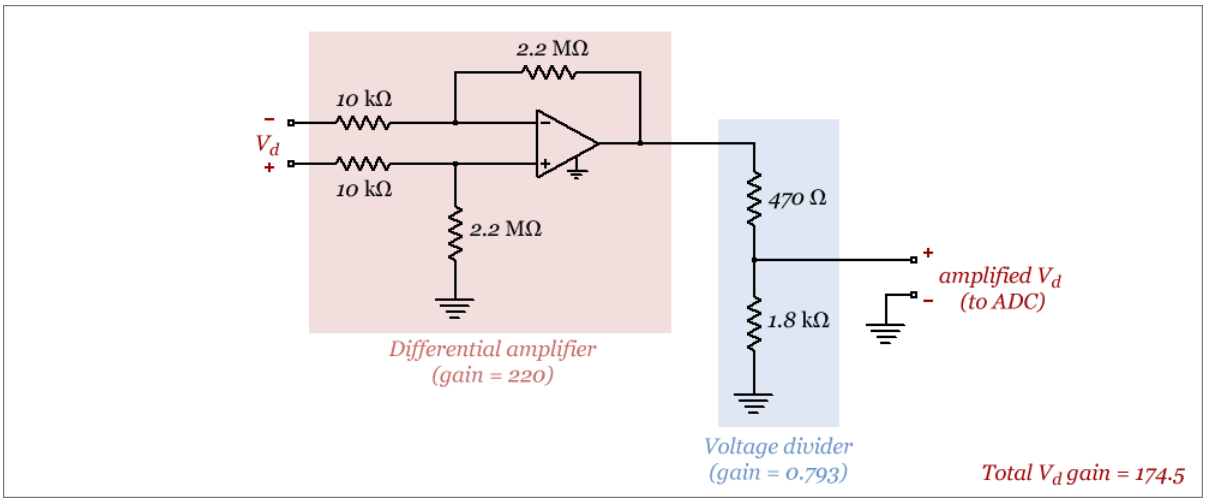

Figure A.5: V_d amplification circuit.

A.1.3.2 Amplifying V_s

The source voltage V_s is also sent to the computer via an ADC on the interface board. Unlike V_d, V_s does not need to be amplified when it is sent to the ADC; on the contrary, it needs to be scaled down since V_s is expected to be around 10V during operation. As illustrated in Figure A.6, the signal amplification circuit for V_s consists of a voltage divider and a buffer amplifier. First, the voltage divider scales V_s to half its value, then that voltage is connected to the input of buffer amplifier, and finally the output of the buffer amplifier is connected to

the "+" terminal of the ADC. Finally, in software the original source voltage is calculated by inverting the voltage divider gain.

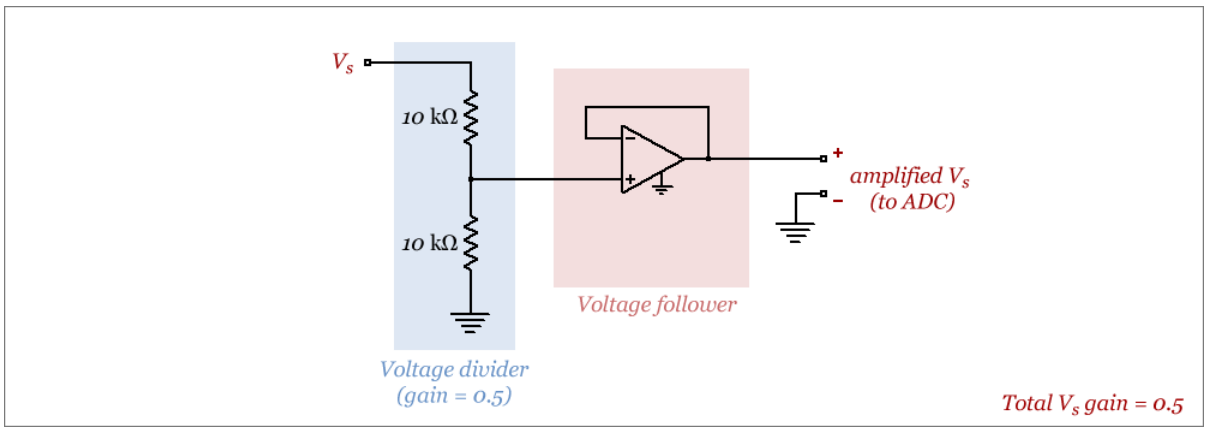

Figure A.6: V_s amplification circuit.

A.1.4 Other feedback signals

A.1.4.1 SMA wire strain

A US Digital H5S-1024 shaft encoder is connected to the computer through a digital encoder input on the interface board to provide experimental feedback of the SMA wire strain. The quadrature encoder does not measure the absolute strain of the SMA wire, which means it can only measure the change in wire length during a single experimental trial. The *encoder displacement gain*, i.e. the scaling factor that converts the encoder reading to the length change of the SMA wire, is calculated by performing the following trial:

1. At room temperature, the duty cycle of the SMA driver is set to 0% for the first 10 seconds of the trial. During this time, the encoder reading is 0 (counts). The "position" of the load cage attached to the SMA wire is marked with a knot on the high-strength wire that connects the load with the SMA wire. A photograph of the knot position is taken.

2. The duty cycle is then set to 20% for the next 60 seconds and the SMA is allowed to actuate and reach a steady state strain.

3. At the end of that 60s actuation period, the encoder count reading is recorded and another photograph of the knot position is taken. By comparing the two photos, the physical displacement of the knot caused by SMA wire contraction is determined. The ratio between the encoder reading and the knot displacement is the *encoder displacement gain*.

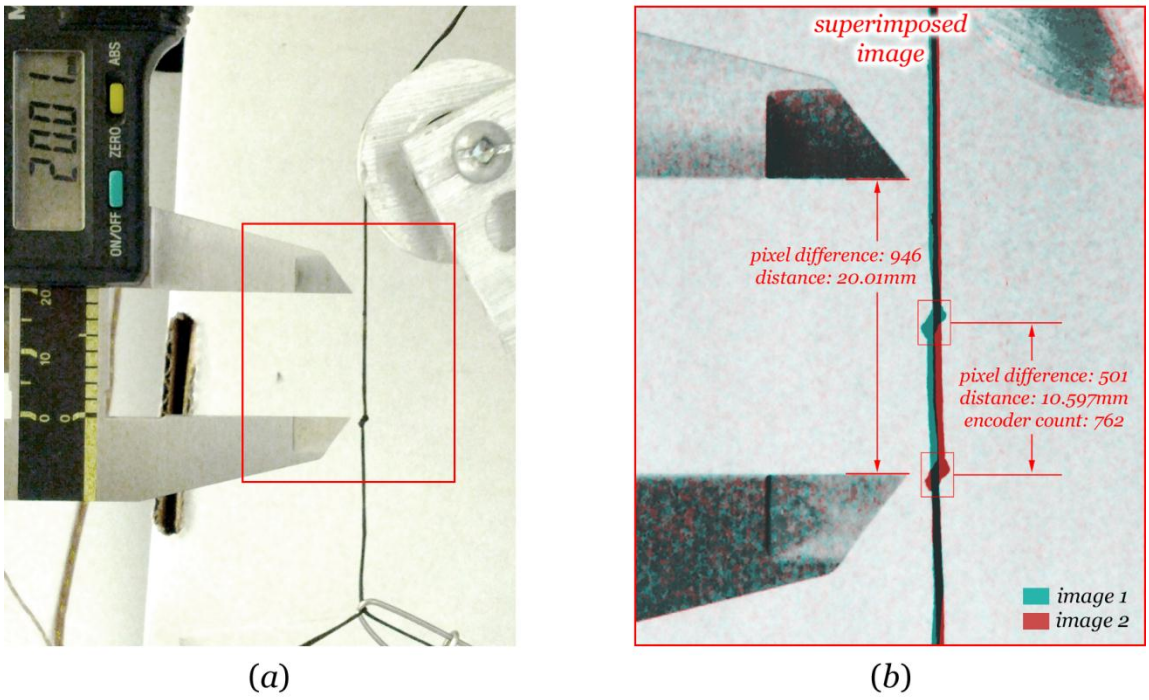

Figure A.7: Measurement of SMA wire length change and determination of the encoder gain. (a) A digital caliper set to 20.01mm is placed parallel to the high-strength wire that connects the load and the SMA wire. (b) The photographs taken before and after actuation are superimposed to allow the displacement caused by SMA wire contraction to be measured.

As shown in Figure A.7a, to ensure the accurate determination of the knot displacement, a digital caliper is placed next to the high-strength wire as a displacement reference in the photographs. The caliper is positioned parallel to the high-strength wire, and to prevent perspective distortion errors, the caliper is also positioned in the same plane as the high-strength wire perpendicular to the camera, so that they are at the same viewing distance. The

jaws of the caliper are used to align the before- and after-actuation photographs, which are superimposed as shown in Figure A.7b to determine the knot's vertical displacement.

Figure A.7b shows that the displacement of the knot as a result of SMA wire contraction was photographically measured to be 10.597mm, while the encoder reading is 762 counts. The *encoder displacement gain* was consequently calculated to be 72 counts/mm.

A.1.4.2 Ambient air temperature

As described in Section 4.1, feedback of the ambient temperature is provided using a K-type thermocouple. The thermocouple is connected to a NEWPORT® iDRN-TC/N Thermocouple Signal Conditioner / Transmitter in order to convert the thermocouple reading to a voltage signal compatible with the MultiQ-PCI analog input. The analog output of the NEWPORT® signal conditioner can be programmed to produce an output voltage that is a linear function of the thermocouple measurement using a NEWPORT® Thermocouple Conditioner programming application. The conversion function is specified using two temperature-voltage data pairs, as shown in Table A.2.

Table A.2: NEWPORT® Thermocouple Signal Conditioner scaling

Temperature, T_{amb}	Output Voltage, V_{Tamb}
-40°C	0V
160°C	5V

Using these two points, the signal conditioner's temperature-to-voltage function can be derived according to (A.3):

$$V_{Tamb} = (T_{amb} + 40°C) \cdot \frac{1}{40} V/°C \tag{A.3}$$

In software, the inverse relationship of (A.3) is used to recover the ambient temperature measurement.

A.2 Software design

The software for controlling, driving, collecting data from the experiment and processing that data is designed to be self-contained in the MATLAB/Simulink environment. Some advantages of using MATLAB are:

1. There are many data processing and analysis tools available in MATLAB, such as curve fitting, signal generation and plotting tools. Implementing the software in MATLAB allows a seamless integration of data acquisition and processing.

2. Simulink is a very intuitive way to build control systems and allows not only a graphical programming paradigm, but also the ability to embed custom code (which compiles to C-code) for implementing algorithms. It is also very useful for building simulations where "virtual" testing of control algorithms is desirable before testing on the experimental setup.

3. Hardware interfacing with the MultiQ board is handled automatically by Simulink.

While MATLAB/Simulink is useful for algorithm design, a limitation is that the algorithms designed in MATLAB will not be directly transferable to a microprocessor. This limitation, however, is ameliorated to some degree by the fact that the Simulink program is converted to C-code by MATLAB, which is then compiled and built into an executable file in order to perform the experiments and collect data in real-time, so the C-code can be re-used for compiling for a microcontroller target. Another disadvantage of using MATLAB/Simulink vs. a microcontroller is the fact that there is a high operating system overheat when using MATLAB/Simulink on a PC (as the MATLAB software was running on a Windows 2000 computer), which would not be present on a microcontroller.

The software system (which will be called *the software* from here on) implemented in Simulink is essentially a digital control system. Through trial and error, the minimum sampling time which can be achieved in Simulink is 0.2ms (or a sampling rate of 5000Hz). Due to processing speed limitations of the computer, any sampling period less than 0.2ms

causes instabilities in the computer system, resulting in irresponsiveness or sometimes the Blue-Screen-of-Death.

As shown in Figure A.8, the software can be divided into 3 subsystems, the *PWM driver*, *data processor*, and *controller*. The PWM driver subsystem is responsible for adjusting the heating power for the SMA wire based on the control signal generated by the controller; the data processor is responsible for calculating the resistance of the SMA wire, R_{sma}, and relaying feedback signals V_s, R_{sma} and T_{amb} to the controller; the controller is responsible for generating the control signal for "priming" and actuating the SMA wire.

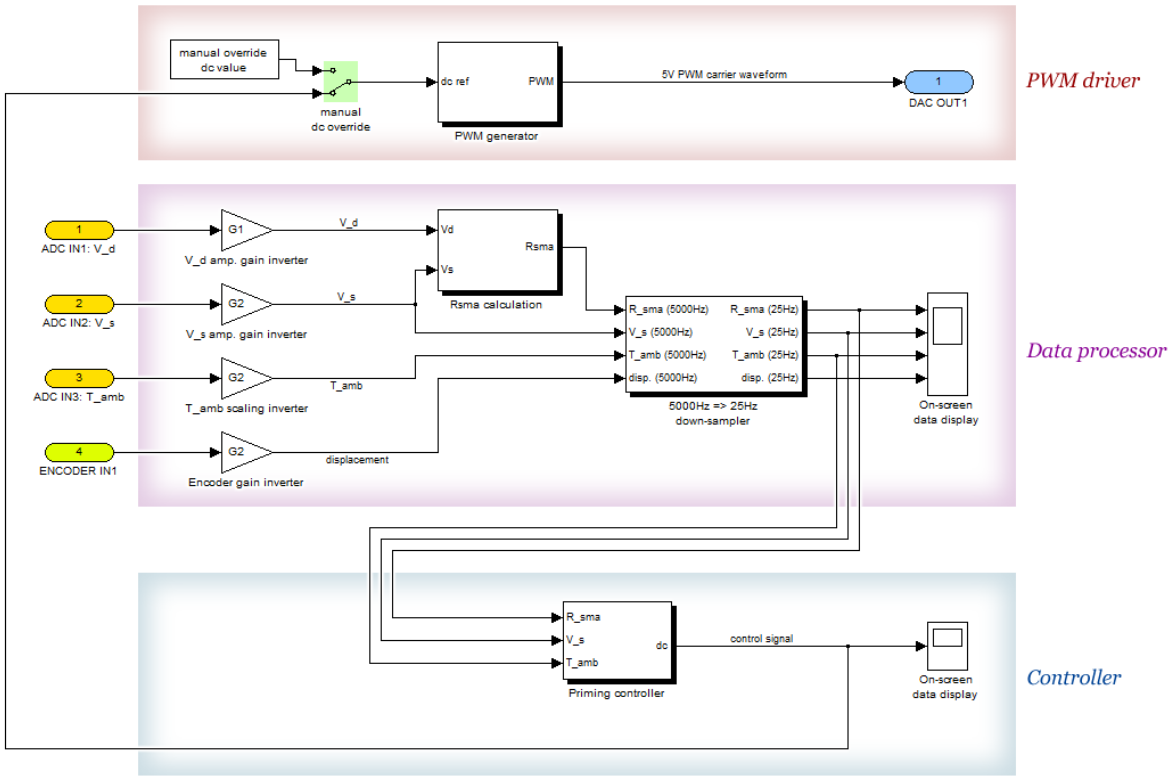

Figure A.8: Software system block diagram.

A.2.1 PWM driver

The PWM driver portion of the software is used to generate a PWM pulse waveform that is the carrier signal for modulating the current that powers the SMA wire. The output of the PWM driver system (i.e. the PWM waveform) is connected to one of the analog outputs on the MultiQ-PCI board, and drives the gate terminal on the MOSFET in the SMA driver circuit. The input to the PWM driver is the reference PWM duty cycle dc_{ref}, a value ranging between 0% and 100% that indicates the fraction of a single PWM cycle in which the output should be "ON". dc_{ref} is the control signal generated by the Controller subsystem, however during testing, it may also be overridden with a manually specified value.

Since the duty cycle of a PWM signal is a measure of the time duration that an "ON" signal is produced, the actual duty cycle of the generated waveform, dc, may be different from dc_{ref} due to the fact that the 0.2ms sampling period of the software limits the resolution of "ON" time that can be achieved. The potential negative effects of the quantization error in the duty cycle are minimized by setting the PWM frequency to be a lot lower than the fundamental frequency of the software, as well as by using a dithering algorithm that will be explained in greater detail later in this subsection.

The parameters of the PWM driver are:

- **PWM frequency:** this is the frequency of the PWM waveform. To allow refined control of the duty cycle, the PWM frequency should be set much lower than the fundamental frequency of the Simulink software environment. In the controller design of this research, the minimum duty cycle resolution is chosen to be 0.5%, and with the fundamental sampling period of the Simulink system being 0.2ms, the PWM frequency is set to 25Hz (or a PWM period of 0.04s). A higher PWM frequency can be set, however the duty cycle resolution would deteriorate as a result. Finally, the PWM frequency is also the rate at which the controller portion of the software is run.

- **PWM pulse magnitude:** Set at 5V to match with the "ON" voltage of the MOSFET. The "OFF" voltage is set to 0V.

- **End Time:** the time at which the power to the SMA wire is shut off. dc_{ref} is set to 0% when End Time is reached regardless of the control signal generated by the Controller subsystem.

The PWM carrier waveform is generated by comparing a saw tooth waveform with the reference duty cycle dc_{ref}. The saw tooth wave is set to ramp from 0 to 100% at the PWM frequency; the comparator function outputs a 1 if the saw tooth function is less than dc_{ref} and a 0 if the saw tooth function is greater. The output of the comparator is multiplied with the PWM pulse magnitude then sent to the MultiQ-PCI's analog output.

As mentioned previously, a potential issue with the sawtooth comparison method of generating the PWM waveform is that the actual duty cycle of the PWM carrier wave, dc, may not be the same as dc_{ref} due to the 0.5% minimum resolution of dc. As shown in the bottom plot in Figure A.9, the duty cycle of the PWM waveform is quantized to the nearest 0.5% interval less than or equal to dc_{ref}. As will be explained later in this thesis, dc_{ref} is fed-back internally in the Controller to predict the heating power of the SMA wire, so it is important that the physical heating power matches the predicted value. To correct this problem, a simple heuristic algorithm is implemented in the PWM Driver subsystem where the duration of the "ON" part of a PWM cycle is adjusted so that the equivalent dc switches between the nearest 0.5% intervals to dc_{ref}, as shown in in the top plot in Figure A.9. When averaged out over a larger time frame, the duty cycle of the generated PWM waveform matches dc_{ref}. This "dithering" algorithm is implemented by adding a random number between (and excluding) 0 to 0.5% to dc_{ref} prior to comparing it to the sawtooth function.

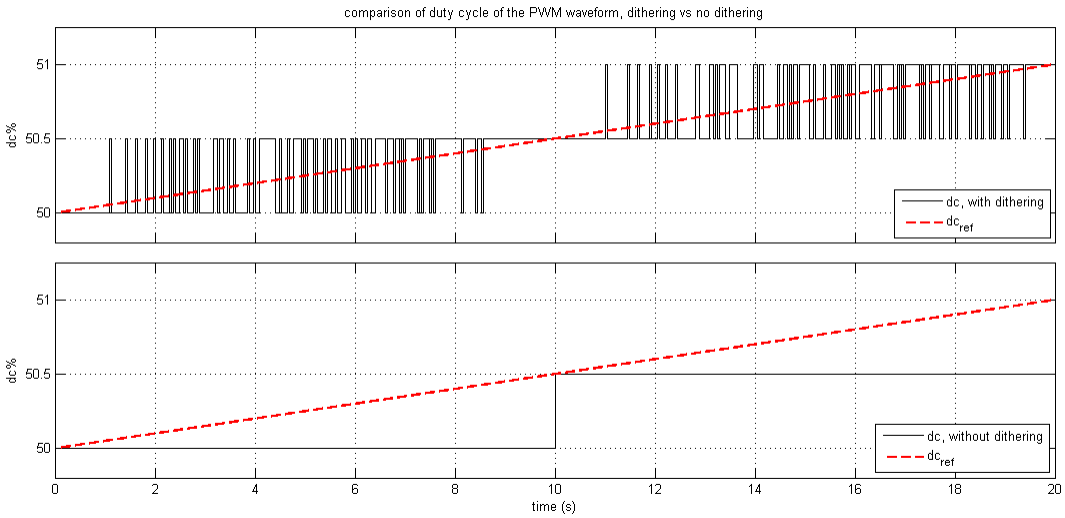

Figure A.9: Comparison of *dc* and dc_{ref} with and without the dithering algorithm.Top: With dithering. Bottom: Without dithering.

A.2.2 Data processor

The Data Processor subsystem in the software is used to decode the inputs into useful data. The main tasks of the Data Processor are to compute the SMA resistance R_{sma} based on V_s and V_d inputs; calculate T_{amb} based on the ambient temperature input and calculate the SMA wire length change from the encoder input. Since the input data are sampled at 5000Hz (the fundamental sampling rate of the software) while the Controller subsystem operates at the PWM rate of 25Hz, the Data Processor also has the additional task of converting the sample rate of V_s, R_{sma} and T_{amb} data from 5000Hz to a slower 25 Hz.

A.2.2.1 SMA resistance

The V_s and V_d voltages measured through the analog inputs on the MultiQ board are fed into an SMA resistance calculation block in the Data Processor, which is implemented as an embedded code block in Simulink. The algorithm used to calculate the SMA resistance is fairly simple:

1. The voltages at inputs 1 & 2 in Figure A.8 are amplified versions of the V_d and V_s measurements respectively. The amplifier gains for these inputs are inverted so the "real" V_s and V_d values are known.

2. Equation (A.2) is used to solve for R_S using these voltages and known resistances of the other resistors:

$$R_S = \frac{R_O}{1 - \frac{R_{SM}}{R_{SM} + R_{OM}} - \frac{V_d}{V_S}} + 1.$$

Note that only the voltage measurements during the "ON" part of a PWM cycle are accurate for R_s calculation. During the "OFF" part, V_d would be 0V regardless of the value of R_s so it would be impossible to calculate R_s.

The above algorithm can be used to accurately deduce R_s only if all resistors in the SMA Driver circuit are exactly equal to their nominal resistances and if the op-amps operate ideally. Because of the resistors' manufacturing tolerances, their values are likely to differ from their nominal values. Furthermore, un-modelled op-amp dynamics may also be present. Thus, an experimental system identification approach is taken to determine the exact function for calculating R_s.

The experimental procedure is as follows:

1. The SMA is replaced with resistors with known values that span the range of possible SMA resistances. Five resistors were used in place of the SMA, at 4.5 Ω, 5 Ω, 5.5 Ω, 6 Ω, 6.5Ω.

2. For each resistor, a 10 second trial is run where the source voltage V_s is adjusted between 8V and 10.5V by manually adjusting a dial on the autotransformer. The PWM duty cycle is set to 50%, and V_d and V_s data during "ON" in each PWM cycle are recorded. Figure

A.10 is a sample illustration of recorded V_d and V_s data, for the 5Ω resistor. The "OFF" portions of the PWM cycles are truncated.

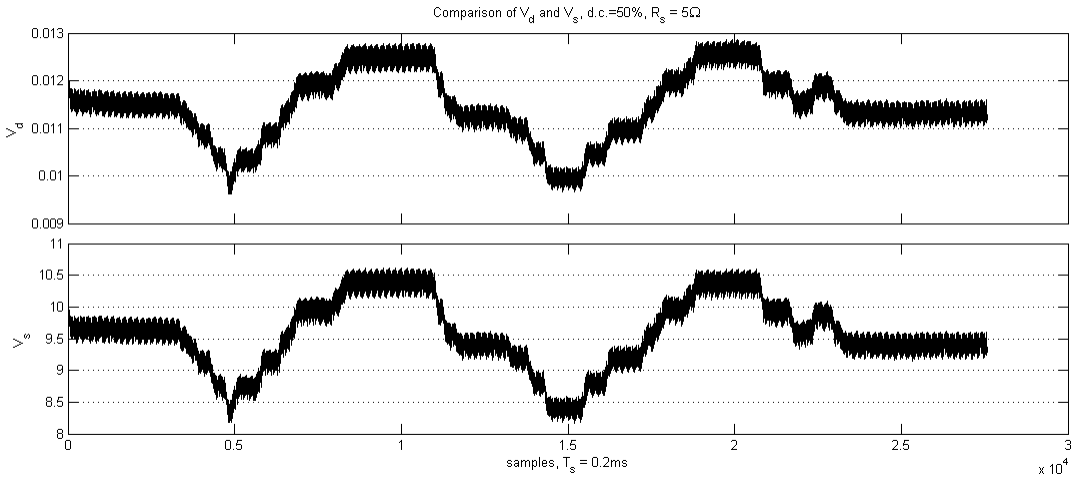

Figure A.10: Comparison of V_d and V_s. Note that the data for the "OFF" portion of each PWM cycle was discarded.

3. As shown in Figure A.11, the V_d and V_s data are plotted against each other for all five resistor trials and the respective V_d/V_s values are calculated using linear least-square estimation. This is done using the curve fitting tool in MATLAB.

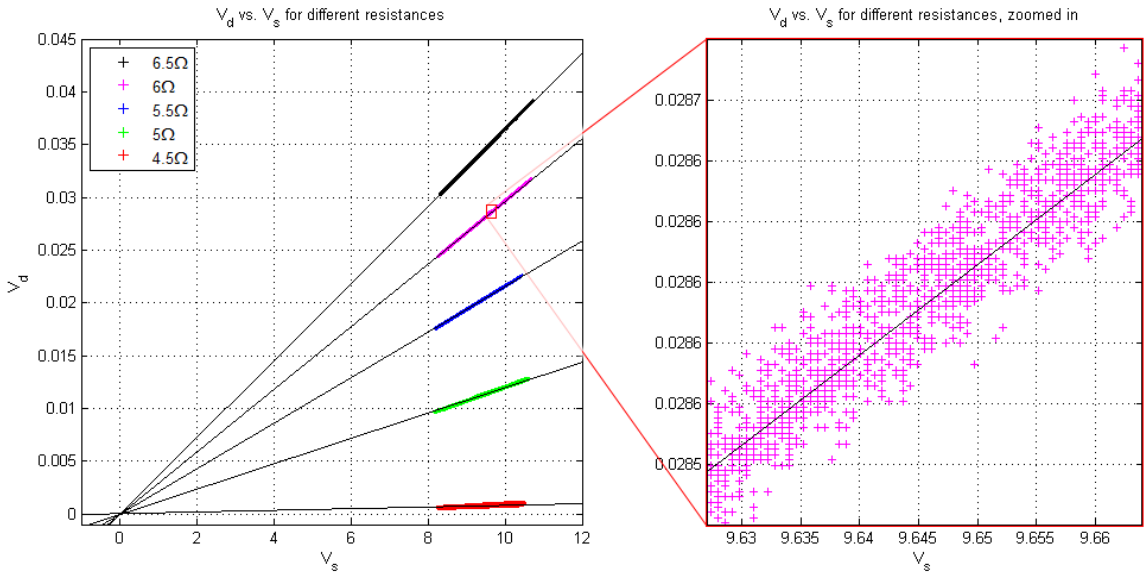

Figure A.11: V_d/V_s data-points and fitted linear functions for the five test resistances.

4. As shown in Figure A.12, the slope (V_d/V_s) of the five linear fits are plotted against their respective resistance values using the MATLAB curve fit tool and a function of the form below is fitted to the data points using the mean squares method.

$$R_s(V_d, V_s) = \frac{a}{1 - b - \frac{V_d}{V_s}} + 1 \tag{A.4}$$

where the nominal bridge resistance values form the nominal model parameters:

$$a = R_O, \quad b = \frac{R_{SM}}{R_{SM} + R_{OM}}.$$

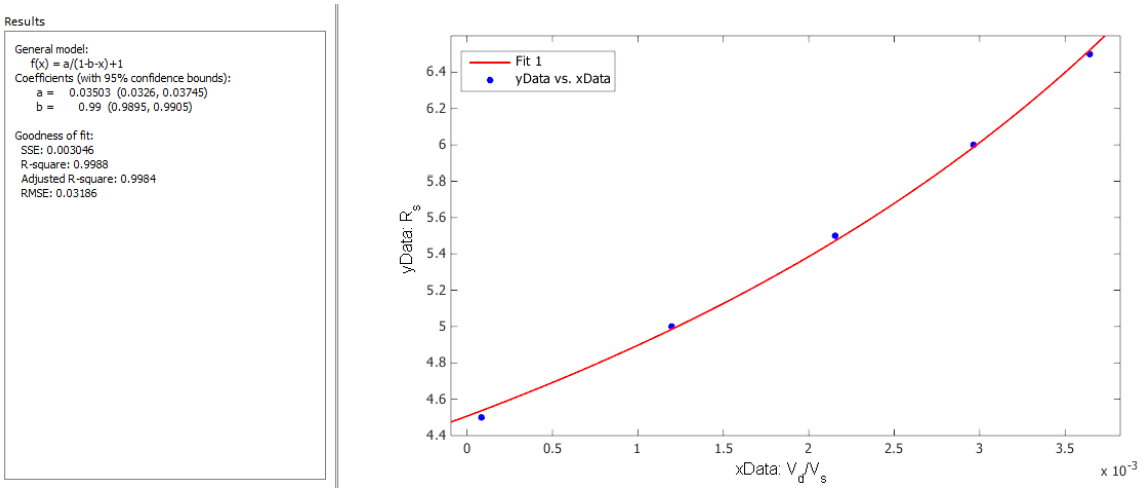

Figure A.12: Fitting R_s function using (A.4).

Through trial and error, it was discovered that using a 2nd order polynomial function of the form

$$R_S\left(\frac{V_d}{V_s}\right) = p_1\left(\frac{V_d}{V_s}\right)^2 + p_2\left(\frac{V_d}{V_s}\right) + p_3 \tag{A.5}$$

yielded a more accurate fit, despite the fact that the polynomial function does not have the same form as the derived model for calculating R_s. The polynomial curve fit result is shown in Figure A.13.

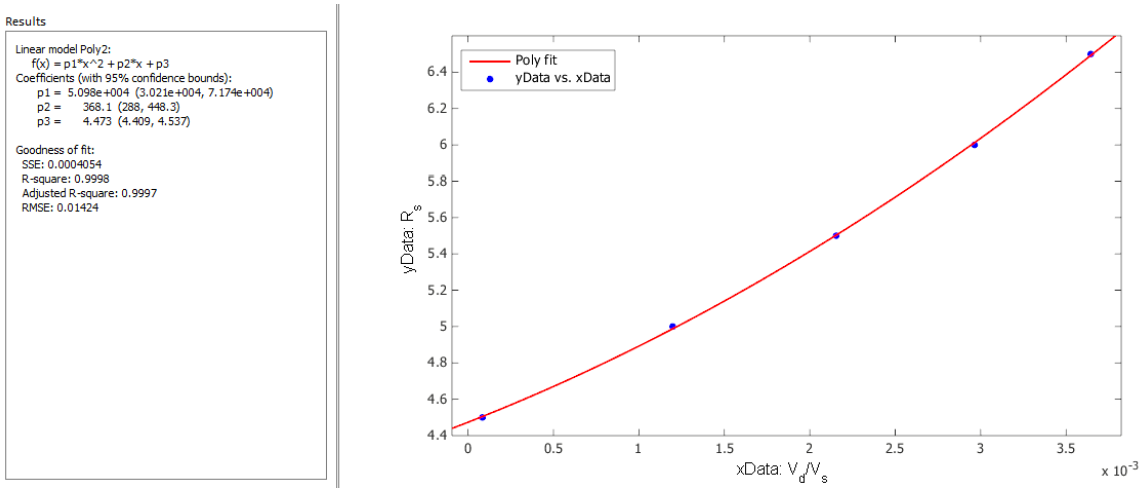

Figure A.13: Fitting R_s function using (A.5).

Due to differences between idealized and the physical amplifier circuit behaviours, it is hypothesized that (A.4) may no longer be an accurate representation of the function between V_d, V_s, and R_s. which may explain why fit using (A.5) produced a better fit, as shown in Figure A.13. Thus, the polynomial model (A.5) was chosen for calculating the SMA resistance instead of (A.4). In software, the parameters for calculating R_s based on (A.5) are:

$$R_S\left(\frac{V_d}{V_s}\right) = 50919.2\left(\frac{V_d}{V_s}\right)^2 + 368.1\left(\frac{V_d}{V_s}\right) + 4.4734 \tag{A.6}$$

A.2.2.2 SMA actuator displacement due to wire length change

The displacement gain of the rotary encoder was previously calculated to be 72 counts/mm, therefore in software, this gain was inverted to allow the displacement of the load attached to the SMA actuator as a result of the nitinol wire length change to be calculated, according to (A.7):

$$displacement(mm) = \frac{encoder\ count}{72}. \tag{A.7}$$

A.2.2.3 Ambient air temperature

In subsection A.1.4.2 the temperature-to-voltage conversion function of the NEWPORT® Thermocouple Signal Conditioner was calculated according to (A.3). In the *Data Processor* subsystem of the software, the original ambient temperature measurement is calculated by inverting the relationship in (A.3), i.e.

$$T_{amb} = -40°C + V_{Tamb} \cdot 40\ °C/V \tag{A.8}$$

A.2.2.4 Sample rate conversion from 5000Hz to 25Hz

Because the controller portion of the software is run at a rate of 25Hz (the "*slow rate*") compared to the fundamental sampling rate of 5000Hz for the entire software program (the "*fast rate*"), the fast rate data at the input ports of the entire Simulink model must be down-sampled before the data is compatible with the slow rate input ports of the controller subsystem. The controller subsystem takes V_s, R_{sma} and T_{amb} as inputs, so those three signals are subject to further data processing to reduce the data rate.

The first step in the sample rate conversion process is to discern accurate fast rate data samples from inaccurate samples. It's known that when the PWM Driver signal transitions from "OFF" to "ON" or vice-versa, the MOSFET and the opamps take some time to fully transition from one state to the next; therefore, the V_d and V_s measurements and the R_{sma} value calculated using V_s and V_d may not be accurate during this time. Figure A.14 shows the effect of this transient on the R_{sma} calculation, where a resistor with 6Ω nominal resistance was used as R_{sma} and the PWM is set to a duty cycle of 10%.

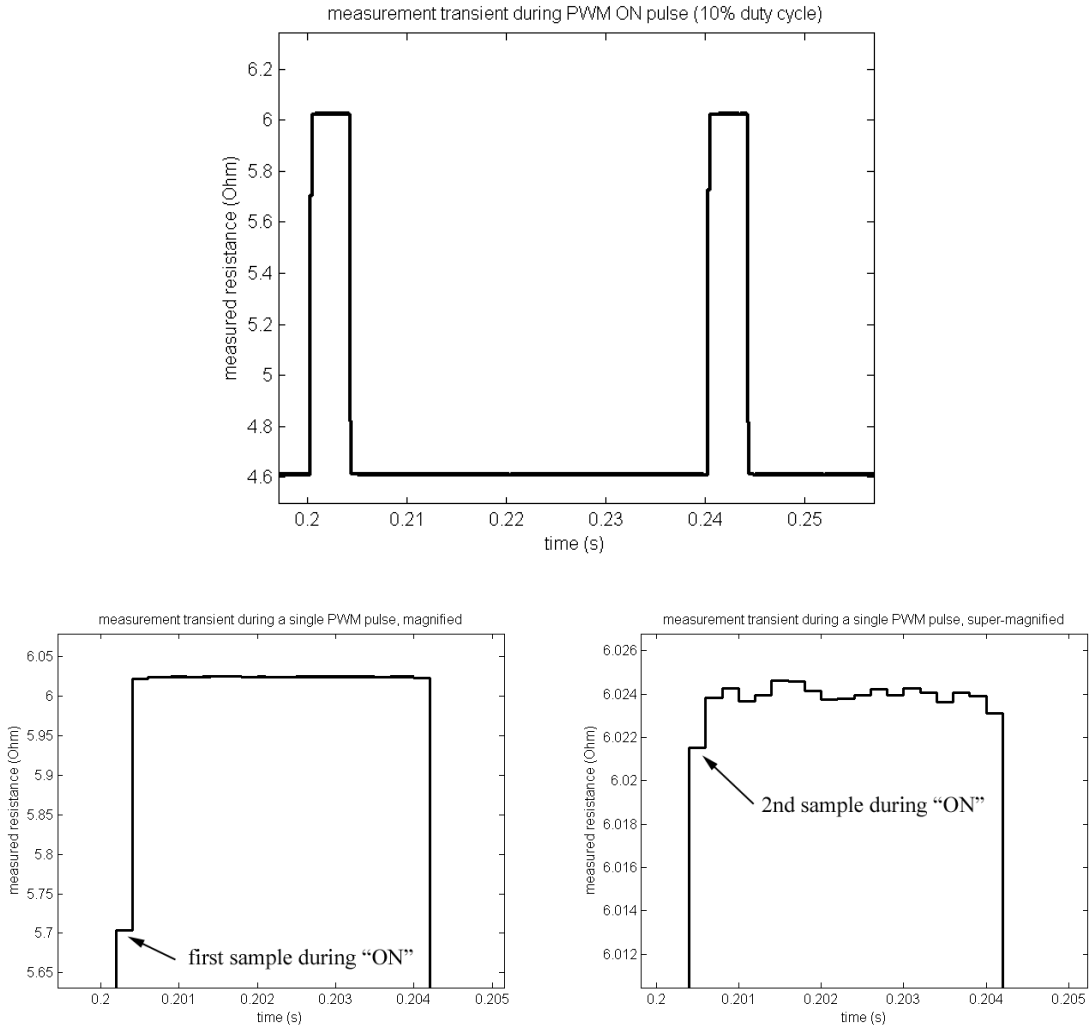

Figure A.14: PWM "ON" pulse transient behaviour. Top: Resistance measurement for two PWM pulses at 10% duty cycle is shown. Bottom left: the first pulse is magnified to show the initial transient. Bottom right: increased magnification of the same pulse shows that the measurement value is steady after about the 2nd sample during the pulse.

It can be seen that the transition transient greatly affects the first sample collected during the "ON" part of the PWM pulse, but after the first two data samples, the pulse seems to have reached steady state. To ensure that there is at least one accurate sample during data

collection, the minimum PWM duty cycle should be 1.5%, which is equivalent to 3 samples at 5000Hz. The first two samples during "ON" are therefore discarded.

The second step is to produce a single slow rate data sample using the remaining fast rate samples during the "ON" period of the pulse. From Figure A.14, it can be seen that at steady state there is still some noise in the data collected during the "ON" period, although the noise is very small compared to the data values themselves. As shown in Figure A.15, to produce the slow rate data for a single PWM cycle, an average of all fast rate data after the 2nd sample during "ON" is calculated. Specifically in the software, the rising edge of the PWM pulse triggers a delayed digital up counter (that runs at the fast rate) that counts up from zero after the first 2 samples, and it also triggers a summer that starts adding up all the sample values after the first 2 samples. The counter and the summer keep doing their respective tasks until the falling edge of the PWM is encountered, at which time the value of the summer is divided by the value of the counter to obtain an average value.

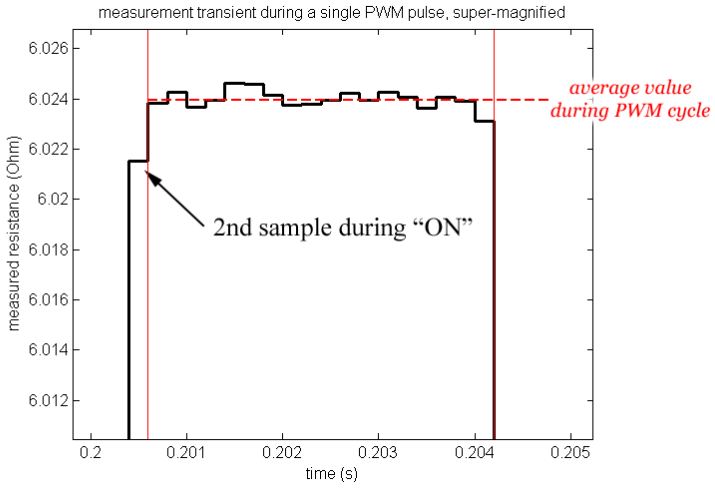

Figure A.15: The average value of measured data during the "ON" period of a PWM cycle is used as the slow rate data.

Because the clock for the high sample rate and the low sample rate are synchronized at the start of each PWM cycle, the controller, which operates at the slow rate, will not be able to

access the calculated average value until the subsequent PWM cycle, so the average value is copied to a temporary variable which is received by the controller at the start of the next PWM cycle. The values in the counter and summer are reset to zero so they will be ready for the next PWM cycle. An unavoidable side effect of this algorithm is that the data received at the overall Simulink model's input ports can be delayed by up to one slow rate sampling period (40ms) before it is received by the controller.

Both the measured V_s and calculated R_{sma} signals are conditioned this way when their values are sent to the controller subsystem. For consistency, since the controller also takes the ambient temperature measurement as an input, T_{amb} sampled at 5000Hz is also processed in an identical manner.

A.2.3 Controller

The controller portion of the software runs at the slow rate of 25Hz, same frequency as the PWM generator. Compared to the fundamental sampling rate of 5000Hz, this slower rate allows the controller algorithm to be easily executed in real time given the computational limitations of the computer, and reduces the memory needed for data logging.

The controller is implemented as a subsystem block in Simulink. The design of the controller block is presented in detail in Chapter 6.

Appendix B

Copyright permissions

B.1 Permission letter for: Figure A.1

Date: Tue, 4 Sep 2012 09:23:17 -0400 [09/04/12 09:23:17 EDT]
From: Mohamed El Deeb <m.aldeeb@gmail.com>
To: Hunter Song <zhsong@uwaterloo.ca>
Cc: Rob Gorbet <rbgorbet@uwaterloo.ca>
Subject: Re: Permission request for reproduction of Figures from your thesis.

Hi Hunter,

I apologize for the late reply. I grant you permission to use the reference below as a citation.

Regards,
Mohamed

On Tue, Aug 28, 2012 at 2:37 PM, Hunter Song <zhsong@uwaterloo.ca> wrote:

> Hi Mohamed, thanks again for agreeing to allow me to use a figure from your thesis. for the record, please send me a reply to the following permission request letter.
>
> **********
> Aug. 28, 2012
>
> To Mohamed El Dib:
>
> I am preparing a thesis entitled "Design of a Robust Priming Controller for SMA Actuators" ("the Work") for the Masters of Applied Science program at the University of Waterloo, Waterloo, ON, Canada.
>
> I would appreciate permission to reproduce the following item(s) in both print and electronic editions of the thesis and any derivative products. Unless you indicate otherwise, I will use the complete reference given below as the citation.
>
> 1. Figure 5.6, "SMA Actuator Priming Using Resistance Feedback," M. El Dib, Master's Thesis, University of Waterloo, University of Waterloo, 2010
>
> Thank you for your prompt attention to this request.
>
> **********
>
> Yours sincerely
>
> Zihao Hunter Song

B.2 Permission letter for Figure 5.1

Date: Wed, 29 Aug 2012 12:31:54 -0500 [08/29/12 13:31:54 EDT]
From: Song, Gangbing <GSong@Central.UH.EDU>
To: Hunter Song <zhsong@uwaterloo.ca>
Cc: gsong@uh.edu <gsong@uh.edu>
Subject: Re: Permission to reproduce

You have my permission

G Song

On Aug 30, 2012, at 1:11 AM, "Hunter Song" <zhsong@uwaterloo.ca> wrote:

> Aug. 29, 2012
>
> Dear Dr. Song:
>
> I am preparing a thesis entitled ?Design of a Robust Priming Controller for SMA Actuators? (?the Work?) for the Masters of Applied Science program at the University of Waterloo, Waterloo, ON, Canada.
>
> I would appreciate permission to reproduce the following item(s) in both print and electronic editions of the thesis and any derivative products.Unless you indicate otherwise, I will use the complete reference given below as the credit line. I've already been granted license by IOP publishing , the organization responsible for making the requested material available.
>
> 1. Figure 6, ?Position control of shape memory alloy actuators with internal electrical resistance feedback using neural networks?, N. Ma, G. Song, H-J. Lee, Smart Mater. Struct. 13 (2004) 777?783.
>
> I have attached the permission letter from IOP Publishing, for your records.
>
> Thank you for your prompt attention to this request.
>
> Yours sincerely
>
> Zihao Hunter Song
> University of Waterloo
>
> ---------- Forwarded message ----------
> From: **Hunter Song** <zhsong@uwaterloo.ca>
> Date: Wed, Aug 29, 2012 at 11:46 AM
> Subject: Re: Permission to reproduce
> To: Permissions <permissions@iop.org>
>
> Thank you Sarah, for your prompt reply!
>
> Zihao Hunter Song
>
> On Aug 29, 2012 5:47 AM, "Permissions" <permissions@iop.org> wrote:
>> Dear Dr Song
>>
>> Please find attached the permission to reproduce material from an IOPP publication.
>>
>> Please acknowledge receipt of this email.
>>
>> Best wishes
>>
>> Sarah Ryder
>>
>> Publishing Administrator
>> Email: permissions@iop.org
>>
>> ---
>>
>> This email (and attachments) are confidential and intended for the addressee(s) only. If you are not the intended recipient please notify the sender, delete any copies and do not take action in reliance on it. Any views expressed are the author's and do not represent those of IOP, except where specifically stated. IOP takes reasonable precautions to protect against viruses but accepts no responsibility for loss or damage arising from virus infection. For the protection of IOP's systems and staff emails are scanned automatically.
>>
>> **IOP Publishing Limited** Registered in England under Registration No 467514. Registered Office: Temple Circus, Bristol BS1 6HG England Vat No GB 461 6000 84.
>>
>> **Please consider the environment before printing this email**
>>
>> ---
>
> <Permissions Song 29 08.pdf>

To: permissions@iop.org,
Cc:
Bcc:
Subject: Permission request to reproduce figure(s) from the Smart Materials and Structures Journal
From: Hunter Song <zhsong@uwaterloo.ca> - Tuesday 28/08/2012 19:26
Sent by: zhsong.uw@gmail.com

Aug. 28, 2012

To whom it may concern:

I am preparing a thesis entitled "Design of a Robust Priming Controller for SMA Actuators" ("the Work") for the Masters of Applied Science program at the University of Waterloo, Waterloo, ON, Canada.

I would appreciate permission to reproduce the following item(s) in both print and electronic editions of the thesis and any derivative products. I should be grateful for nonexclusive perpetual world rights in all languages and media. Unless you indicate otherwise, I will use the complete reference given below as the credit line. In case you do not control these rights, I would appreciate it if you could let me know to whom I should apply for permissions.

1. Figure 6, "Position control of shape memory alloy actuators with internal electrical resistance feedback using neural networks", N. Ma, G. Song, H-J. Lee, Smart Mater. Struct. 13 (2004) 777–783.

For your convenience a copy of this letter may serve as a release form: the duplicate copy may be retained for your files.

Thank you for your prompt attention to this request.

Yours sincerely

Zihao Hunter Song
University of Waterloo

PERMISSION TO REPRODUCE AS REQUESTED IS GIVEN PROVIDED THAT:

(a) the consent of the author(s) is obtained
(b) the source of the material including author, title of article, title of journal, volume number, issue number (if relevant), page range (or first page if this is the only information available), date and publisher is acknowledged.
(c) for material being published electronically, a link back to the original article should be provided (via DOI).

IOP Publishing Ltd
Temple Circus
Temple Way
BRISTOL
BS1 6BE

29/08/2012
Date

Sarah Hale
Rights & Permissions

B.3 Permission letter for Figure 5.7

ELSEVIER LICENSE

TERMS AND CONDITIONS

Sep 12, 2012

This is a License Agreement between Zihao Hunter Song ("You") and Elsevier ("Elsevier") provided by Copyright Clearance Center ("CCC"). The license consists of your order details, the terms and conditions provided by Elsevier, and the payment terms and conditions.

Supplier	Elsevier Limited
	The Boulevard,Langford Lane
	Kidlington,Oxford,OX5 1GB,UK
Registered Company Number	1982084
Customer name	Zihao Hunter Song
Customer address	802-32 Clegg Rd
	Markham, ON L6G0B2
License number	2.97323E+12
License date	20-Aug-12
Licensed content publisher	Elsevier
Licensed content publication	Materials Science and Engineering: A
Licensed content title	Electric resistance variation of NiTi shape memory alloy wires in thermomechanical tests: Experiments and simulation
Licensed content author	V. Novák,P. Šittner,G.N. Dayananda,F.M. Braz-Fernandes,K.K. Mahesh
Licensed content date	25-May-08
Licensed content volume number	481–482
Licensed content issue number	
Number of pages	7
Start Page	127
End Page	133
Type of Use	reuse in a thesis/dissertation
Portion	figures/tables/illustrations
Number of figures/tables/illustrations	1
Format	both print and electronic
Are you the author of this Elsevier article?	No
Will you be translating?	No
Order reference number	
Title of your thesis/dissertation	Design of a Robust Priming Controller for SMA Actuators
Expected completion date	Sep-12
Estimated size (number of pages)	170
Elsevier VAT number	GB 494 6272 12
Permissions price	0.00 USD
VAT/Local Sales Tax	0.0 USD / 0.0 GBP
Total	0.00 USD
Terms and Conditions	

INTRODUCTION

1. The publisher for this copyrighted material is Elsevier. By clicking "accept" in connection with completing this licensing transaction, you agree that the following terms and conditions apply to this transaction (along with the Billing and Payment terms and conditions established by Copyright Clearance Center, Inc. ("CCC"), at the time that you opened your Rightslink account and that are available at

any time at http://myaccount.copyright.com).

GENERAL TERMS

2. Elsevier hereby grants you permission to reproduce the aforementioned material subject to the terms and conditions indicated.

3. Acknowledgement: If any part of the material to be used (for example, figures) has appeared in our publication with credit or acknowledgement to another source, permission must also be sought from that source. If such permission is not obtained then that material may not be included in your publication/copies. Suitable acknowledgement to the source must be made, either as a footnote or in a reference list at the end of your publication, as follows:

"Reprinted from Publication title, Vol /edition number, Author(s), Title of article / title of chapter, Pages No., Copyright (Year), with permission from Elsevier [OR APPLICABLE SOCIETY COPYRIGHT OWNER]." Also Lancet special credit - "Reprinted from The Lancet, Vol. number, Author(s), Title of article, Pages No., Copyright (Year), with permission from Elsevier."

4. Reproduction of this material is confined to the purpose and/or media for which permission is hereby given.

5. Altering/Modifying Material: Not Permitted. However figures and illustrations may be altered/adapted minimally to serve your work. Any other abbreviations, additions, deletions and/or any other alterations shall be made only with prior written authorization of Elsevier Ltd. (Please contact Elsevier at permissions@elsevier.com)

6. If the permission fee for the requested use of our material is waived in this instance, please be advised that your future requests for Elsevier materials may attract a fee.

7. Reservation of Rights: Publisher reserves all rights not specifically granted in the combination of (i) the license details provided by you and accepted in the course of this licensing transaction, (ii) these terms and conditions and (iii) CCC's Billing and Payment terms and conditions.

8. License Contingent Upon Payment: While you may exercise the rights licensed immediately upon issuance of the license at the end of the licensing process for the transaction, provided that you have disclosed complete and accurate details of your proposed use, no license is finally effective unless and until full payment is received from you (either by publisher or by CCC) as provided in CCC's Billing and Payment terms and conditions. If full payment is not received on a timely basis, then any license preliminarily granted shall be deemed automatically revoked and shall be void as if never granted. Further, in the event that you breach any of these terms and conditions or any of CCC's Billing and Payment terms and conditions, the license is automatically revoked and shall be void as if never granted. Use of materials as described in a revoked license, as well as any use of the materials beyond the scope of an unrevoked license, may constitute copyright infringement and publisher reserves the right to take any and all action to protect its copyright in the materials.

9. Warranties: Publisher makes no representations or warranties with respect to the licensed material.

10. Indemnity: You hereby indemnify and agree to hold harmless publisher and CCC, and their respective officers, directors, employees and agents, from and against any and all claims arising out of your use of the licensed material other than as specifically authorized pursuant to this license.

11. No Transfer of License: This license is personal to you and may not be sublicensed, assigned, or transferred by you to any other person without publisher's written permission.

12. No Amendment Except in Writing: This license may not be amended except in a writing signed by both parties (or, in the case of publisher, by CCC on publisher's behalf).

13. Objection to Contrary Terms: Publisher hereby objects to any terms contained in any purchase order, acknowledgment, check endorsement or other writing prepared by you, which terms are inconsistent with these terms and conditions or CCC's Billing and Payment terms and conditions. These terms and conditions, together with CCC's Billing and Payment terms and conditions (which are incorporated herein), comprise the entire agreement between you and publisher (and CCC) concerning this licensing transaction. In the event of any conflict between your obligations established by these terms and conditions and those established by CCC's Billing and Payment terms and conditions, these terms and conditions shall control.

14. Revocation: Elsevier or Copyright Clearance Center may deny the permissions described in this License at their sole discretion, for any reason or no reason, with a full refund payable to you. Notice of such denial will be made using the contact information provided by you. Failure to receive such notice will not alter or invalidate the denial. In no event will Elsevier or Copyright Clearance Center be responsible or liable for any costs, expenses or damage incurred by you as a result of a denial of your permission request, other than a refund of the amount(s) paid by you to Elsevier and/or Copyright Clearance Center for denied permissions.

LIMITED LICENSE

The following terms and conditions apply only to specific license types:

15. **Translation**: This permission is granted for non-exclusive world **English** rights only unless your license was granted for translation rights. If you licensed translation rights you may only translate this content into the languages you requested. A professional translator must perform all translations and reproduce the content word for word preserving the integrity of the article. If this license is to re-use 1 or 2 figures then permission is granted for non-exclusive world rights in all languages.

16. **Website**: The following terms and conditions apply to electronic reserve and author websites:
Electronic reserve: If licensed material is to be posted to website, the web site is to be password-protected and made available only to bona fide students registered on a relevant course if:
This license was made in connection with a course,
This permission is granted for 1 year only. You may obtain a license for future website posting,

All content posted to the web site must maintain the copyright information line on the bottom of each image,
A hyper-text must be included to the Homepage of the journal from which you are licensing at
http://www.sciencedirect.com/science/journal/xxxxx or the Elsevier homepage for books at http://www.elsevier.com , and
Central Storage: This license does not include permission for a scanned version of the material to be stored in a central repository such as that provided by Heron/XanEdu.

17. **Author website** for journals with the following additional clauses:

All content posted to the web site must maintain the copyright information line on the bottom of each image, and the permission granted is limited to the personal version of your paper. You are not allowed to download and post the published electronic version of your article (whether PDF or HTML, proof or final version), nor may you scan the printed edition to create an electronic version. A hyper-text must be included to the Homepage of the journal from which you are licensing at http://www.sciencedirect.com/science/journal/xxxxx . As part of our normal production process, you will receive an e-mail notice when your article appears on Elsevier's online service ScienceDirect (www.sciencedirect.com). That e-mail will include the article's Digital Object Identifier (DOI). This number provides the electronic link to the published article and should be included in the posting of your personal version. We ask that you wait until you receive this e-mail and have the DOI to do any posting.

Central Storage: This license does not include permission for a scanned version of the material to be stored in a central repository such as that provided by Heron/XanEdu.

18. **Author website** for books with the following additional clauses:
Authors are permitted to place a brief summary of their work online only.
A hyper-text must be included to the Elsevier homepage at http://www.elsevier.com . All content posted to the web site must maintain the copyright information line on the bottom of each image. You are not allowed to download and post the published electronic version of your chapter, nor may you scan the printed edition to create an electronic version.

Central Storage: This license does not include permission for a scanned version of the material to be stored in a central repository such as that provided by Heron/XanEdu.

19. **Website** (regular and for author): A hyper-text must be included to the Homepage of the journal from which you are licensing at http://www.sciencedirect.com/science/journal/xxxxx. or for books to the Elsevier homepage at http://www.elsevier.com

20. **Thesis/Dissertation**: If your license is for use in a thesis/dissertation your thesis may be submitted to your institution in either print or electronic form. Should your thesis be published commercially, please reapply for permission. These requirements include permission for the Library and Archives of Canada to supply single copies, on demand, of the complete thesis and include permission for UMI to supply single copies, on demand, of the complete thesis. Should your thesis be published commercially, please reapply for permission.

References

[1] K. Ikuta, "Micro/miniature Shape Memory Alloy Actuator," *Proc. 1990 IEEE International Conference on Robotics and Automation,* vol. 3, pp. 2156-2161, 1990.

[2] B. K. Alliston, A. M. Knebol and M. R. Salemi, "Method and Apparatus for Controlling a Shape Memory Alloy Fuel Injector". US Patent 6019113, 1 Feb 2000.

[3] K. Ikuta, "Shape Memory Alloy Servo Actuator System with Electric Resistance Feedback and Application for Active Endoscope," *Proc. 1988 IEEE International Conference on Robotics and Automation,* pp. 427-430, 1988.

[4] F. Calkins, J. H. Mabe and R. T. Ruggeri, "Overview of Boeing's Shape Memory Alloy Based Morphing Aerostructures," *ASME 2008 Conference on Smart Materials, Adaptive Structures and Intelligent Systems,* vol. 1, pp. 885-895, 2008.

[5] R. Featherstone and Y. H. Teh, "Improving the Speed of Shape Memory Alloy Actuators by Faster Electrical Heating," *Experimental Robotics IX, Springer Tracts in Advanced Robotics,* vol. 21, pp. 67-76, 2006.

[6] M. El Dib, R. Gorbet, E. Kubica, X. Gao, A. L. Browne and N. L. Johnson, "Adaptive SMA Actuator Priming Using Resistance Feedback," *Smart Materials and Structures,* vol. 20, no. 11, 2011.

[7] P. Sittner, V. Novak, P. Lukas and M. Landa, "Stress-Strain-Temperature Behavior Due to B2-R-B19' Transformation in NiTi Polycrystals," *Journal of Engineering Materials*

and Technology, vol. 128, pp. 268 - 278, 2006.

[8] D. Madill and D. Wang, "Modelling and L2-stability of a Shape Memory Alloy Position Control System," *IEEE Transactions on Control Systems Technology,* vol. 6, no. 4, pp. 473-481, 1998.

[9] K. Ikuta, M. Tsukamoto and S. Hirose, "Mathematical Model and Experimental Verification of Shape Memory Alloy for Designing Microactuator," *Proc. MEMS '91,* pp. 103-108, 1991.

[10] D. A. Johnson, "Eyeglass Frame". U.S. Patent 7441888, 28 Oct 2008.

[11] Dynalloy Inc., "Technical Characteristics of Flexinol Actuator Wires," [Online]. Available: http://dynalloy.com/pdfs/TCF1140.pdf. [Accessed July 2012].

[12] W. Huang, "On the Selection of Shape Memory Alloys for Actuators," *Materials & Design,* vol. 23, no. 1, pp. 11-19, 2002.

[13] R. A. Russell and R. B. Gorbet, "Improving the Response of SMA Actuators," *Proc.1995 IEEE International Conference on Robotics and Automation,* vol. 3, pp. 2299-2304, 1995.

[14] B. Selden, K. Cho and H. H. Asada, "Segmented Shape Memory Alloy Actuators Using Hysteresis Loop Control," *Smart Materials and Structures,* vol. 15, no. 2, pp. 642-652, 2006.

[15] O. K. Rediniotis, D. C. Lagoudas, H. Y. Jun and R. D. Allen, "Fuel-Powered Compact SMA Actuator," *Proc. Smart Structures and Materials 2002,* pp. 441-490, July 2002.

[16] F. Gil and J. Planell, "Thermal Effciencies of NiTiCu Shape Memory Alloys," *Thermochimica Acta,* vol. 327, no. 1-2, pp. 151-154, March 1999.

[17] S. Hirose, K. Ikuta and Y. Umetani, "Development of Shape Memory Alloy Actuators: Performance Assessment and Introduction of a New Composing Approach," *Advanced Robotics,* vol. 3, no. 1, pp. 3-16, 1988.

[18] G. Song, B. Kelly and B. N. Agrawal, "Active Position Control of a Shape Memory Alloy Wire Actuated Composite Beam," *Smart Material Structures,* pp. 711-716, 2000.

[19] S. B. Choi, Y. M. Han, J. H. Kim and C. C. Cheong, "Force Tracking Control of a Flexible Gripper Featuring Shape Memory Alloy Actuators," *Mechatronics,* vol. 11, no. 6, pp. 677-690, 2001.

[20] J. Harrison, "Measurable Change Concomitant with SME Transformation," in *Engineering Aspects of SMAs,* London, Butterworth- Heinemann, 1990, pp. 106-209.

[21] N. Ma, G. Song and H. Lee, "Position Control of Shape Memory Alloy Actuators with Internal Electrical Resistance Feedback using Neural Networks," *Smart Materials and Structures,* vol. 13, no. 4, pp. 777-783, 2004.

[22] M. El Dib, "SMA Actuator Priming Using Resistance Feedback," Master's Thesis, University of Waterloo, University of Waterloo, 2010.

[23] V. Novak, P.Sittner, G. N. Dayananda, F. M. Braz-Fernandes and K. K. Mahesh, "Electric Resistance Variation of NiTi Shape Memory Alloy Wires in Thermomechanical Tests: Experiments and Simulation," *Materials Science and Engineering A,* no. 481 - 482, pp. 127 - 133, 2008.

[24] J. A. Shaw and C. B. Churhill, "Thermo-Electro-Mechanical Shakedown Response of Condition Shape Memory Alloy Wires," in *ASME 2009 Conference on Smart Materials, Adaptive Structures, & Intelligent Systems,* Oxnard, CA, 2009.

[25] V. Novak and P. Sittner, "Micromechanics Modelling of NiTi Polycrystalline Aggregates Transforming Under Tension and Compression Stress," *Materials Science and Engineering A*, no. 378, pp. 490 - 498, 2004.

[26] S. Shu, D. C. Lagoudas, D. Hughes and J. T. Wen, "Modeling of a Flexible Beam Actuated by Shape Memory Alloy Wires," *Smart Materials and Structures*, vol. 6, pp. 265-277, 1997.

[27] W. D. Callister Jr. and D. G. Rethwisch, Fundamentals of Materials Science and Engineering, 4th edition, John Wiley & Sons, 2012.

[28] Quanser Consulting Inc., "MultiQ-PCI Data Acquisition System Reference Manual," 2000. [Online]. Available: http://www.se.rit.edu/~se463/ResearchProject/Quanser/MultiQ-PCI%20Reference%20Manual.pdf.

[29] Analog Devices, "Precision Rail-to-Rail Input and Output Operational Amplifiers," [Online]. Available: http://www.analog.com/static/imported-files/data_sheets/OP184_284_484.pdf. [Accessed July 2012].